

Development of a planning tool for robot-assisted partial nephrectomy surgery based on 3D reconstructions of kidneys

Sarah Vandenbulcke

Student number: 01400560

Supervisors: Prof. dr. ir. Charlotte Debbaut, Prof. dr. ir. Patrick Segers

Counsellors: Prof. dr. Karel Decaestecker, Dr. ir. Danilo Babin, Ir. Pieter De Backer (UGent)

Master's dissertation submitted in order to obtain the academic degree of
Master of Science in Biomedical Engineering

Academic year 2018-2019

Development of a planning tool for robot-assisted partial nephrectomy surgery based on 3D reconstructions of kidneys

Sarah Vandenbulcke

Student number: 01400560

Supervisors: Prof. dr. ir. Charlotte Debbaut, Prof. dr. ir. Patrick Segers

Counsellors: Prof. dr. Karel Decaestecker, Dr. ir. Danilo Babin, Ir. Pieter De Backer (UGent)

Master's dissertation submitted in order to obtain the academic degree of
Master of Science in Biomedical Engineering

Academic year 2018-2019

Preface

Now, I am about to complete my Master thesis, I would like to look one last time back and importantly, thank all the people who supported me on the way. Last year, I chose this master thesis topic because of the close connection with clinical practice and the possibility to develop something new. During my thesis, I learned a lot about biology, but also on the technical level by working with different tools such as Mimics, Python and MeVisLab.

First, I wish to thank Charlotte Debbaut for great guidance during my master thesis. I have really appreciated the regular feedback and all the advice. Further, I also would like to thank Pieter De Backer for making the time to give advice and proofreading and for guiding this project with so much motivation.

For the medical part, I want to thank Karel Decaestecker for the clinical feedback and giving us the opportunity to attend a partial nephrectomy surgery. Importantly, the development of the planning tool would not have been possible without the segmentations by Maryse Lejoly and Stefanie Vanderschelden. Further, I want to address Stijn De Buck for the advice on the use of MeVisLab. It was a great opportunity to work on this topic and therefore I want to thank my supervisors Charlotte Debbaut and Patrick Segers for making this thesis possible.

At last, I want to say thank you to my family for all their support during my studies.

Sarah Vandenbulcke
May 2019

Permission of Use on Loan

"The author gives permission to make this master dissertation available for consultation and to copy parts of this master dissertation for personal use.

In all cases of other use, the copyright terms have to be respected, in particular with regard to the obligation to state explicitly the source when quoting results from this master dissertation."

Sarah Vandembulcke

May 2019

Abstract

Renal cell carcinoma is the most common form of kidney cancer and accounts for 2-3% of all cancers worldwide with the highest incidence in Western Europe. For small renal tumours, the treatment of choice is partial nephrectomy, a surgical procedure that involves resection of the tumour. This treatment allows part of the kidney to remain functional without compromising the oncological outcomes [31]. The surgeon blocks the arterial blood flow towards the tumour in order to avoid excessive bleeding and impaired visibility during tumour resection. Selective clamping of the arteries supplying the tumour minimizes healthy tissue ischemia, but therefore a good knowledge of the patient-specific vascularization and the perfusion of the surrounding parenchyma is crucial [28]. Currently, the surgeon depends to a great extent on his/her experience and 3D insight in the 2D sliced CT data to decide on the clipping locations which complicates pre-operative planning. Visualization of indocyanine green allows to inspect tumour ischemia after clamping, though this technique only provides surface information and can only be used intra-operatively, hence it does not allow for pre-operative planning.

The aim of this thesis is the development of a planning tool for partial nephrectomy surgery that helps the surgeon to decide on the ideal clipping locations. Therefore, a model is developed that uses 3D reconstructions of the renal parenchyma and arterial tree to create a 3D map of the perfusion zones per arterial segment. The perfusion map thus allows to select the arterial segments that supply the tumour and clamping of these vessels may allow bloodless resection of the tumour.

Keywords: partial nephrectomy, kidney cancer, 3D reconstructions, surgical planning

Development of a planning tool for robot assisted partial nephrectomy surgery based on 3D reconstructions of kidneys

Sarah Vandenbulcke

Supervisor(s): Prof. dr. ir. Charlotte Debbaut, Prof. dr. ir. Patrick Segers

Counsellor(s): Ir. Pieter De Backer, Prof. dr. Karel Decaestecker, Dr. ir. Danilo Babin

Abstract—Partial nephrectomy is the treatment of choice for early stage renal cell carcinoma and involves tumour resection from the kidney. Selective clamping of the tumour perfusing arteries during the procedure minimizes healthy tissue ischemia and blood loss but necessitates a profound knowledge of patient-specific vascularization and an estimation of the corresponding perfusion regions. In this work, we present a framework to predict these perfusion regions based on 3D models derived from CT scans and validate it against available commercial software packages.

Keywords— Partial nephrectomy, renal cell carcinoma, 3D reconstructions, surgical planning

I. INTRODUCTION

RENAL cell carcinoma is the most common type of kidney cancer, accounting for 2-3 % of all cancers worldwide with the highest incidence in western countries. Partial nephrectomy is the treatment of choice for small renal tumours allowing part of the kidney to remain functional without increasing the risk of cancer recurrence [1]. During the procedure, the blood supply towards the tumour is blocked to avoid excessive bleeding during resection. To minimize healthy tissue ischemia, the surgeon selectively clamps the arteries supplying the tumour region. Hence, a good understanding of the patient-specific vasculature and the perfusion of the surrounding parenchyma is crucial [2].

Nowadays, the surgeon mainly relies on his/her own experience and 3D insight in the 2D sliced CT images to decide on the ideal clipping locations. To help the surgeon in this decision, intra-operative visualization of vascularization through the use of indocyanine green injection is often used nowadays. This allows to see whether the tumour is completely ischemic after clamping [3]. However, the view is limited to the renal surface only and the method cannot be applied pre-operatively. Furthermore, 3D models have large potential for surgical planning, since they are thought to improve the 3D insight in the patient-specific anatomy. However, the accuracy is limited by the quality of the scans and these models do not provide direct perfusion information [4]. Up to present, we found only one commercial company providing a specialised service for surgical planning based on arterial perfusion, though its models are not clinically validated and very expensive. Thus, there is clearly a need for new, affordable planning tools that facilitate pre- and intra-operative planning.

Here, we present a model that determines the arterial perfusion zones based on the anatomical information derived from standard pre-operative CT scans. Our model suggests the the-

oretical perfusion areas per vessel and thus allows for adequate planning through 3D visualization of these perfusion zones. As such, it can provide the clamping locations for bloodless tumour resection with minimal healthy tissue ischemia.

II. MATERIALS AND METHODS

The model creates a map of the perfusion regions in the kidney, by assigning each point of the parenchyma to a specific branch of the arterial tree. For every point, the branch is selected that has the highest probability to supply that point. This probability is approximated by the distance between the branch and that specific point. In short, the model determines the closest branch for each point of the kidney based on the anatomy of the arterial tree. A similar method was already applied on the portal tree of the liver by Selle et al. in 2002 [5]. The comparison of their model outcomes with the real perfusion zones showed an overlap of about 80%, suggesting that this approach makes sense anatomically. The anatomical data is obtained from segmented CT data of the affected kidney and the arterial tree. Figure 1 shows the 3 main steps in construction of the model.

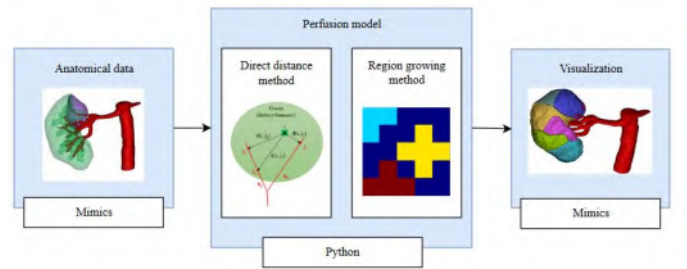


Fig. 1. The built-up of the model into 3 steps starting with segmentation of the anatomical data in the Mimics software package [6]. This information is used to determine the perfusion zones using two different methods, namely the direct distance and region growing method by implementation in Python. The resulting perfusion zones are visualised using Mimics®.

A. Anatomical data

The input for the model contains anatomical data of the arterial tree, the renal parenchyma and the tumour. This anatomical information is obtained from CT images by segmentation in Mimics, a software package for advanced image processing developed by Materialise (Leuven) [6]. The original CT images are obtained from patients suffering from kidney cancer before

they underwent partial nephrectomy. The segmentation allows to construct a 3D model and use the volumes of the different structures as the input of the model. For analysis of the vascular structure, the arterial tree is first transformed into a centreline model using Mimics®. The resulting graph structure exists of automatically numbered branches that are built up from closely spaced (control) points connected to each other. The skeleton is exported by the coordinates of these control points together with their corresponding branch numbers. The segmented 3D volumes of the kidney, tumour and arteries are exported as 2D image slices in BMP format.

B. Perfusion model in python

Once the anatomical data is stored in an adequate format, the patient-specific settings are adjusted step by step as listed below. Based on these settings and the anatomical data, the model determines the perfusion zones of the renal parenchyma and tumour.

- The file directories of the text file containing the skeleton and the BMP files of the kidney, tumour and arteries are inserted.
- The user defines the dimensions of the BMP slices and the Mimics® image volume so that the model can adjust the centreline coordinates in the Mimics® coordinate system to the coordinate system defined by the BMP slices called the 'voxel' coordinate system.
- The slice thickness and the z-coordinate of the start slice are inserted.
- Arterial segments starting outside the parenchyma and subsequently entering it, as well as segments with a dead end are selected. These segments are the most relevant ones in surgical planning as they are the most likely to be clamped by the surgeon.
- The user defines the Mimics® image volume and the discrete image volume based on the slice dimensions. These values are necessary for coordinate transformation.

The underlying algorithm is also built up in three parts. First, the model loads and processes the anatomical data based on the input settings to retrieve the required information summarized in table I.

TABLE I
OVERVIEW OF THE DATA THAT IS LOADED IN THE MODEL.

Structure	Information
Kidney parenchyma	coordinates of all parenchyma points
Tumour	coordinates of all tumour points
Arteries	coordinates of all arteries points
Skeleton	coordinates selected control points branch numbers control points

For each point of the parenchyma and tumour, the model selects the closest branch. Therefore, two different approaches are applied: the direct distance approach and the region growing approach.

B.1 Direct distance method

The direct distance approach calculates for each voxel i of the tissue (both parenchyma and tumour) the squared distance $d^2(i, j)$ to all control points of the skeleton. Based on these distances, the control point l corresponding with minimum distance is selected as depicted in equation 1.

$$d^2(i, l) = \min\{d^2(i, 1), d^2(i, 2), \dots, d^2(i, n)\} \quad (1)$$

Each control point is linked to the number of the branch where it is located on. Hence, the branch number b of control point l is assigned to voxel i , by setting the function S_{tissue} for this voxel i equal to b as depicted in equation 2.

$$S_{tissue}(i) = b(l) \quad (2)$$

This process is applied until all voxels of the tumour and kidney are assigned to the adequate branch.

B.2 Region growing method

For the region growing (RG) method, the skeleton branches grow with the same speed in all directions within the image volume until they meet another growing branch. The method starts with the introduction of a region growing list that contains the branch numbers and the coordinates of the control points of the arterial tree. Next, the first element of the list is selected and the surrounding points are determined as depicted in figure 2

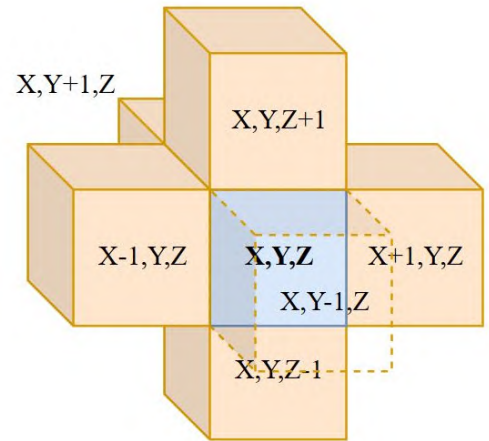


Fig. 2. The starting point (blue) with coordinates (X, Y, Z) grown in all 6 directions (orange) with same step size.

These newly defined points are added to the RG list when they are part of the image volume and are not labelled. Then, the next element of the list is selected and again the surrounding points are defined in the same way as described above. The algorithm runs until all points of the image volume contain a label and that results in a map of the perfusion zones over the complete image volume. By only selecting the voxels that are part of the kidney or tumour based on the anatomical data of these structures, the perfusion zones in the parenchyma and tumour are obtained.

C. Visualization

The model delivers information about the perfusion zones in 3D volumes and is able to visualize them in 2D format as depicted in figure 3. Though, interpretation of the results requires 3D visualization and therefore, the Mimics® software is again used. The model returns grey value images containing the arterial tree, the tumour and the kidney in BMP format. These grey value images are loaded in Mimics® that is able to transform them back again in a 3D structure.

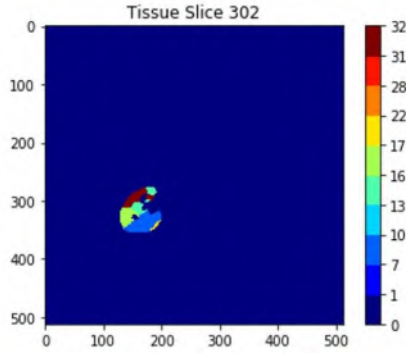


Fig. 3. The 2D visualization of an image slices of the kidney divided into perfusion zones. The numbers depict the numbers of the branches that supply their corresponding perfusion regions.

III. RESULTS

The outcomes of the model are retrieved from segmented CT data of patients before they underwent partial nephrectomy, using the direct distance and region growing method. Figure 4 shows the results of the direct distance and region growing method applied to the same patient. Though both methods are implemented to determine the closest branch, the resulting perfusion zones are slightly different. Despite these differences, a closer look on the tumour shows that both methods predict the same branches supplying the tumour and hence identical clipping locations are suggested.

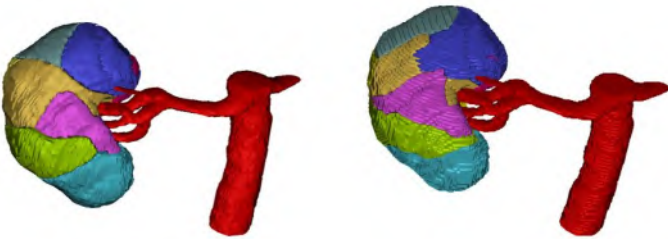


Fig. 4. The 3D map of the perfusion zones due application of (left) the direct distance method and (right) the region growing method.

To our knowledge, the only commercial service providing surgical planning is the one from Visible Patient. Although not clinically validated, these models seem to successfully predict tumour supplying arteries. Figure 5 compares our results to those provided by the online service of Visible Patient, showing that the volumes are not completely the same. Multiple fac-

tors influence these differences, but the most important factor is probably that the segmentations are not identical.

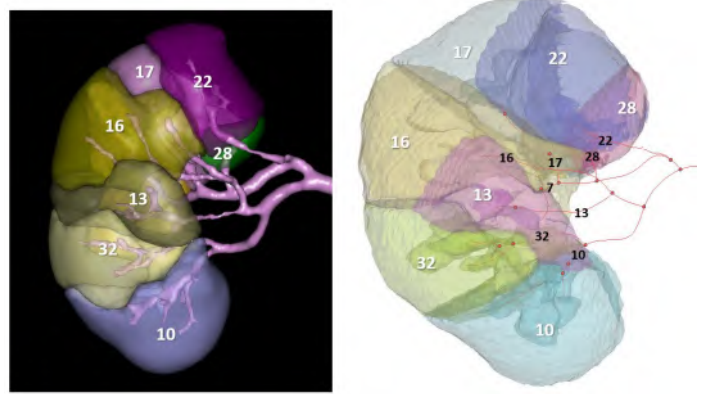


Fig. 5. The outcomes of Visible Patient (left) are compared with those of the perfusion model (right). The numbers designate the numbers of the arterial segments supplying the kidney tissue.

As an example, figure 6 takes a closer look at the results for the tumour perfusion zones. According to Visible Patient, the tumour is supplied by 4 different branches, namely 22, 28, 17 and 16. At the same time, our perfusion model predicts the same branches and an additional branch 5. Thus, these results suggest that both methods will result in complete tumour ischemia when actually clamping, though our perfusion model will cause more healthy tissue ischemia. As stated above, the image also indicates that the reconstruction of the arterial tree of Visible Patient is more detailed than the one used for our model which will most probably explain the different results.

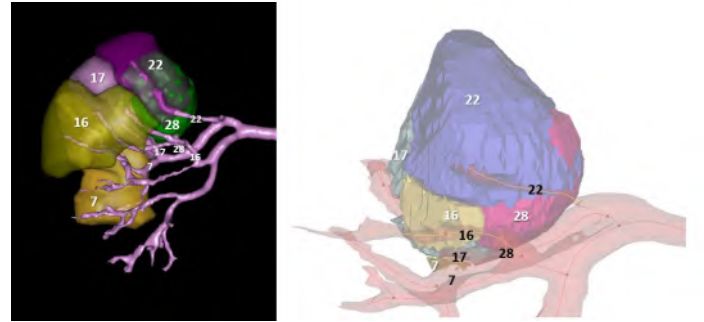


Fig. 6. Detail of the tumour perfusion for the clipping model of Visible Patient (left) and the perfusion model (right). The numbers designate the branches of the arterial segments supplying the tumour.

IV. IMPLEMENTATION IN MeVisLAB

The current tool uses different types of software to create a 3D map of the perfusion zones starting from segmented CT images. The implementation of the tool into clinical practice requires the integration of different steps in one interface to allow the use of the tool without technical knowledge whilst decreasing the amount of manual work. A good candidate for such an interface is MeVisLab, which possesses functionalities to import data, write code and visualise the outcomes [7]. Unfortunately, the functionalities of the free version of the MeVisLab software

are limited related to scripting, not allowing implementation of large Python files as created to run the model. Thus, towards the future, there should be looked for alternative solutions for the implementation of the model in MeVisLab and whether it is necessary to purchase a licence.

V. CONCLUSION

A model is developed that is able to create a 3D map of the kidney and tumour divided into perfusion zones and thus, enables to predict the arteries supplying the tumour. The comparison with the clipping models of Visible Patient proves that the results correctly predict the tumour perfusing arteries, though also suggests some false positives. That shows that the results are promising, but optimizations of the model and its input data are necessary to obtain better results in the future.

REFERENCES

- [1] Borje Ljungberg, L. Albiges, K. Bensalah, A. Bex, R. H. Giles, M. Hora, Markus A. Kuczyk, Thomas Lam, Lorenzo Marconi, Axel S. Merseburger, and et al., “Eau guidelines on renal cell carcinoma,” *European Association of Urology*, 2018.
- [2] Mark A Perazella, Robert Dreicer, and Mitchell H Rosner, “Renal cell carcinoma for the nephrologist,” *Kidney International*, vol. 94, no. 3, pp. 471–483, 2018.
- [3] Marc Bjurlin, Tyler Mcclintock, and Michael Stifelman, *Near-Infrared Fluorescence Imaging with Intraoperative Administration of Indocyanine Green for Robotic Partial Nephrectomy*, vol. 16, 2015.
- [4] Francesco Porpiglia, Daniele Amparore, Enrico Checcucci, Riccardo Autorino, Matteo Manfredi, Giada Iannizzi, and Cristian Fiori, “Current Use of Three-dimensional Model Technology in Urology: A Road Map for Personalised Surgical Planning,” *European Urology Focus*, vol. 4, no. 5, pp. 652–656, 2018.
- [5] D Selle, B Preim, A Schenk, and H. Peitgen, “Analysis of vasculature for liver surgical planning,” *IEEE Transactions on Medical Imaging*, vol. 21, no. 11, pp. 1344–1357, 2002.
- [6] Materialise mimics. <https://www.materialise.com/en/medical/software/mimics> [accessed March 3, 2019].
- [7] Mevislab: Features. <https://www.mevislab.de/mevislab/features/> [accessed April 10, 2019].

Contents

List of Figures	xv
List of Tables	xv
List of Symbols	xvi
List of Abbreviations	xvii
1 Introduction	1
2 Background	3
2.1 Renal anatomy	3
2.2 Renal function	5
2.3 Renal cancer	5
2.3.1 Staging of renal tumour	7
2.3.2 Treatments for renal cancer	8
2.4 Partial nephrectomy	9
2.5 Study of the renal vasculature	10
2.5.1 Anatomy of renal vasculature	10
2.5.2 Modelling of the vasculature	12
2.6 Methods for determining perfusion areas	16
2.6.1 Anatomical approaches	16
2.6.2 Model-based approaches	17
2.7 Current surgical planning tools	24
2.8 Implementation for clinical practice	27
3 Materials and Methods	29
3.1 Anatomical data	31
3.1.1 Segmentation	31
3.1.2 Skeletonization	32
3.2 Perfusion model	34
3.2.1 Load input data	35
3.2.2 Apply the model	40

3.2.3	Output 2D slices	46
3.3	Visualization and validation	47
4	Results and discussion	49
4.1	Input of the patient cases	50
4.2	Results of direct distance method	53
4.3	Results of region growing method	60
4.4	Validation of results	63
5	Implementation	69
5.1	Import imaging data	69
5.2	Implementation of the algorithm	73
5.2.1	Visualization	74
5.3	Conclusion	77
6	Conclusion and future perspectives	79
	Bibliography	87
	Appendix	89
A	Overview Python Files	89
A.1	Patient-specific settings	89
A.2	Algorithm of Perfusion model	90

List of Figures

2.1	The nephron is the functional unit of the kidney. Retrieved from [8].	4
2.2	The anatomy of the kidney. Retrieved from [37].	5
2.3	Schematic drawing of a kidney affected by renal cancer. Retrieved from [5].	6
2.4	The 4 main stages of renal tumour. Retrieved from [47].	8
2.5	Partial nephrectomy surgery. Retrieved from [35].	9
2.6	Illustration of the Grave's theory dividing the kidney into 5 segments. Retrieved from [14]	11
2.7	Two examples of anatomical variations of the renal vasculature: (left) extrahilar artery and (right) superior polar artery. Retrieved from [15]	11
2.8	Venous tree of the kidney with the color designating the vessel ordering. Retrieved from [36].	12
2.9	Overview of different ordering methods, (A) top-down ordering method, (B) the Strahler ordering and (C) the diameter-defined Strahler ordering. Retrieved from [38].	13
2.10	3D Reconstruction of the hepatic circulation with hepatic venous (blue), portal venous (yellow) and hepatic arterial system (red). Retrieved from [38].	14
2.11	Thinning algorithm for skeletonization. Retrieved from [38].	15
2.12	Top-down ordering applied to the portal tree. Retrieved from [38].	15
2.13	View of renal tumour after selective clamping of the arterial segment with (a) normal view and (b) the infrared light is set on. ICG shows incomplete clamping of the tumour, as it still colors green. Retrieved from [33].	17
2.14	blood vessels and muscle tissue are segmented from images i.e. μ CT images. Retrieved from [49]	18
2.15	Voronoi polygons to define perfusing regions of capillaries. Retrieved from [49].	19
2.16	The ideal situation (left), where the vascular territories can be directly determined from the detailed branching structure versus reality where modelling is required (right). Retrieved from [46]	20
2.17	The shortest euclidean distances for every voxel to branch B_i : the brighter the voxel, the closer the voxel is to the branch. Retrieved from [46].	20

2.18	The segments are defined based on the minimal distances. Retrieved from [46].	21
2.19	The result of solving the Laplace equation for branch B_i . Retrieved from [46].	22
2.20	The resulting map of the liver divided into segments using the LASA approach. Retrieved from [46].	22
2.21	The results of vascular corrosion casting for different pruning levels from left to right: low, medium and high pruning. Retrieved from [46].	23
2.22	The dissection of the renal branches is guided by the 3D reconstruction: the upper image shows the normal anatomy and the images below shows the super-accuracy 3D reconstruction superimposed on the true anatomy. Retrieved from [41].	25
2.23	3D models produced by Visible Patient: (left) 3D model of kidney with tumour and its vasculature, and (right) liver divided into perfusion zones supplied by the branches of the portal vein. Retrieved from [48].	26
3.1	Overview of the complete workflow existing of three main steps: the preparation and import of anatomical data in Mimics, the new perfusion model and the 3D visualization.	30
3.2	3D model of the kidney parenchyma (green), the tumour (purple) and arteries (red) obtained in Mimics Research after segmentation.	31
3.3	CT slice of a patient with a tumour in the right kidney. (left) contrast enhanced CT slice and (right) CT slice showing segmentation masks of kidney parenchyma (green), tumour (purple) and arteries (red).	32
3.4	Centreline calculated in Mimics from the 3D model of the arterial tree . . .	33
3.5	Centreline with corresponding branch numbers. The colours of the numbers designate the corresponding generations following a top-down ordering.	33
3.6	The model starts with (1) loading the data of the skeleton, the tumour and the kidney. Next (2), the data is used by the model to determine the perfusion areas of the arterial tree. At last (3), these results are exported as 2D slices and converted into 3D images.	34
3.7	Example of the data in the text file where the branch number (green box) and the x, y and z coordinates of each control point (red box) can be obtained. The other specifications in the file, such as the minimal radius are now not used, though may be interesting for future applications.	35
3.8	The X_{mc} , Y_{mc} and Z_{mc} coordinates in Mimics coordinate system (left) are transformed into new coordinates X_v, Y_v and Z_v in 'voxel' coordinate system (right), according to the transformation depicted by equations 3.1, 3.2 and 3.3	36

3.9	The tumour and the tissue are supplied by different branches of the arterial tree. The arterial tree is skeletonized and the branch numbers are added. The bold numbers depict the branches that fulfil the two requirements as set in this section and therefore are selected as the branches determining the perfusion zones. The underscored numbers mark the segments that are situated inside the kidney and are ramifications of the selected (bold) branches.	38
3.10	Examples of axial 2D slices of the kidney (left) and tumour (right).	39
3.11	Simple example of the principle of the direct distance approach explained above.	41
3.12	Two slices obtained from the direct distance method.	42
3.13	The initial situation (a): three points are labelled with 1(blue),2 (yellow) and 3(brown) and (b) the result after one step of region growing.	43
3.14	(a) The initial situation with three differently labelled points. (b) the situation after one step of region growing of each region. (c) shows further progression in region growing and (d) shows the final result of three different regions labelled with 1, 2 and 3 or blue, yellow and brown.	44
3.15	Two image slices as results of the region growing.	46
3.16	Image slice of the kidney (left) and the tumour (right) divided into perfusion zones as a result of the region growing method.	46
4.1	Anterior view on 3D models of the renal parenchyma (green), tumour (purple) and arteries(red) as result of segmentation	49
4.2	The 3D model of the arterial tree and the calculated centrelines for each patient case in anterior view for patient 1 and 4 and posterior view for patient 2 and 3. The complexity of the reconstruction of the tree of patient 3 has more detail than the trees of the other patients.	51
4.3	The tumour and the tissue are supplied by different branches of the arterial tree. The bold numbers depict the numbers of the branches that fulfil the requirements as set in section 3.2.1 and therefore, are selected as the branches determining the perfusion zones.	52
4.4	Anterior and posterior view on the perfusion maps with the arterial tree of patient 1 (a-b) and 2 (c-d). Each color represents a perfusion zone supplying the corresponding arterial branch.	53
4.5	Anterior and posterior view on the perfusion maps with the arterial tree of patient 3 (a-b) and 4 (c-d). Each color represents a perfusion zone supplying the corresponding arterial branch.	54
4.6	(a) The detail of the tumour of patient 1 shows 5 perfusion zones in the tumour, supplied by branches 7, 16, 17, 22 and 28. (b) The perfusion map of these branches in the complete kidney shows that they perfuse about half the kidney including a substantial part of the healthy parenchyma. . .	55

4.7	(a) The detail of the tumour of patient 2 shows 3 perfusion regions in the tumour, supplied by the branches 7, 12 and 13 according to the results of the model. (b) The perfusion zones supply zones of the tumour and also part of the healthy parenchyma.	56
4.8	3D perfusion maps of the kidney of patient 4 with branch 9 added and without this branch.	57
4.9	(a) The detail of the tumour of the patient 4 when segment 9 is added to the model shows that there are 3 branches perfusing the tumour namely 2,9 and 11. (a) The detail of the patient 4 when there is no segment 9 shows that there are only 2 branches supplying the tumour, namely 2 and 11.	57
4.10	Perfusion zones of the branches of the 3rd generation. (a-c) The perfusion zones are determined based on the information of the pruned tree. (b-d) The results are obtained based on the complete tree	58
4.11	The detail of the tumour with (a) 5 perfusion zones when the complete arterial tree is used and (b) 2 perfusion zones when the tree pruned until only the 3 first generation remain.	59
4.12	Anterior and posterior view on the perfusion maps of patient 1 obtained with region growing (a-b) and with the direct distance method (c-d). Each color represents a perfusion zone supplied by the corresponding arterial branch.	60
4.13	The detail of the tumour of patient 1 with perfusion zones determined according to (a) the region growing approach and (b) the direct distance approach.	61
4.14	The detail of the tumour of patient 2 with perfusion zones determined according to (a) the region growing approach and (b) the direct distance approach.	61
4.15	Anterior and posterior view on the perfusion maps of patient 2 obtained with region growing (a-b) and with the direct distance method (c-d). Each color represents a perfusion zone supplied by the corresponding arterial branch.	62
4.16	The results of Visible Patient (a-c) on the left side are compared to the results of our model (b, d) on the right side. The black numbers show the labels of the branches and the white and coloured numbers correspond to the perfusion zones.	64
4.17	Detail of the perfusion zones supplying the tumour. (a) Visible Patient predicts that 4 branches supply the tumour, namely 16, 17, 22 and 28. (b) Our model suggests that there are 5 perfusion zones supplied by branches 7, 16, 17, 22 and 28.	65

4.18	Arterial tree obtained by Visible Patient (b) has a higher complexity than the one used in our model (a)	65
4.19	Detail of the perfusion zones supplying the tumour for patient 2. (a) Visible Patient predicts that 2 branches supply the tumour, namely 13 and 7. (b) Our model suggests that the 2 perfusion zones are supplied by branches 7,12 and 13.	66
4.20	The results for patient 2 of Visible Patient (a-c) on the left side are compared to the results of our model (b, d) on the right side. The black numbers show the labels of the branches and the white and coloured numbers correspond to the perfusion zones.	67
4.21	Arterial tree of patient 2 with tumour and tumour supplying arteries assigned. The arterial segments by (a) Visible Patient have a higher complexity than (b) those used in our model.	68
5.1	The network required to load multiple DICOM slices and visualize the resulting image volume in 2D	70
5.2	The network required to load and visualise the kidney volume starting from 2D DICOM slices exported from Mimics.	70
5.3	The network required to load and visualise the kidney volume starting from 2D BMP slices exported from Mimics.	71
5.4	Window to create a macro module. (a) The name of the module, the project and the package is selected. (b) A Python file can be added to the module to allow scripting. (c) Fields can be created to import for instance specific variables or directories.	73
5.5	(a)Module to run the perfusion model with corresponding code (b) to define functionalities	74
5.6	Network (a) schematic and (b) in MeVisLab to obtain 3D visualization of arterial tree and the perfusion zones of the kidney and tumour. There is started from the 2D BMP slices of the image volume that combines the tumour, kidney and arteries.	74
5.7	Schematic representation of the network to obtain 3D visualization of the arterial tree and the perfusion zones of the kidney and tumour when starting from the BMP files of the separate structures. Each load BMP slices module represents the combination of the ImageComposer and ImageMultiLoad module.	75
5.8	Network in MeVisLab to obtain 3D visualization of the arterial tree and the perfusion zones of the kidney and tumour. There is started from the 2D BMP slices of the tumour, kidney and arteries separately.	76
5.9	(a)Visualization of perfusion zones starting from combined images. (b) Visualization of the perfusion zones starting from separate images of the structures.	77

List of Tables

2.1	TNM staging system with data retrieved from [17]	7
2.2	Percentages of the volume overlap between outcomes of the described LASA and NNSA methods and the results of vascular corrosion casts, results retrieved from [46]	23
2.3	Overview of image acquisition and contrast agent (non-ionic with 350 mg I/ml or 370 mg I/ml) settings used in [41] to obtain high-resolution CT images.	25
3.1	Overview of the import data that is loaded in the model.	35
4.1	Overview of image specifications for each dataset containing the complete shape of the image volume, the original and loaded number of slices, the slice thickness or slice gap and the z-coordinate of the first slice that is loaded.	50
5.1	Overview of what should be manually inserted in the model.	72
6.1	Overview of the settings in Python with their corresponding description. .	90

List of symbols

Symbol	Description	Unit
g	Metric assigning voxel to appropriate liver segment, from [46]	[-]
S_i	Liver segment i, from [46]	[-]
L	Collection of points forming the liver volume, from [46]	[-]
V	Collection of points forming the hepatic vein, from [46]	[-]
B_i	Branch of the portal tree perfusing the segment i, from [46]	[-]
B_i	Portal tree, from [46]	[-]
v	Voxel of the image volume, from [46]	[-]
ϕ	Harmonic function, solution of Laplace equation, from [46]	[-]
X_{mc}, Y_{mc}, Z_{mc}	X, Y and Z coordinates of control point in Mimics coordinate system	[mm]
X_v, Y_v, Z_v	X, Y and Z-coordinates of control point in 'voxel' coordinate system	[mm]
$\Delta X_v, \Delta Y_v, \Delta Z_v$	X, Y and Z dimensions of the image volume in 'voxel' coordinate system	[mm]
$\Delta X_{mc}, \Delta Y_{mc}, \Delta Z_{mc}$	X, Y and Z dimensions of the image volume in Mimics coordinate system	[mm]
$X_{min}, Y_{min}, Z_{min}$	Minimum X, Y and Z coordinates in Mimics coordinate system	[mm]
$X_{tissue}, Y_{tissue}, Z_{tissue}$	X, Y and Z coordinates of voxel of tissue (tumour/-parenchyma) volume in 'voxel' coordinate system.	[mm]
d	Distance	[mm]
S_{tissue}	Function returning the assigned branch number for tissue point	[-]
b	Branch number	[-]
BL	List containing all selected branch numbers	[-]
RG	Region growing list with voxels and branch numbers	[-]

List of abbreviations

BMP	Bitmap Image File
CE	Conformité Européenne: mark for products that hold with standards within the European Economic Area
CT	Computed Tomography
DDM	Direct Distance Method
DICOM	Digital Imaging and Communications in Medicine
EAU	European Association of Urology
HA3D	Hyper-Accuracy 3D reconstructions
ICG	Indocyanine Green
ISO	International Organization for Standardisation
LASA	Laplacian Segment Approximation
LRLT	Living-Related Liver Transplant
MRI	Magnetic Resonance Imaging
NIRF	Near-Infrared Fluorescence Imaging
NNS	Nephron Saving Surgery
NNSA	Nearest Neighbour Segment Approximation
PN	Partial nephrectomy
RAPN	Robot-Assisted Partial Nephrectomy
RCC	Renal Cell Carcinoma
RGM	Region Growing Method
TNM	Classification system for malignant tumours based on their extent of spread
VEGF	Vascular Endothelial Growth Factor

Chapter 1

Introduction

The kidneys are essential organs of the human body responsible for several vital functions such as the removal of waste products and excessive fluids. Loss of kidney function causes waste material to accumulate in the body, disturbs electrolyte balance, and hence can severely impact the quality of life. Dialysis and transplantation are currently the most effective treatments for renal failure, but are costly and impair patient life quality [27]. Several conditions may result in renal failure, among them kidney cancer.

Kidney cancer is not a single type of cancer, but is a term used to designate different types of cancer occurring in the kidneys [29]. The most common form is renal cell carcinoma (RCC), cancer originating from the lining of the proximal renal tubules, responsible for primary urine transport. According to the EAU guidelines on RCC [31], RCC accounts for 2-3 % of all cancers globally with the highest incidence in Western Europe. Surgical removal is the treatment of choice for kidney cancer as long as the cancer has not yet spread to other parts of the body. In radical nephrectomy, the entire kidney is removed including the surrounding fascia, adrenal gland, and upper ureter. An alternative is partial nephrectomy or nephron saving surgery, where only the diseased part of the kidney is removed allowing the remaining part to still be functional [30].

Partial nephrectomy is recommended whenever technically feasible and is considered as the treatment of choice for early-stage RCC. Compared to radical nephrectomy, kidney function is better preserved and the risk of developing metabolic or cardiovascular disorders is reduced [31, 25]. Currently, robotically assisted partial nephrectomy becomes more widely applied for renal tumours, thanks to the progressions in technology and medicine [42].

During partial nephrectomy, cancer recurrence is avoided by ensuring the integrity of the tumour capsule and removal of the tissue around the edge of the tumour. The supplying vessels of the kidney are usually blocked to avoid excessive blood loss and increase the visibility for the surgeon.

This, however, also increases the ischemia time, the time during which there is insufficient blood supply to the renal tissue. This, in turn, increases the risk of losing kidney function after surgery [28]. To avoid unnecessary healthy tissue ischemia, the surgeon should be able to selectively block the arteries supplying the tumour and leave those that supply the healthy tissue untouched [39]. Currently, the surgeon depends to a great extent on his/her experience and 3D insight in the 2D sliced CT data to decide on the clipping locations what complicates preoperative planning. Visualization of tissue ischemia with indocyanine green injections has proven to be useful to facilitate decision making, though the technique only gives information about the surface and does not allow for pre-operative planning. Thus, there is clearly a need for better preoperative planning.

The goal of this thesis is the development of a tool that enables pre-surgical planning of partial nephrectomy. Therefore, a model is developed that uses 3D reconstructions of kidneys and the arterial tree to make patient-specific 3D models of the kidney perfusion. The planning tool may enable the surgeon to pre-operatively distinguish tumour perfusing arteries from those supplying healthy tissue and that could minimize healthy tissue ischemia and thus minimal loss of kidney function.

This master's dissertation presents the model in six different chapters. Chapter 2 introduces the clinical background concerning the renal anatomy, physiology, renal cancer and partial nephrectomy. Thereafter, a closer look is taken to the current progress in vascular modelling and surgical planning to serve as inspiration for the planning tool. Then, a closer look is taken at the planning tool itself. Chapter 3 starts with explaining the functioning of the complete model and the associated workflow. Then, chapter 4 discusses the results of this tool, that are validated in the same chapter. One last technical part in chapter 5 shows the possibilities for implementation of the planning tool. There is finally concluded with some final thoughts and a look toward the possibilities in the future.

Chapter 2

Background

Before taking a closer look at the model, this chapter provides both clinical and technical background relevant for the construction and interpretation of the model. There is started with a concise overview on the renal anatomy and function, followed by the introduction of renal cancer and its treatments. The more technical part discusses the current progress in vascular modelling and the ongoing developments in surgical planning.

2.1 Renal anatomy

Under normal circumstances, people have two kidneys, one at each side of the vertebral column, lying behind the peritoneal space in the abdomen and they are characterized by their typical bean-like shape. Each kidney is surrounded by three layers of connective tissue, collectively called the renal capsule, that provides protection, stability and serves as an attachment site for the surrounding tissue. The renal capsule is surrounded by the renal fascia that encapsulates the kidneys and the adrenal glands [4].

On a microscopic scale, the kidney is primarily composed of its functional units, the nephrons. The general structure of one nephron is depicted in figure 2.1. There are approximately 1 million nephrons in the human kidney and each of these nephrons exists of a renal corpuscle and linked to it the convoluted tubules [22]. The initial filtration from the blood into urine is performed at the level of the renal corpuscle containing the glomerulus, which is a dense network of capillaries, and the surrounding Bowman's capsule. Water, ions and small molecules are forced through the filtration barrier between capillaries and the Bowman's capsule. The filtration is enabled by the selective permeability of the glomerular endothelium to fluids and small molecules and the elevated hydrostatic pressure in the capillaries due to vasoconstriction, which is the narrowing of blood vessels. The initial filtrate flows from Bowman's capsule to the renal tubule along which it changes its composition by reabsorption and secretion. Most of the reabsorption of solutes happens in the first convoluted part of the tubule, the proximal tubule.

Next, the urine flows into the loop of Henle, that is mainly responsible for the urine concentration by reabsorbing water and salt from the urine. Then, the urine is transported through the distal tubule into the collecting duct, where only minor changes are applied to the urine composition [37].

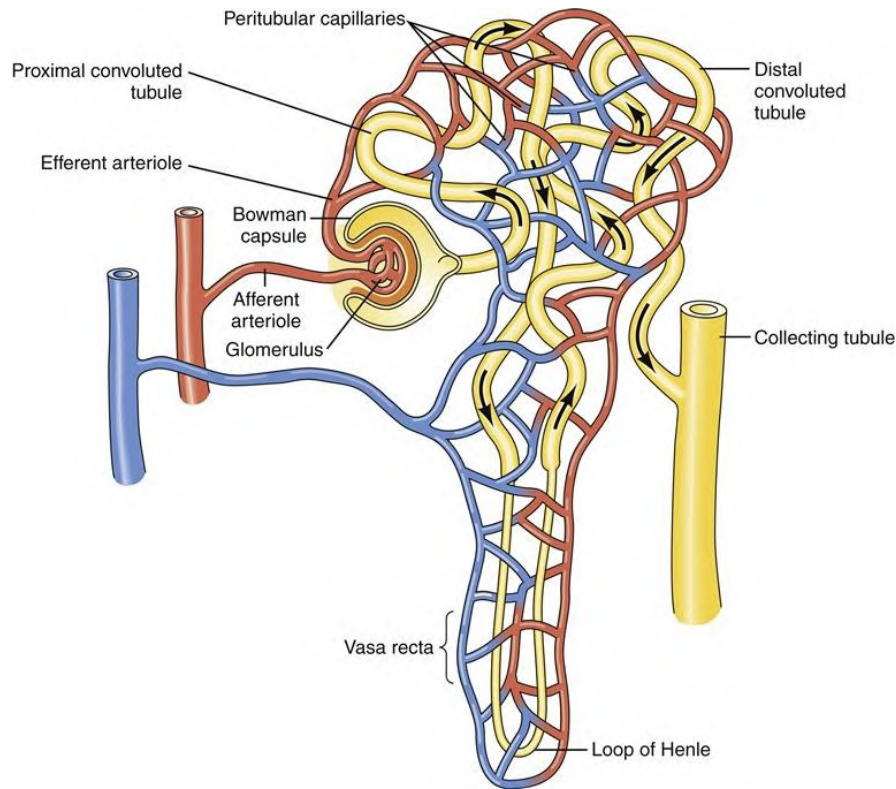


Figure 2.1: The nephron is the functional unit of the kidney. Retrieved from [8].

On a macroscopic scale, as shown in figure 2.2, the kidney exists of an inner and outer zone. The outer zone is the renal cortex that contains the glomeruli. The inner zone of the kidney or medulla is made up of conically shaped areas, the so-called renal pyramids. Here, the loops of Henle, the vasa recta and the collecting ducts are found. These collecting ducts are responsible for urine transportation towards the renal calyces where the urine collects and is passed toward the ureter for excretion. The vasa recta are straight capillaries lying parallel to the loop of Henle, and they enable reabsorption and secretion between the renal tubule and the blood [7].

The ureter transports urine toward the bladder from where it is excreted out of the body. The kidneys are perfused by the renal arteries, which are direct branches of the descending aorta. According to Herzlinger and Hurtado [22], about 20% of the cardiac output is transported toward the kidneys along the renal arteries, though the kidneys account only for 0.08 % of the body weight. This large incoming blood volume allows the kidneys to effectively manage the balance of ions, fluids and waste products and therefore exceeds the amount blood supply required for their metabolic needs.

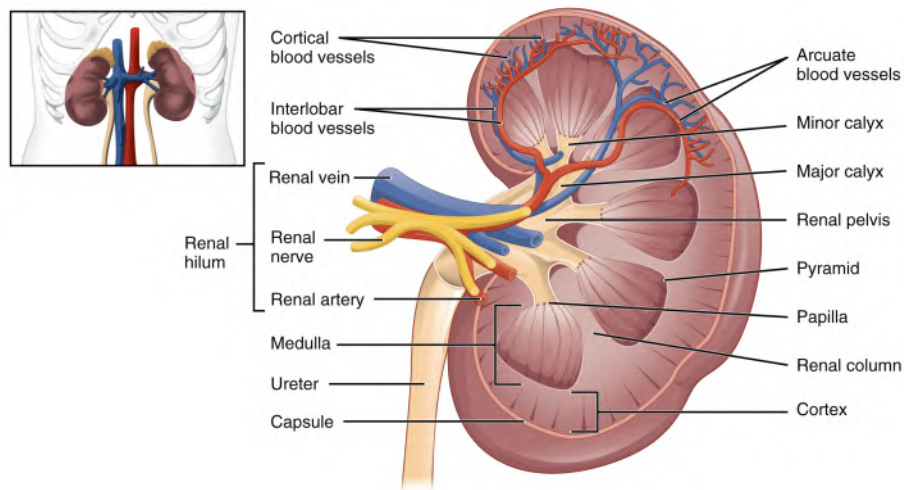


Figure 2.2: The anatomy of the kidney. Retrieved from [37].

2.2 Renal function

The functional anatomy of the kidney, as described before, is strongly linked with its main functions of removing waste products and excessive fluids from the body. By regulating the body's fluid, electrolyte, and acid-base balance, the kidneys play an important role in the maintenance of the body constitution. Other important functions are the production of hormones such as erythropoietin that influences the production of red blood cells and vitamin D that regulates the amount of calcium in the body. On top of each kidney, the adrenal gland can be found, responsible for the production of several hormones such as cortisol, adrenaline, and aldosterone [4].

The loss of kidney function results in severe consequences and even death. Without clinical intervention, sustaining life becomes impossible when filtration from glomerulus, absorption or reabsorption from renal tubules get affected. Death resulting from renal diseases is ranked as the 9th most abundant cause of death in the USA [19].

2.3 Renal cancer

In the previous paragraphs, the anatomy and function of healthy kidneys were studied showing their important role in the human body. Unfortunately, several renal conditions exist that can endanger the health of a person. Renal cancer or kidney cancer is one of them. As already mentioned in the introduction, the most common group of kidney cancers is renal cell carcinoma (RCC), originating from the epithelial cells of the renal tubules. They account for 85% of all primary renal neoplasms or tumours originating from the kidney [34]. RCC accounts for about 5% in men and 3% in women of all oncological diagnoses and is the 6th most diagnosed cancer in men and 10th in women [12].

The highest incidence rates are found in developed countries in northern Europe and America and RCC is twice as prevalent in men as in women. Only 4 % of all cases of RCC are familial and clear cell RCC, the most common form of RCC, usually arises from an inherited mutation in the von Hippel-Lindau tumour suppressor gene [11]. The majority of cases is sporadic and for these, the most important risk factors are cigarette smoking, obesity and hypertension [24].

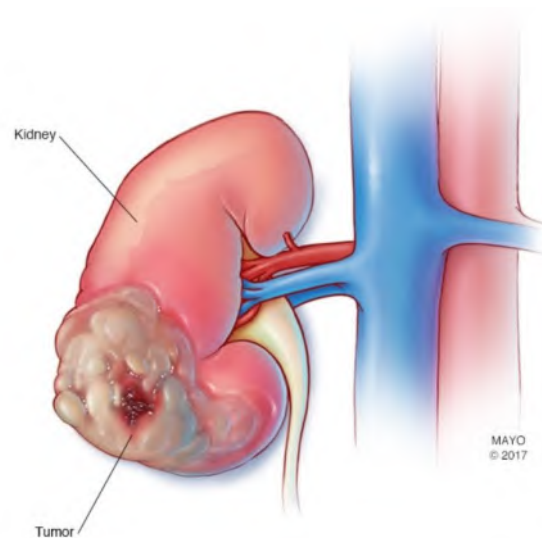


Figure 2.3: Schematic drawing of a kidney affected by renal cancer. Retrieved from [5].

Figure 2.3 presents a schematic drawing of kidney cancer. In early stages of the cancer, RCC gives rise to diverse symptoms such as hematuria (blood in the urine), flank pain and flank mass. However, more than 40% of the patients with RCC are strictly asymptomatic, which makes early detection difficult. About 50% of RCC are incidental imaging findings and in one-third of the individuals, the cancer is only detected when the tumour is already locally advanced or metastasized, decreasing the patient's chances of survival [11]. Fortunately, during recent years, better screening and registration resulted globally in a significant rise in incidence and decrease in mortality rate [32, 31].

Apart from cancer-related complications, kidney cancer, and especially RCC, is strongly associated with both chronic and acute kidney disease [39]. Kidney disease involves decreased kidney functioning and can imply severe consequences for the patients. Not only cancer itself but also specific cancer treatments, especially systemic treatments such as chemotherapy, may induce kidney disease by damaging the functional units of the kidney because these treatments are often nephrotoxic.

2.3.1 Staging of renal tumour

RCC may arise from a variety of specialized cell types located along the length of the nephron. The most common type of RCC is clear cell renal RCC or also called conventional RCC, arising from the epithelium of the proximal tubule. Important in the choice of the therapy is the size of the tumour and the extent of invasion. Therefore, the TNM staging system is used. Here, T describes the size of primary tumour and its invasion of nearby tissues, N describes the nearby lymph nodes that are involved and M describes the spread of the tumour to other parts of the body or metastasis. 2.1 gives an overview of stages of tumours with their corresponding code according to the TNM staging system [11]. There are four main stages determining tumour size. For stage one (T1), the tumour is confined to the kidney and is smaller or equal to 7 cm. For these early-stage tumours partial nephrectomy is the treatment of choice. The 2nd stage tumours (T2) are also confined to the kidney but are larger than 7 cm maximally 10 cm in size. In the 3rd stage (T3), the tumour has invaded the veins or has extended the renal capsule, but stays within the renal fascia. Finally, stage 4 (T4) tumours have spread beyond the renal fascia [17]. Figure 2.4 shows a condensed renal tumour classification based on the TNM staging system into 4 main stages based on the size of the tumour, the lymph node metastases and the degree of metastasis.

Primary tumours (T)	Description
TX	Primary tumour cannot be assessed
To	No evidence of primary tumour
T1	≤ 7 cm and limited to kidney
T2	> 7 cm but ≤ 10 cm and limited to kidney
T3	Tumour extends into major veins and beyond the renal capsule
T4	Tumour invades renal gland and beyond the renal fascia
Regional lymph node (N)	Description
NX	Regional lymph nodes cannot be assessed
No	No regional lymph node metastasis
N1	Metastasis in regional lymph node (s)
Distant metastasis (M)	Description
Mo	No distant metastasis
M1	Distant metastasis

Table 2.1: TNM staging system with data retrieved from [17]

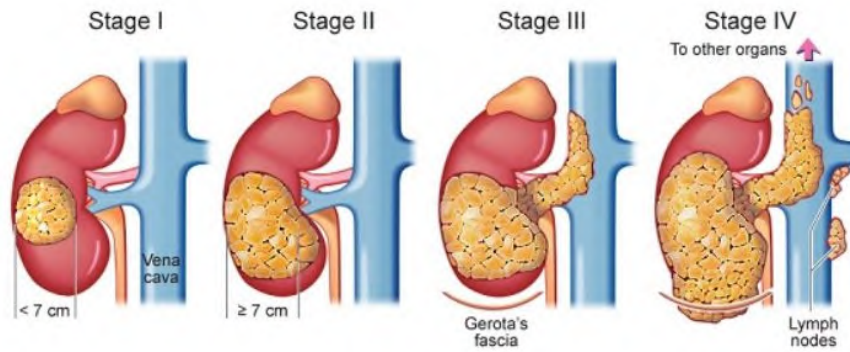


Figure 2.4: The 4 main stages of renal tumour. Retrieved from [47].

2.3.2 Treatments for renal cancer

The treatment of choice for kidney cancer is largely dependent on the stage of the tumour. For early-stage RCC or localized renal cell cancer, the tumour can be treated by ablation or surgical resection [31]. Surgical resection involves either complete removal of the kidney (radical nephrectomy) or removal of the diseased part of the kidney (partial nephrectomy). Ablation is particularly interesting for patients that are not suitable for anaesthesia and when minimal loss of renal function is desired. One of the used ablation techniques is thermal ablation. Here, heat induces necrosis of the tumour tissue by applying high-frequency alternating current, which in turn results in protein denaturation of the tumour tissue and cauterization of the tumour supplying vessels. [44]. However, the EAU guidelines for RCC [31] state that the cancer-specific mortality for patients treated with surgery is significantly lower than for patients treated with non-surgical treatments such as ablation. Therefore, surgery is the recommended therapy to treat and cure localized renal cell cancer.

In later stages, especially when metastasis toward other parts of the body occurs, treatments are often applied to prolong survival and serve as a palliative treatment [18]. These therapies are either local or systemic. Local therapies can target the primary tumour with surgical resection or embolization (the blockage of blood supply to the tumour) or they can treat metastases with therapies such as radiotherapy and immunotherapy. Systemic therapies include targeted therapies, immunotherapy, and chemotherapy. One typical targeted therapy blocks the vascular endothelial growth factor (VEGF), that stimulates angiogenesis or formation of new capillaries and is typically upregulated in many tumours to increase tumour perfusion [16]. For chemotherapy, the efficacy is usually limited since renal cell carcinoma is a chemotherapy-resistant tumour [20]. According to the guidelines for RCC, chemotherapy should not be offered as first-line therapy in metastatic RCC [31].

2.4 Partial nephrectomy

Partial nephrectomy (PN) or nephron saving surgery (NSS) involves the removal of the diseased part of the kidney, while maintaining the healthy tissue, and is recommended whenever technically feasible. Figure 2.5 shows an example of the surgical procedure. Historically, radical nephrectomy was the most commonly applied treatment, even for small T1 tumours [20]. With technical and clinical advances, partial nephrectomy has become the recommended treatment for small tumours (T1-type).

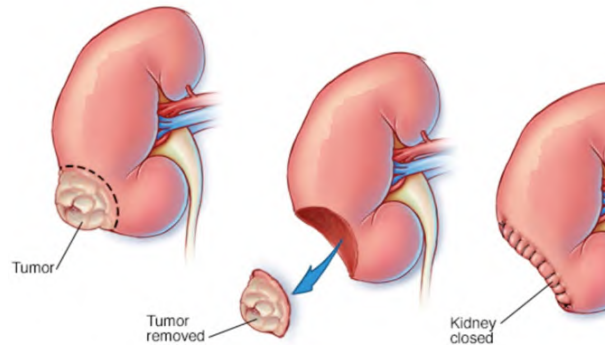


Figure 2.5: Partial nephrectomy surgery. Retrieved from [35].

Partial nephrectomy is a challenging surgery compared to radical nephrectomy since as much as possible functional tissue needs to be preserved without compromising the oncological outcomes. During the procedure, the surgeon typically blocks the arteries supplying the tumour to avoid excessive blood loss and allow a better view on the surgical site, enabling precise resection of the tumour. However, these arteries usually also supply healthy tissue leading to local ischemia of this healthy tissue what can result in loss of function of these tissues [39]. Hence, the ischemia time should be limited to 20 minutes to minimize the deterioration of renal function after surgery [6]. Consequently, the tumour resection should be executed sufficiently fast with adequate removal of the tumour to avoid tumour recurrence.

Despite the complexity, partial nephrectomy offers several advantages over radical nephrectomy. By removal of the complete kidney, the patient can either rely on the remaining kidney or will need dialysis to compensate for the loss of function. Therefore, PN is especially advised in patients with a high risk for postoperative renal insufficiency. That is the case when there are renal tumours in both kidneys, or when the only functioning kidney is affected by the tumour or when one kidney is affected by the tumour while the other kidney has already decreased functioning. Moreover, radical nephrectomy involves an increased risk of introducing chronic renal failure, which is a gradual loss of kidney function, and even complete kidney failure. These conditions are associated with an elevated risk of cardiovascular diseases and even death. Several studies have shown that partial nephrectomy does not compromise the oncological outcomes compared to radical

surgery, though it is not yet proven that the overall survival is higher in PN [31].

Historically, both partial and radical nephrectomy were executed as open surgeries. However, minimally invasive surgery has become widely used, though the procedure is technically challenging compared to open surgery. This complexity may be overcome by the use of robotic systems, which increase the surgeon's dexterity within the abdominal cavity [45]. Open, laparoscopic and robot-assisted surgery are applied for both partial and radical nephrectomy. The minimally invasive approaches, laparoscopic or robot-assisted, are usually preferred, unless the peri-operative, functional or oncological outcomes may become less favourable. Whenever any surgical technique of partial nephrectomy is feasible without compromising outcomes, radical nephrectomy should not be performed [31].

2.5 Study of the renal vasculature

Partial nephrectomy is a complex procedure and its success relies upon a good understanding of the renal vasculature as stated by [10]. Sufficient information on the relation between vasculature and parenchymal volume enables selective clamping of the tumour perfusing arteries and hence, might help the surgeon to reduce the ischemia time.

2.5.1 Anatomy of renal vasculature

As mentioned earlier, the kidneys receive a large percentage of the cardiac output in order to maintain body fluid constitution. A change in renal blood flow changes the glomerular filtration rate and that in turn influences the volume and composition of body fluids. Therefore, the kidneys have the capacity to regulate their own blood flow, this process is called autoregulation, and can be achieved by inducing mechanisms such as vasoconstriction and vasodilation [13]. The kidneys are supplied by the renal arteries directly branching from the abdominal aorta. Like the ureter, the blood vessels enter or leave the kidney at the renal hilus. The renal artery typically divides into an anterior and posterior branch before entering the renal hilum. The anterior branch receives about 75% of the blood volume and divides in four segmental arteries (upper, middle, lower and apical). The posterior branch forms the posterior segmental artery. The segmental arteries divide further into lobar, interlobar, arcuate, interlobular and finally into afferent arteries supplying the glomerular capillaries where the glomerular filtration happens [26].

Historically, the kidney vasculature was thought to be organized according to the Graves' description. This theory states that the kidney parenchyma is subdivided into 5 segments, each of them supplied by a different segmental artery. Figure 2.6 shows the typical division of the kidney parenchyma into 5 segments. However, there is estimated that in only 42 % of the population the parenchyma is subdivided according to the Graves' description.

Thus, a tumour located in one specific segment can be vascularized by arteries destined for different segments [10]. This complicates surgery because more than one segmental artery should be clamped to block the blood supply to that tumour. That may result in more ischemia of healthy tissue, compromising surgical outcomes.

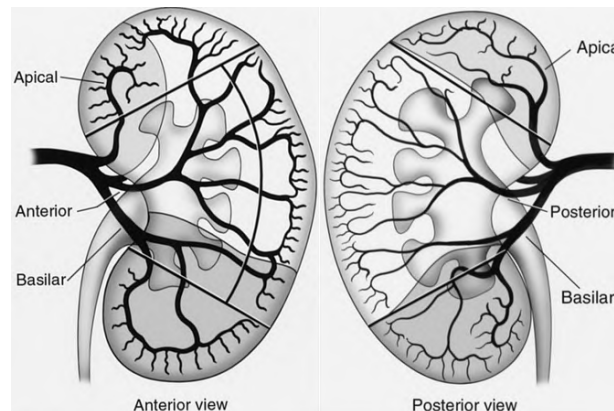


Figure 2.6: Illustration of the Grave's theory dividing the kidney into 5 segments. Retrieved from [14]

Moreover, the normal pattern where the kidneys are supplied by a single renal artery, which splits into branches around the hilum, accounts only for 62.5 % for right kidney and 72.5 % for left kidney of the cases. There are different possible variations such as the two depicted in figure 2.7. One shows an extrahilar artery, which is a branch that bifurcates from the renal artery before the renal hilum and goes into the kidney outside the renal hilum. The other is a superior artery, which is a small artery that directly comes from the aorta to supply the kidney separately from the main renal artery [15]. All these factors make surgical planning more difficult and make the development of a model of the renal vasculature a challenging task.

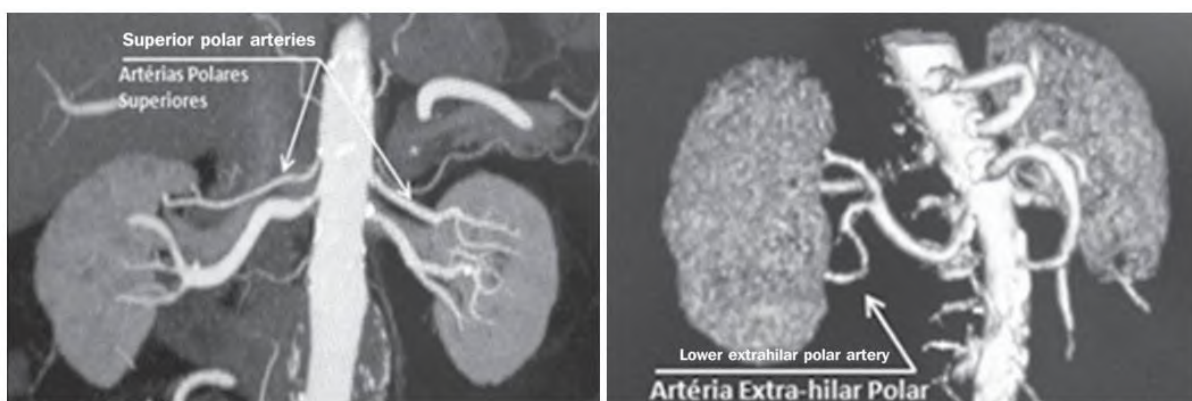


Figure 2.7: Two examples of anatomical variations of the renal vasculature: (left) extrahilar artery and (right) superior polar artery. Retrieved from [15]

2.5.2 Modelling of the vasculature

The previous paragraph was aimed at obtaining a better understanding of the vascular anatomy. Another way of analyzing tumour perfusion is by building a model of the arterial network based on imaging data. In this section, the construction of these vascular models is studied in order to obtain a better understanding of vascular modelling.

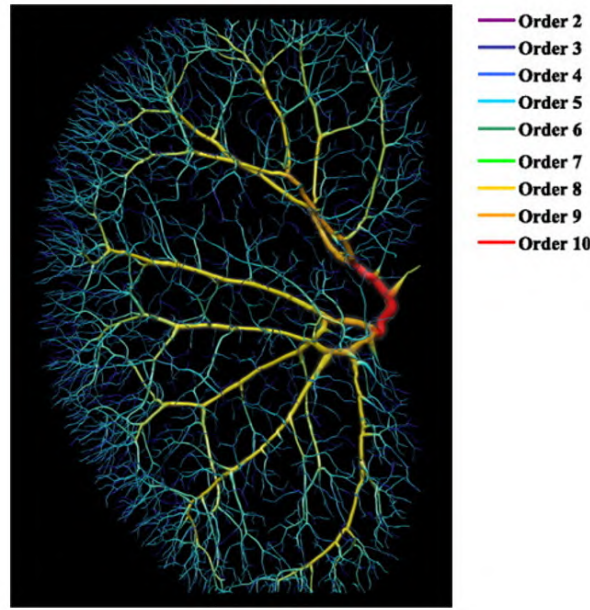


Figure 2.8: Venous tree of the kidney with the color designating the vessel ordering. Retrieved from [36].

One example of modelling of the kidney vasculature was executed by Nordsletten et al. [36]. They analysed the renal vasculature of the rat based on microcomputed tomography (μ CT) and built a model of this vasculature using automated segmentation. The study was conducted to analyse the effects of hypertension and diabetes on the vasculature, though the general principles can be used for other applications. The procedure was executed as following. First, the vasculature of the organ tissue was delineated using a radio-opaque silicone polymer and thereafter the vessel walls were visualized using μ CT iso-surface rendering, a technique where millions of point are dispersed over the arterial and venous walls. Based on this rendering the vascular tree was skeletonized while calculating the vessel diameters, lengths and connectivity. These steps result in a stream of points at the center-line of all vessels. In the last step, the original vasculature was reconstructed by connecting points and all points were associated with a vessel segment resulting in a line network of the renal vasculature. To characterize the topology, the principle of blood vessel generations is introduced, where each branch is labelled with a certain order according to the hierarchy. That results in an ordering as shown in figure 2.9. The principle of these generations is explained later in this paragraph.

Ordering methods

Typically, the branching topology is characterized by the introduction of the principle of blood vessel generations, that was already applied in the study by Nordsletten et al. in 2006 [36] to describe the topology of the kidney vasculature. Figure 2.9 shows three possible ordering methods to assign blood vessel generations. The top-down method travels downstream starting from the trunk of the vasculature by allocating generation 1 to the trunk and assigning generation 2 to its daughter branches. The general principle is that, when the parent branch is labelled n , then the daughter branches are assigned generation $n+1$. The Strahler ordering is a bottom-up method, assigning the lowest order to the terminal branches. Each vessel is followed upward until the next bifurcation where the parent is given a higher order, under the condition that both daughter branches coming together have the same generation. When two daughter branches have a different order, the parent branch is allocated with the generation of the daughter branch with the higher order [38]. The 'diameter defined Strahler ordering' takes into account the diameters when assigning the generations, allowing for more adequate allocation of generations. Geert Peeters [38] developed a diameter defined top-down ordering method.

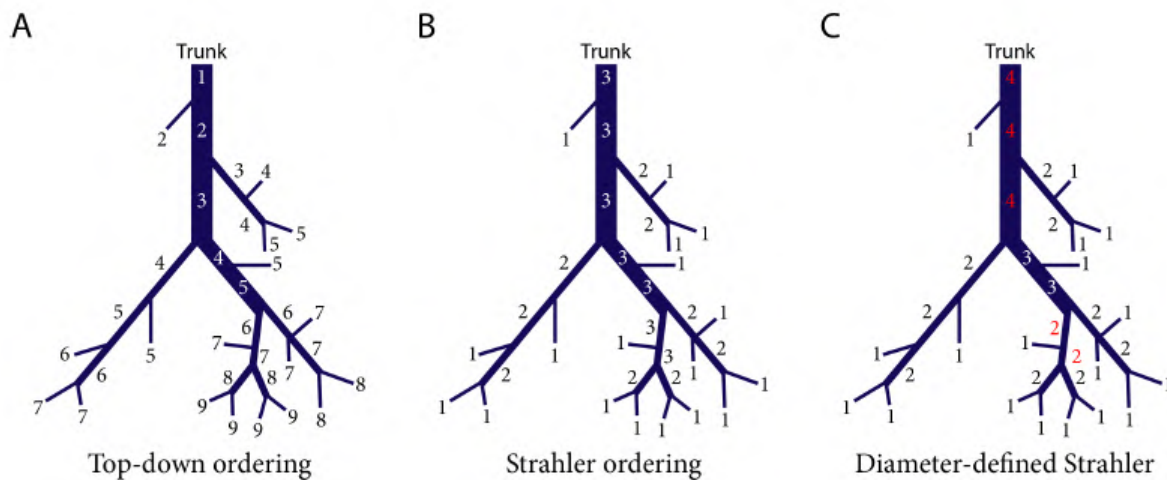


Figure 2.9: Overview of different ordering methods, (A) top-down ordering method, (B) the Strahler ordering and (C) the diameter-defined Strahler ordering. Retrieved from [38].

Modelling the arterial tree of the liver

A substantial part of research in this area is conducted for the liver and its vasculature. Several models for liver vasculature are developed with applications such as liver cirrhosis [38] and tumour resection [46]. The techniques used for the liver may serve as an inspiration and provide concepts to be applied for the kidney vasculature modelling.

Geert Peeters [38] studied the relationship between hepatic vasculature remodelling and the progression of cirrhosis, a disease characterized by chronic loss of liver function due to replacement of the healthy hepatic architecture by scar tissue and regenerative modules. Therefore, they developed and implemented a methodological framework, that allows to model and analyse the vasculature and blood flow of the rat liver during the progression of cirrhosis. Morphological data of the hepatic vasculature was obtained using two experimental approaches, namely immunohistochemistry and vascular corrosion casting. The latter one produces a 3D replica of the vascular system by injecting polymeric resin, that subsequently polymerizes. The replica is then scanned using high-resolution μ CT. That allows processing of the retrieved dataset resulting in a segmented dataset and a virtual 3D model of the vasculature. The microvasculature was studied using immunohistochemistry followed by confocal laser scanning. The obtained data were semi-automatically segmented using the in house developed software tool DELIVER. The obtained 3D reconstruction of the hepatic circulation of the rat liver is shown in figure 2.10.

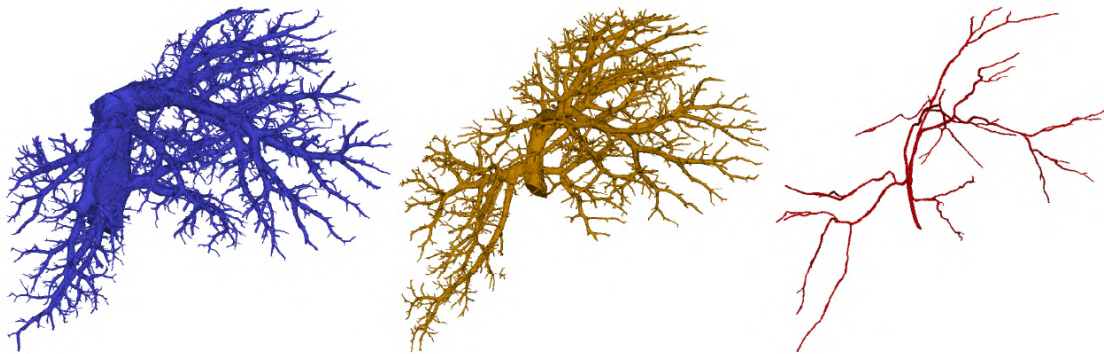


Figure 2.10: 3D Reconstruction of the hepatic circulation with hepatic venous (blue), portal venous (yellow) and hepatic arterial system (red). Retrieved from [38].

Following the segmentation of the μ CT scans and the confocal laser scanning, both datasets were analysed using the DELIVER tool. The segmented vasculature was converted into a graph structure as depicted in figure 2.11. First, the segmented blood vessels were skeletonized by the use of a 3D thinning algorithm, that calculates the centre line of the vasculature by removing the surface voxels until only the centre lines remain. During this process, it is important that the algorithm maintains the segment length. Next, the voxels situated at intersections or dead ends were identified. That in turn allowed to build a graph structure, where each branch consists of different nodes in between the previously determined intersection and/or death-end voxels. For each branch, the mean radius was computed allowing to apply a diameter-defined top-down ordering, resulting in an ordering method that combines the top-down ordering and diameter-defined (Strahler) ordering.

This approach for defining graphs structures from segmented CT data is also interesting for other applications and a similar approach is used for the planning tool explained in chapter 3.

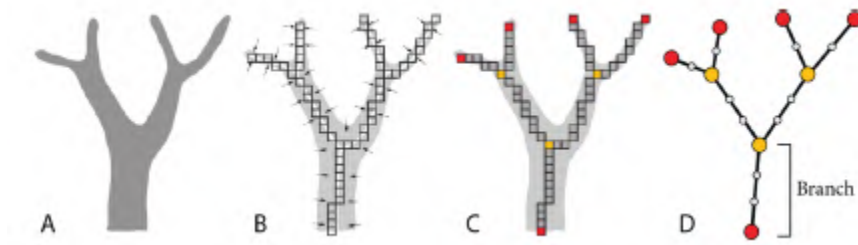


Figure 2.11: Thinning algorithm for skeletonization. Retrieved from [38].

The methodological framework allowed them to make a detailed reconstruction of the hepatic circulation and analyse quantitatively the vasculature of the rat liver depicted in figure 2.12.

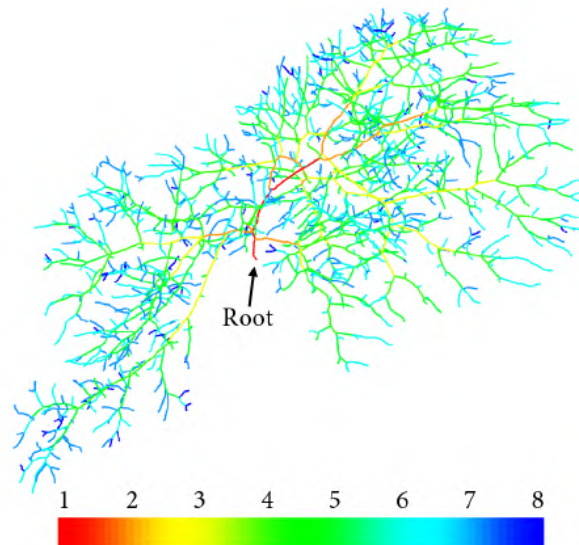


Figure 2.12: Top-down ordering applied to the portal tree. Retrieved from [38].

The study by Selle et al. [46] analyzed the liver vasculature in the context of surgical planning, and therefore developed a vascular model and proposed a model-based approach to determine the vascular territories, i.e. the vascular perfusion zones of the portal vein. A vascular model is particularly interesting for planning of surgeries such as living-related liver transplant surgery (LRLT) and oncologic resection. In LRLT, a healthy person donates a part of his or her liver. This is possible thanks to the liver's regeneration capacity when a part is removed, but for successful partial removal, a good knowledge of morphology and branching pattern of the liver vasculature is key.

In a similar way as in the study of Geert Peeters [38], CT data was first segmented and transformed into a graph structure. The graph structure was created from the segmented vessels by first using a 3D thinning technique, followed by identification of the voxels at branching nodes and endpoints. The obtained graph structure exists of nodes corresponding with branching points and end points and in between them segments connecting these points. The resulting graph structure was used to determine the vascular territories supplied by the main branches of the liver as will be explained more in detail in section 2.6.

2.6 Methods for determining perfusion areas

Following the structural analysis of the vascular network, one can study the organ perfusion. In this paragraph, different approaches are described to divide organs into vascular segments according to the arterial perfusion.

2.6.1 Anatomical approaches

Kidney perfusion was historically thought to be organized according to the Graves' description. According to Borojeni et al. [10], however, tumours can be supplied by several arteries originating from segments different from its own segment. This is possibly a result of angiogenesis promoted by the tumour. Moreover, they found out that with increasing tumour size, the probability increases that the tumour is supplied by different segmental arteries. In conclusion, simply dividing the tumour into vascular segments according to the Graves' description is not recommended to determine the vascular territories.

During procedures such as partial nephrectomy, a frequently used technique is near-infrared fluorescence (NIRF) imaging by intraoperative administration of indocyanine green (ICG). This is a safe and non-nephrotoxic technique with low adverse effects allowing to visualize local tissue ischemia after selective clamping. An example is shown in figure 2.13. Here, the ICG is administered during selective clamping of arteries. When part of the tumor colors in green, it is still perfused which implies that selective clamping only resulted in partial ischemia of the tumour. Hence, for bloodless tumour resection, the surgeon needs to clamp the main supplying artery of the kidney resulting in global ischemia of the kidney [9].

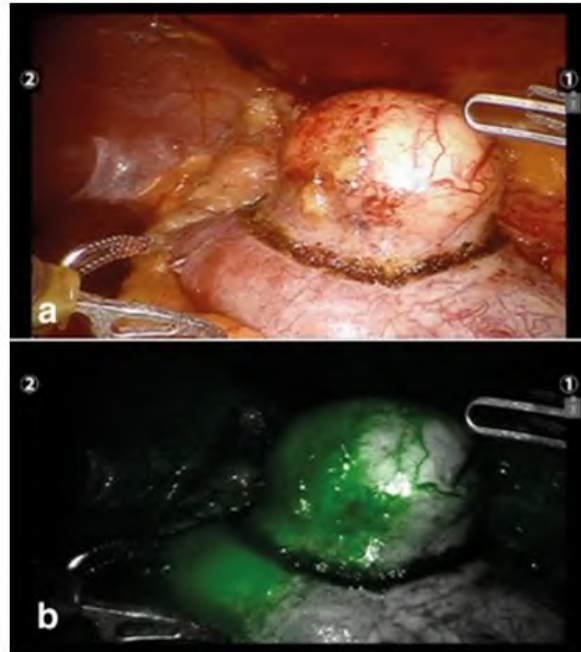


Figure 2.13: View of renal tumour after selective clamping of the arterial segment with (a) normal view and (b) the infrared light is set on. ICG shows incomplete clamping of the tumour, as it still colors green. Retrieved from [33].

It is clear that NIRF imaging with ICG administration is particularly useful to facilitate decision making. However, this technique has several limitations. Firstly, the clamping time must be minimized to avoid tissue dysfunction afterwards. Hence, the surgeon should make fast decisions based on the ICG measurements whether to start cutting or to cause total kidney ischemia. Further, only the surface of the tumour and kidney is visualized, though the non-visible parts of the tumour, located deeper under the surface, may be supplied by other vessels. In such cases, bleeding during tumour resection is possible. Currently, the initial clamping of the surgeon is based on the sliced CT data and the limited view through the robotic console. Therefore, the decision of the surgeon is often dependent on his/her intuition and experience. It is clear that ICG measurements have proven to be useful. Nevertheless, some major drawbacks are present which can be overcome by a presurgical planning tool which suggests the ideal clipping locations and is the objective of this master's thesis.

2.6.2 Model-based approaches

The foundation for the planning tool is a map of the perfusion areas of the kidney based on the anatomy of the kidney and the arterial tree. In this paragraph, an overview is given of the different approaches that have been applied previously to define these perfusion zones. These approaches are applied on organs different from the kidney but can serve as inspiration for determining the kidney perfusion areas.

Skeletal muscle oxygenation

A paper by Zeller-Plumhoff et al. [49] reviews the current progress in image-based modelling of skeletal muscle oxygenation. The studied models investigate the influence of the microvascular structure on the tissue oxygenation by coupling vascular network models to muscle function. The blood vessel network model is obtained starting from imaging data of muscle tissue and blood vessels. Next, these images, i.e. μ CT, are manually or (semi-) automatically segmented, and that allows to analyse the 3D structure of the blood vessel and apply a mesh to the tissue for finite element modelling to model muscle oxygenation.

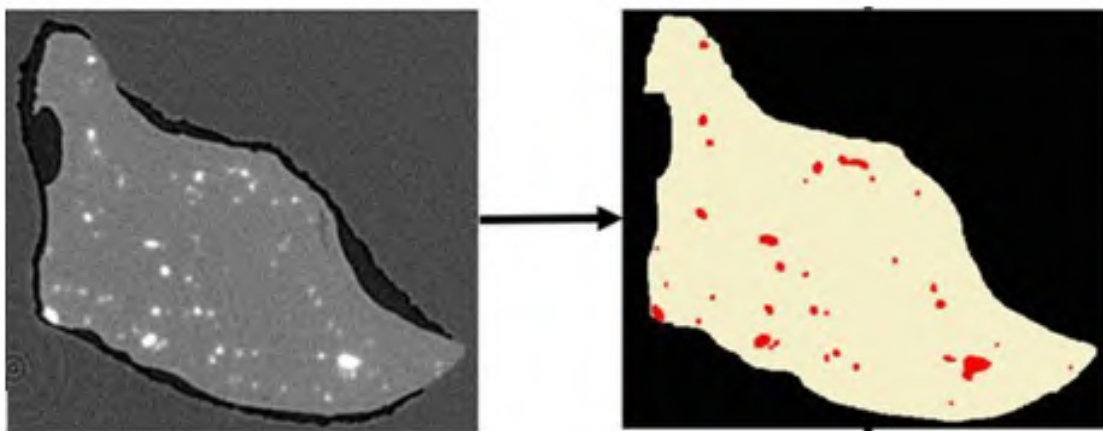


Figure 2.14: blood vessels and muscle tissue are segmented from images i.e. μ CT images. Retrieved from [49]

Thereafter, the vascular network can be linked to muscle function. In the most simplified model, the oxygen transport from the capillaries to the muscle tissue can be described by radial diffusion along the axis of the blood vessels, resulting in cylindrical diffusion domains. More realistic is the concept of domains of influence, such as the Voronoi polygons. Each capillary defines a polygon that consists of all discrete tissue points that are closest to that capillary and more distant from the other capillaries. The assumption is then made that all tissue points within each polygon are supplied by the capillary in this polygon. Figure 2.15 shows an image of 2D Voronoi polygons compared with numerically computed streamlines that define trapping regions. The capillary within this region supplies it with oxygen. They found out that in 2D the Voronoi polygons, forming tessellations, are relatively good representations of capillary oxygen supply regions, but that more research should be done whether this method is sufficient to describe oxygenation volumes in 3D. Typically, the 3D models are obtained by combining the 2D results from different points along the vessel axis.

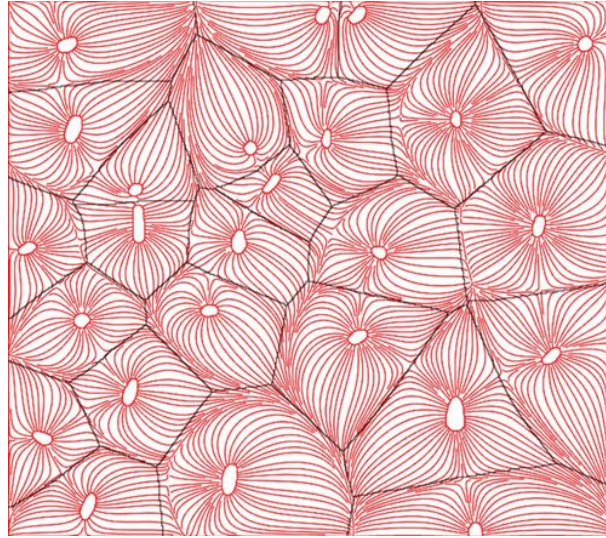


Figure 2.15: Voronoi polygons to define perfusing regions of capillaries. Retrieved from [49].

Perfusion zones of the portal tree in the liver

Selle et al. [46] proposed a model-based approach to determine the perfusion areas or vascular territories in the liver. Therefore, they first constructed a graph structure of the vascular network as a starting point to determine these vascular territories (section 2.5.2).

Following the structural analysis of the portal tree, they estimated the liver's vascular territories supplied by the main branches of the portal tree of the liver. First, they described the problem in an abstract manner by introducing a function g . This function assigns each liver voxel v to the appropriate liver segment S_i . Each segment represents a subvolume of the liver L that is supplied by branch B_i of the portal tree B . Practically, each voxel v of the liver L will be assigned to a segment number i as depicted in equation 2.1.

$$g : v \in L \rightarrow \{1, \dots, n\} \quad (2.1)$$

In the absence of detailed information of the branching that would directly deliver information about the vascular territories as depicted in figure 2.16, they used modelling approaches to determine g . These approaches are based on the anatomical information of the portal tree and the liver. Therefore, they made use of two different methods to approximate the liver segments. One method is the nearest neighbour segment approximation (NNSA), the other approach is called the Laplacian segment approximation (LASA).

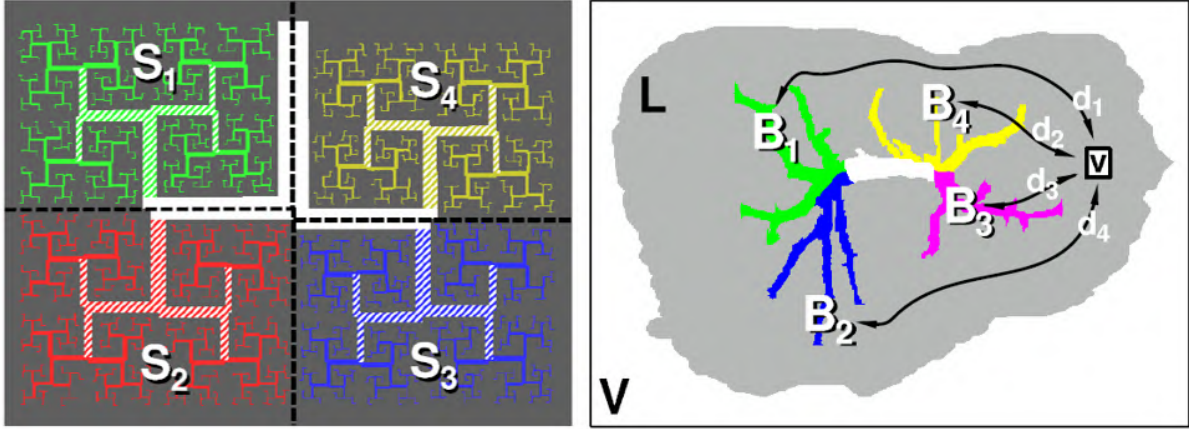


Figure 2.16: The ideal situation (left), where the vascular territories can be directly determined from the detailed branching structure versus reality where modelling is required (right). Retrieved from [46]

The NNSA approach assigns each voxel to the closest branch B_i to that voxel. First, for every voxel, they determined the shortest Euclidean distance d_i to every branch B_i as depicted in equation 2.2. That results in a map of these distances $d_i(v)$ for each branch as depicted in Figure 2.17.

$$d_i(v) = \min_{v' \in B_i} \|v - v'\| \quad (2.2)$$

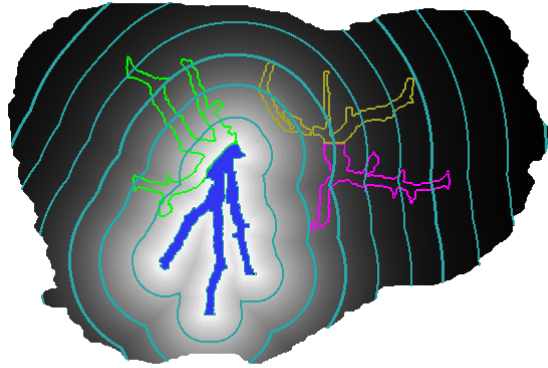


Figure 2.17: The shortest euclidean distances for every voxel to branch B_i : the brighter the voxel, the closer the voxel is to the branch. Retrieved from [46].

Next, the function g_{NNSA} assigns every voxel v to the closest branch k based on the calculation of $d_k(v)$, the minimum of the distances to all branches, calculated as $d_k(v) = \min \{d_1(v), \dots, d_n(v)\}$.

$$g_{NNSA}(v) = k \quad (2.3)$$

The segment S_i represents the liver voxels that are assigned to index branch i as depicted in equation 2.9. That results in a map of the liver segments as shown in figure 2.18

$$S_i = \{v \in L \mid g_{NNSA}(v) = i\} \quad (2.4)$$

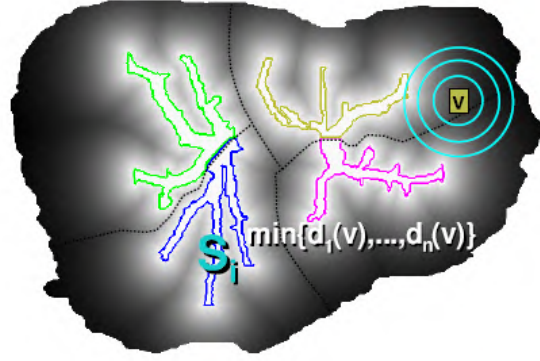


Figure 2.18: The segments are defined based on the minimal distances. Retrieved from [46].

The LASA approach is more complex and aims to determine for each segment i a harmonic function ϕ_i , that is a solution of the Laplace equation (equation 2.5). The Laplace equation can be solved by imposing specific boundary conditions, making this equation particularly useful for this application.

$$\Delta\phi_i(v) = \nabla^2\phi_i(v) = 0 \quad (2.5)$$

For segment i , the probability that a certain voxel v is perfused by branch B_i is the highest when the voxel is located on that specific branch. Therefore, the harmonic function ϕ_i should be maximal at branch B_i , resulting in the first boundary condition depicted in 2.6. At the other side, the probability should be equal to zero when the voxel is located on a branch j different from i or when a voxel is not part of the kidney. Therefore, the harmonic function ϕ_i should be zero at branch B_j with $j \neq i$ and outside the liver, as depicted in equation 2.7

$$\phi_i(v) = 1 \quad v \in B_i \quad (2.6)$$

$$\phi_i(v) = 0 \quad v \in B_j \text{ with } j \neq i \text{ or } v \notin L \quad (2.7)$$

The Laplace equation can now be solved based on these boundary conditions what result in a map for segment i shown in figure 2.19.

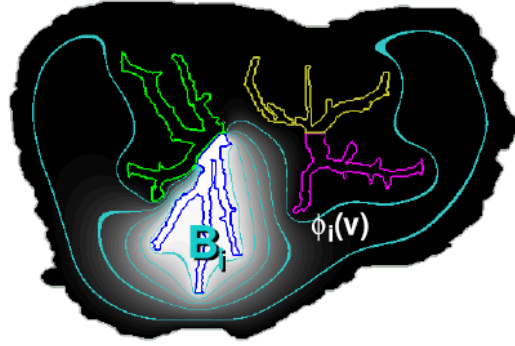


Figure 2.19: The result of solving the Laplace equation for branch B_i . Retrieved from [46].

The harmonic function ϕ_i increases as a voxel is closer to the corresponding branch B_i . Hence, as shown in equation 2.8, the function g_{LASA} assigns every voxel v to branch k where ϕ_i is maximal, so that applies $\phi_k(v) = \max \{\phi_1(v), \dots, \phi_n(v)\}$. Finally, each voxel in the liver L is assigned to its corresponding branch based on the function g_{LASA} , resulting in figure 2.20.

$$g_{LASA}(v) = k \quad (2.8)$$

$$S_i = \{v \in L \mid g_{LASA}(v) = i\} \quad (2.9)$$

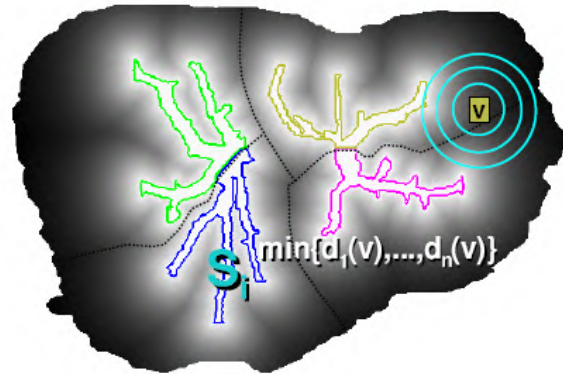


Figure 2.20: The resulting map of the liver divided into segments using the LASA approach. Retrieved from [46].

They also optimized the Laplacian segment approximation by slightly changing the boundary conditions. They introduced an additional boundary condition depicted in equation 2.10 that the harmonic function ϕ_i should be zero at the height of the hepatic vein V . This makes anatomically sense since the hepatic vein drains the blood from the liver. Further, they considered the local radius of the branches $r(v)$ for the boundary conditions

as depicted in equation 2.11. In that way, they took into account that larger branches perfuse a larger area by transporting more blood and that reduces the influence of smaller branches.

$$\phi_i(v) = r(v) \quad v \in B_i \quad (2.10)$$

$$\phi_i(v) = 0 \quad v \in B_j \text{ with } j \neq i \text{ or } v \notin L \text{ or } v \in V \quad (2.11)$$

They validated the approximation methods by vascular corrosion casts of the human livers from cadavers. The vascular corrosion casting allowed very precise approximation of the true anatomical segments. They applied the three described approaches for three levels of pruning as depicted in figure 2.21 and compared these results with the outcomes of vascular corrosion casting based on the volume overlap as shown in table 2.2.

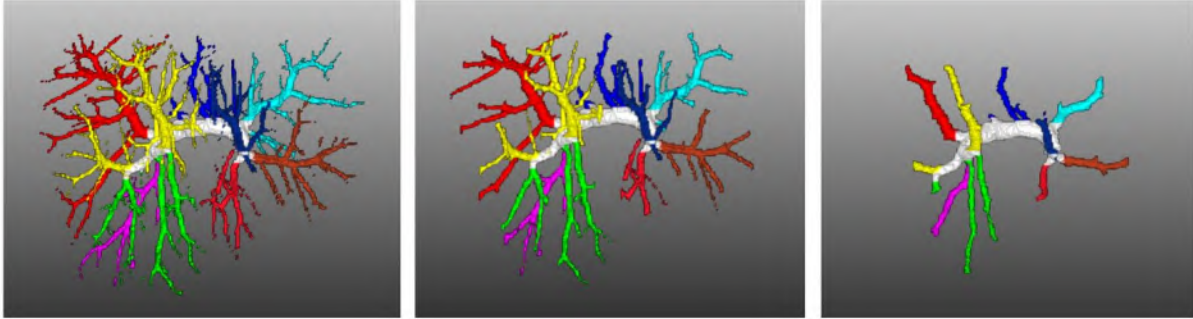


Figure 2.21: The results of vascular corrosion casting for different pruning levels from left to right: low, medium and high pruning. Retrieved from [46].

Pruning levels	High	Medium	Low
NNSA	79 %	89.9 %	93.4 %
LASA	77.7 %	88.6 %	91.7 %
Optimized LASA	81.7 %	90.8 %	92.7 %

Table 2.2: Percentages of the volume overlap between outcomes of the described LASA and NNSA methods and the results of vascular corrosion casts, results retrieved from [46]

A higher percentage of volume overlap corresponded with a more realistic outcome of a method. They showed to have good results with volume overlap around 80-90 % depending the level of pruning. The NNSA approach performed better when the tree was more detailed. At the other side, when starting from a highly pruned portal tree, the optimized LASA method had slightly better results with up to 2.7 % more overlap compared to NNSA. However, the LASA method required more computational power and therefore the NNSA method seems to be the more suitable approach in practice.

They also evaluated their methods in a clinical setting. For the liver resection surgery, they concluded that automatic segmentation of the liver, tumours and vasculature allows for better planning and improved preparation. They also suggested that the knowledge of the vascular anatomy enables better evaluation of potential donors for living-related liver transplant surgery.

2.7 Current surgical planning tools

Together with surgery becoming less invasive and more precise, the need for more precise surgical planning is evident. Useful tools for surgical planning are 3D models. They help the surgeon to gain insight into the patient-specific anatomy. An overview of these methods is given in a paper by Porpiglia et al. [40]. The models can be constructed from MRI and high-resolution CT images. Thereafter, the models can either be printed using 3D printing or maintained as virtual images that overlap on the endoscopic view, resulting in augmented reality (AR) surgical view. These 3D models have already been used for prostate cancer surgery and kidney surgery. However, the major limitation of these models is the accuracy when image acquisition or segmentation is not optimal. Further, automated intra-operative superposition is not yet used in daily practice as the model needs to adapt and align with constantly changing intra-operative views and physiologic movements of the organ.

A more elaborated tool, hyper-accuracy three-dimensional (HA3D) reconstruction, was used by researchers of the University of Turin to test its efficacy to clamp selectively during robot-assisted partial nephrectomy (RAPN) [41]. They used specific scan protocols and CT contrast injection, to obtain high-resolution CT scans. An overview of these settings can be found in table 2.3. These images were further processed to obtain a virtual 3D model of the kidney. By reliable reproduction of the arteries, they could follow the segmental arteries until they contacted the tumour surface, allowing the identification of the arterial branch/branches supplying the tumour. Further, as shown in figure 2.22, they superimposed the virtual model on the real anatomy, that overlapped with great accuracy, showing a very reliable model. The tool allowed them to make a preoperative simulation of selective ischemia. Moreover, the clamping following the simulation resulted in successful ischemia of the tumour tissue and little ischemia of healthy tissue. Thereafter, the successful selective clamping of the tumour supplying arteries was proved by the use of fluorescence imaging. They aim to integrate the reconstructed images into the robotic console.



Figure 2.22: The dissection of the renal branches is guided by the 3D reconstruction: the upper image shows the normal anatomy and the images below shows the super-accuracy 3D reconstruction superimposed on the true anatomy. Retrieved from [41].

Settings		
Images	detector configuration	64 x 0.625
	rotation time	0.75 s
	section thickness	0.7 mm
	intersection gap	0.3 mm
	helical pitch	0.609
	scan field of view	50 cm
	x-ray tube voltage	120 kV
	x-ray tube current	300 mA
Contrast	delay arterial phase	7 s
	delay nephrographic phase-	70 s
	delay delayed phase	600 s
	injection at rate	4 ml/s

Table 2.3: Overview of image acquisition and contrast agent (non-ionic with 350 mg I/ml or 370 mg I/ml) settings used in [41] to obtain high-resolution CT images.

A commercial company, Visible Patient, developed specialised software to produce patient-specific 3D models extracted from CT or MRI images. They obtained a CE mark for their software, meaning that it meets safety, health and environmental requirements allowing them to sell it within the European economic area. They offer an online service for 3D patient modelling, where physicians can send their data returning back 3D models. This service is certified ISO 13485, which is an internationally agreed standard defining quality requirements for the medical devices industry [23]. Moreover, they developed software for surgical planning to assist physicians in choosing the optimal strategy for surgery [48]. Two examples of their outcomes are depicted in figure 2.23, showing the segmented kidney and a model of the perfusion zones of the liver.

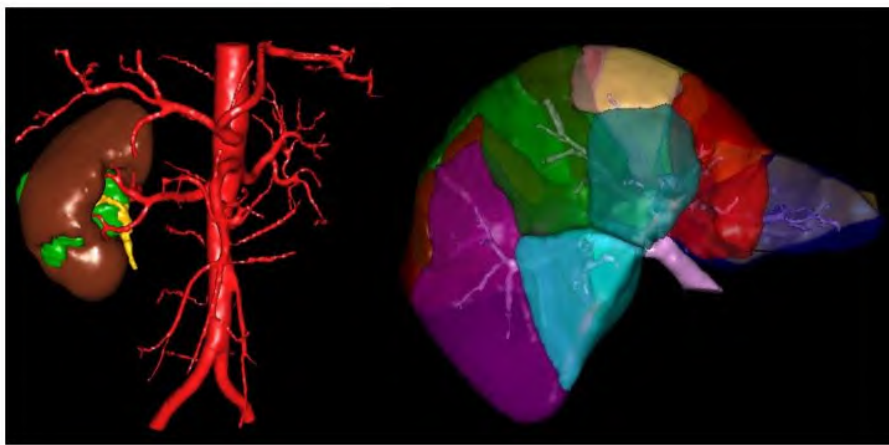


Figure 2.23: 3D models produced by Visible Patient: (left) 3D model of kidney with tumour and its vasculature, and (right) liver divided into perfusion zones supplied by the branches of the portal vein. Retrieved from [48].

They apply similar techniques used in the liver and lungs on the kidney too, making it a suitable planning tool for partial nephrectomy. However, since Visible Patient is commercial company, they charge a significant amount of money for each 3D model they produce. This cost makes using this service on the CT data of each patient not economically feasible. Moreover, the results that they return, can only be visualized using their specialised software, and that doesn't allow to use the obtained data for other purposes or for more elaborated tools. These limitations explain the need for an in-house developed software for planning of partial nephrectomy.

2.8 Implementation for clinical practice

The ongoing progress in surgical planning is promising but it remains challenging to make these research solutions ready for clinical use. This is certainly something that should be taken into account for the development of an in-house model. One solution is implementation of the model in an existing platform that already offers the functionalities for clinical use.

The R&D department of Siemens Healthineers has developed a platform *syngo.via* Frontier for advanced post-processing prototypes. As a client of *syngo.via*, people can use these prototypes for research and clinical applications within the *syngo.via* environment. Moreover, with the *syngo.via* Frontier Development Kit, it is possible to develop and upload prototypes on the *syngo.via* Frontier server. This can be achieved by reusing existing code or integrating own algorithms in the environment. The development of these prototypes can be done among others in MeVis MDL, python and C++. Important to be noted, *syngo.via* Frontier is currently destined for research use only and not for clinical use [21].

An interesting option for implementation in this Frontier environment is MeVisLab, which is a modular framework for medical image processing and visualization development. This framework is the result of a collaboration of MeVis Medical Solutions AG, a German company that provides software products for image-based medicine and the German research institute for Digital Medicine, Fraunhofer Mevis. MeVisLab can be used to build clinical application prototypes by the construction of modular networks combined with scripting. These networks are constructed from existing image processing modules, built based on underlying image processing algorithms, and new modules, that can be built using among others Python scripting or C++ programming. A major advantage is that this framework allows to load first image data, process and analyze these images and finally visualize them. Moreover, several image formats such as tiff, dicom and bmp are supported. All these factors together with the implementation into *syngo.via* Frontier environment make MeVisLab a suitable choice for construction and implementation of new prototypes [2].

Chapter 3

Materials and Methods

In today's clinical practice, the available techniques have several limitations, proving that there is clearly a need for better pre-surgical planning. This chapter presents a model that aims to support pre-surgical planning of partial nephrectomy by informing the surgeon on arterial perfusion based on anatomical information of the parenchyma and the arterial tree.

Figure 3.1 shows a high-level overview of the complete workflow. In the next sections, each step in this workflow is described in detail. Section 3.1 discusses the source of anatomical data and the first step in the workflow. This step is realised in Mimics and includes the generation of a skeleton from the arterial tree and exportation of the anatomical data in slice format. These data are the input of the model. In section 3.2, the functioning of the perfusion model is discussed in detail starting from the manual adjustments of some patient-specific settings. At last, 3.3 shortly introduces the 3D visualization of the outcomes in Mimics and discusses possibilities to validate these results.

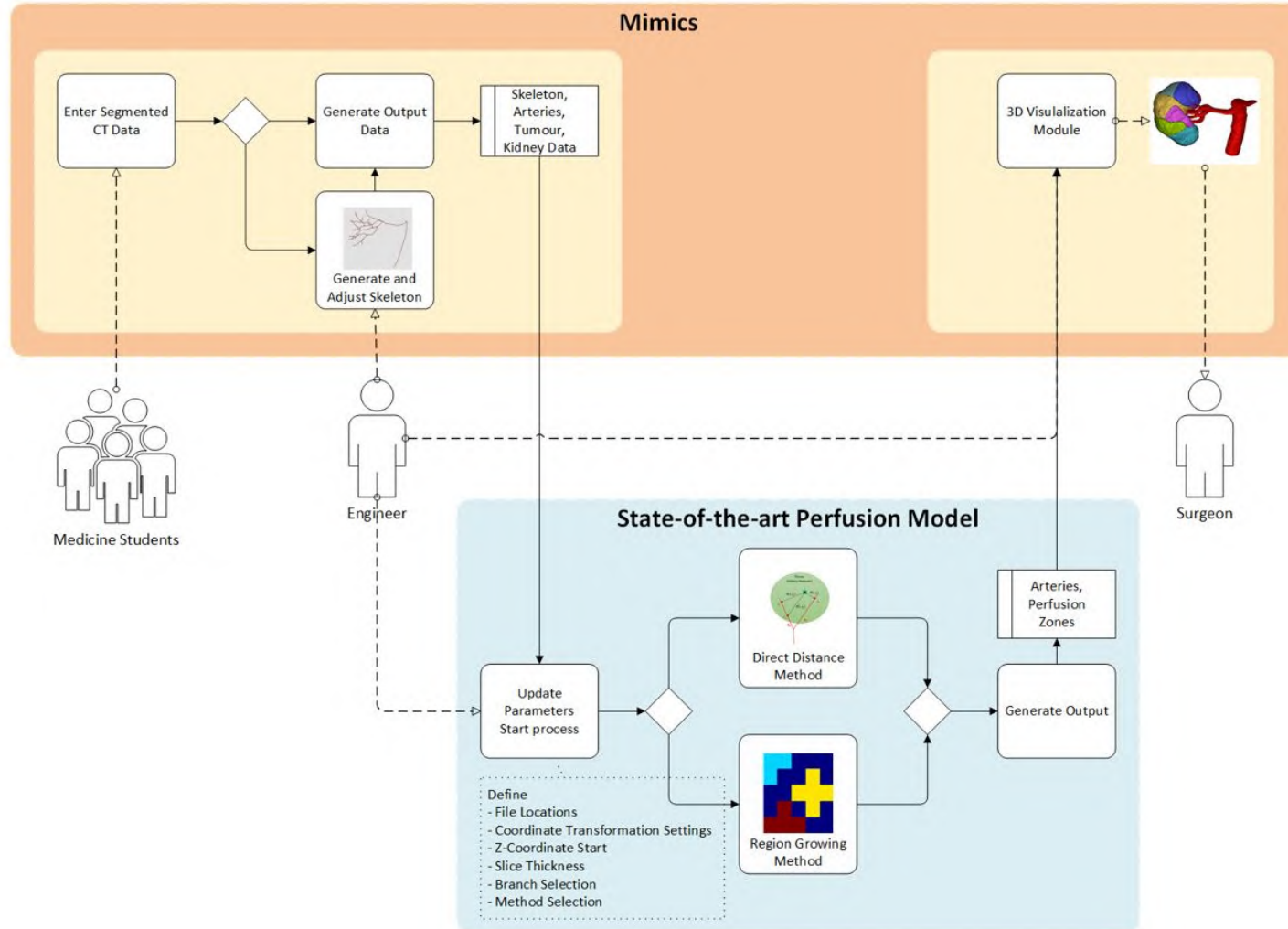


Figure 3.1: Overview of the complete workflow existing of three main steps: the preparation and import of anatomical data in Mimics, the new perfusion model and the 3D visualization.

3.1 Anatomical data

The input of the model exists of anatomical information about the arterial tree, the tumour and the kidney tissue, that comes from segmented CT images of these structures. The segmentation of kidney, tumour and the vascular tree allows to build a 3D model of these structures as depicted in figure 3.2.

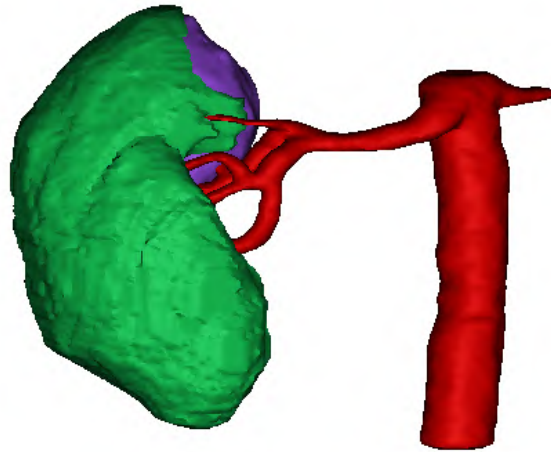


Figure 3.2: 3D model of the kidney parenchyma (green), the tumour (purple) and arteries (red) obtained in Mimics Research after segmentation.

3.1.1 Segmentation

The segmentation is performed using Mimics Research, which is specialised image processing software developed by Materialise [1]. Starting from contrast-enhanced CT images of the abdomen, two master students of medicine, Maryse Lejoly and Stefanie Vanderschelden, have segmented several kidneys and their vasculature. Their master thesis involves the clinical side of the planning tool for partial nephrectomy and they are responsible for the segmentation of the CT data, serving as input for the model. The contrast-enhanced CT images are obtained during clinical examination of patients with kidney cancer before they underwent partial nephrectomy. Figure 3.3 shows two CT slices of a patient with a tumour in the right kidney. One is a contrast-enhanced CT image and the other shows the segmentation into the kidney, the arterial tree and the tumour. The axial 2D slices with segmentations of the kidney, the tumour and the arterial tree are exported from Mimics as image files in bitmap (BMP) format, a format that can be imported in the model.

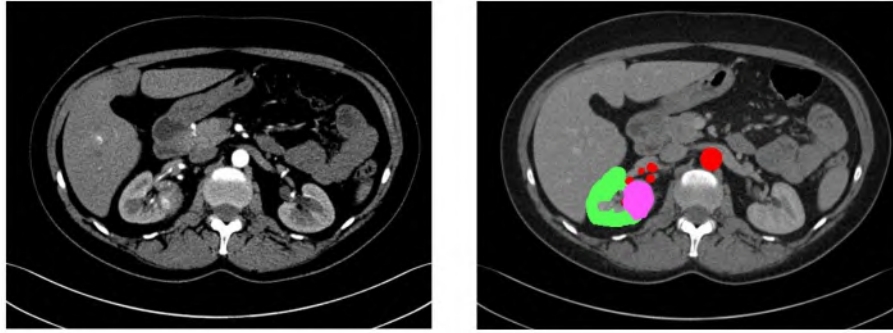


Figure 3.3: CT slice of a patient with a tumour in the right kidney. (left) contrast enhanced CT slice and (right) CT slice showing segmentation masks of kidney parenchyma (green), tumour (purple) and arteries (red).

The quality of the results of the final perfusion model is highly dependent on the quality of the segmentation. For instance, when a major vessel is missed or a non-existing vessel is added, wrong conclusions can be drawn and this can lead to inadequate clamping. Though, segmentation of raw CT data is a challenging and time-consuming task. The resolution of CT images is often limited and image acquisition with contrast agents is not always accurate. Therefore, it requires sufficient anatomical knowledge and exercise to speed up the process and overcome difficulties in distinguishing different structures. Instead of performing manual segmentation, a master student thesis in Biomedical Engineering, Jordi Martens, is working on automatic segmentation in the context of this project. That would allow to speed up the segmentation step and enables automation of the complete workflow starting from clinical data to the actual perfusion model, which is the final objective of the planning tool.

3.1.2 Skeletonization

The 3D model of the arterial tree delivers the necessary information about the anatomy of the arterial tree for the input of the model. In the next step, the 3D model of the arterial tree is skeletonized as depicted in figure 3.4 to allow qualitative assessment.

Several people have been active in the development and optimisation of algorithms to calculate the skeleton from segmented data, as briefly discussed in section 2.5.2. They used a thinning algorithm to obtain the skeleton of vascular structures. However, in the context of this thesis, an alternative approach is used that makes use of Mimics. The Mimics software allows to calculate centrelines based on the 3D reconstructions as depicted in figure 3.4. The generated centrelines are first inspected and manually adjusted when needed by removing wrongly skeletonized branches or adding segments. Then, they are grouped according to their generation. Thereafter, their coordinates are exported to a text file to serve as an input for the model.

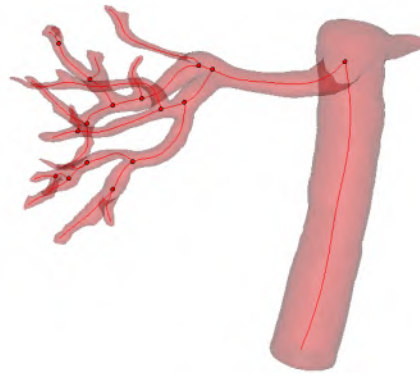


Figure 3.4: Centrelines calculated in Mimics from the 3D model of the arterial tree

The exported data contains for each branch the corresponding branch number and the coordinates of the control points on the branch. These control points are automatically generated and their number depends on the tortuosity and length of the branch. In figure 3.5, the obtained centrelines are depicted with their corresponding branch numbers.

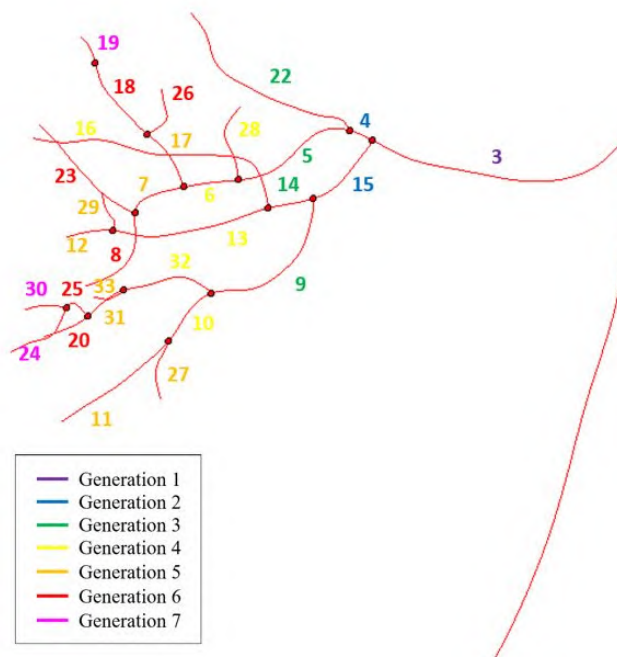


Figure 3.5: Centrelines with corresponding branch numbers. The colours of the numbers designate the corresponding generations following a top-down ordering.

The major advantage of this approach to calculate centrelines is that the centrelines are obtained directly from the segmented 3D model in Mimics and thus requires no additional algorithm. Though, this approach is only partly automatic resulting in additional manual steps.

3.2 Perfusion model

The image volume is composed of discrete blocks or voxels. The base of these blocks is typically squared with a side of 1 mm and the height is equal to the slice thickness. Based on the segmentations, voxels are assigned to the kidney or tumour. For each of these voxels of the kidney, the model determines the number of the branch that has the highest probability of supplying that voxel. It is important that the allocation of a branch number to each voxel is anatomically relevant and at the same time is feasible without requirements of excessive computational power. A logic approach that comes up in mind is a method that determines the nearest branch to each voxel. As discussed in section 2.6.2, a similar approach of shortest distances was applied and validated by [46] and showed to have good results proving it to be anatomically relevant without excessive computational demands. Though the method was only applied for the liver, a similar approach for the kidneys should give realistic results too and therefore looks suitable as a base for the model.

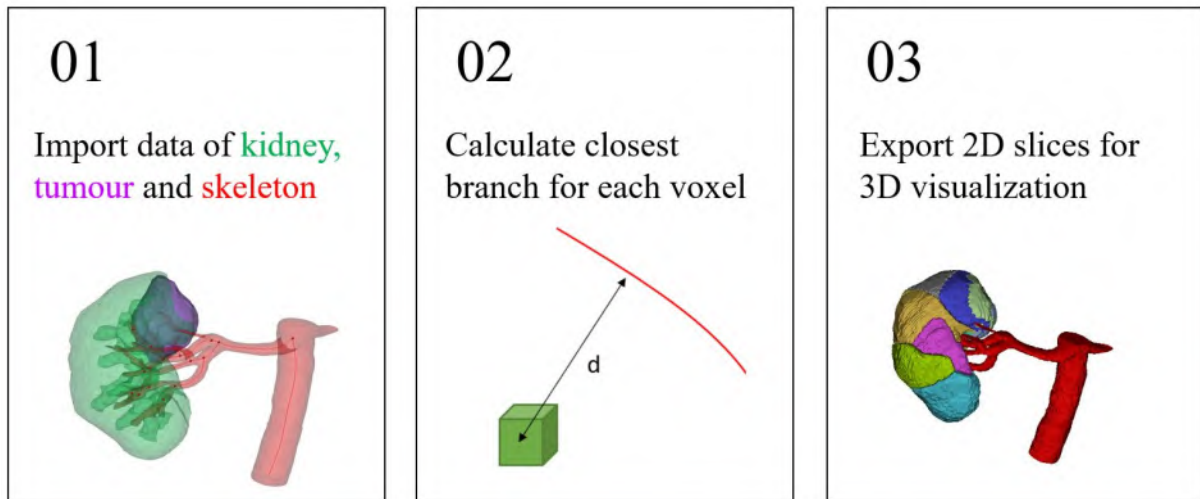


Figure 3.6: The model starts with (1) loading the data of the skeleton, the tumour and the kidney. Next (2), the data is used by the model to determine the perfusion areas of the arterial tree. At last (3), these results are exported as 2D slices and converted into 3D images.

The model itself is written in Python code and is built up following three steps as depicted in figure 3.6. First, the data of the skeleton, kidney and tumour is loaded. From this information, the model determines the perfusion zones by determining the closest branch to each voxel. Therefore, two different approaches are used, which will be explained later on. Once each voxel is assigned to a specific branch, the obtained perfusion zones are exported to 2D sliced images that are imported in Mimics to allow 3D visualization.

3.2.1 Load input data

The first part of the model exists of importing the data as depicted in table 3.1.

Import data	file type	obtained info
Skeleton	.txt	x, y, z coordinates control points Branch number
Tumour	.bmp 2D slices	x, y, z coordinates of voxels
Parenchyma	.bmp 2D slices	x, y, z coordinates of voxels

Table 3.1: Overview of the import data that is loaded in the model.

Skeleton

The skeleton is loaded in the model as a text file that lists the control points for each branch of the skeletonized arterial tree as depicted in figure 3.7. From this file, the information about the positions of these control points and the corresponding branch numbers are retrieved. The positions of these control points are described in a coordinate system of Mimics, that varies with each dataset. To allow calculations, a coordinate transformation is applied to describe all the control points in the same coordinate system as the tissue.

[Generation 1] Branch Segment 3:						
Point (17.6797, -131.9220, 1489.4725) connects from:						
Branch Segment 1						
Point (-24.4158, -125.0657, 1485.1500) connects to:						
Branch Segment 15						
Branch Segment 4						
Px	Py	Pz	Tx	Ty	Tz	
17.6797	-131.9220	1489.4725	-0.5133	-0.8498	0.1198	
16.6110	-133.2391	1489.8623	-0.6752	-0.6781	0.2902	
16.0322	-133.8016	1490.1131	-0.6888	-0.6622	0.2952	

Figure 3.7: Example of the data in the text file where the branch number (green box) and the x, y and z coordinates of each control point (red box) can be obtained. The other specifications in the file, such as the minimal radius are now not used, though may be interesting for future applications.

The coordinate transformation converts the X_{mc} , Y_{mc} and Z_{mc} coordinates of each control point (designated with red box) to new coordinates X_v , Y_v and Z_v , that are calculated as depicted in equations 3.1, 3.2 and 3.3. Here, X_{min} , Y_{min} are the x and y coordinates corresponding with respectively the left and top side of an image slice in Mimics. Z_{min} is the coordinate of the bottom slice of the image. ΔX_{mc} and ΔY_{mc} give the width and height of the image slices in Mimics and ΔX_v , ΔY_v represent the dimensions of the BMP slices. The ΔZ_{mc} and ΔZ_v have typically the same value and can be calculated as the number of slices multiplied with the slice gap. Figure 3.8 visualises the meaning of these coordinate values for the two coordinate systems. Importantly, these values vary between different patient cases and hence the coordinate transformation should be adapted to each patient.

$$X_v = \frac{X_{mc} - X_{min} \cdot \Delta X_v}{\Delta X_{mc}} \quad [mm] \quad (3.1)$$

$$Y_v = \frac{Y_{mc} - Y_{min} \cdot \Delta Y_v}{\Delta Y_{mc}} \quad [mm] \quad (3.2)$$

$$Z_v = \frac{Z_{mc} - Z_{min} \cdot \Delta Z_v}{\Delta Z_{mc}} \quad [mm] \quad (3.3)$$

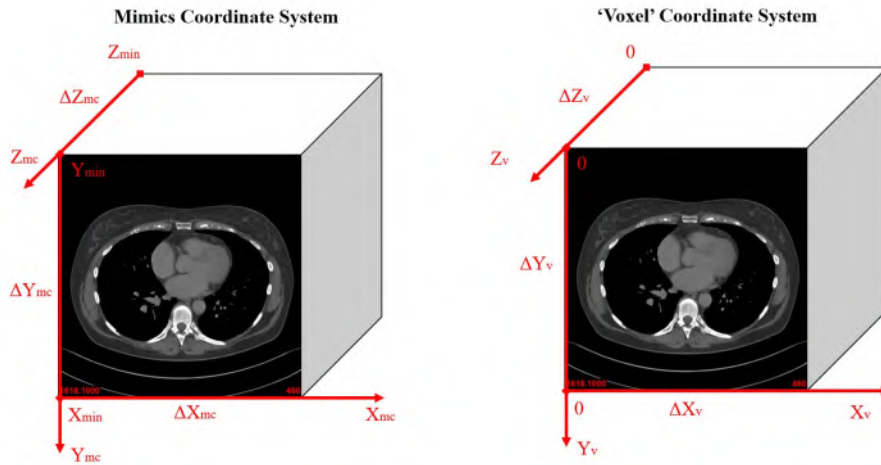


Figure 3.8: The X_{mc} , Y_{mc} and Z_{mc} coordinates in Mimics coordinate system (left) are transformed into new coordinates X_v , Y_v and Z_v in 'voxel' coordinate system (right), according to the transformation depicted by equations 3.1, 3.2 and 3.3

Finally, four lists are obtained containing the x, y and z coordinates and the branch numbers of the complete arterial tree. Though in reality, only branches that go into the kidney will supply the tissue. Moreover, the surgeon can only clamp a specific branch of the arterial tree, when this branch is located outside the kidney. Therefore, branches are only marked if they fulfil all requirements as listed below.

- Requirement 1: the branch should start outside the tissue (tumour or kidney) .
- Requirement 2: a part of the branch should go inside the tissue or the branch should have a dead-end.

In short, only branches that start outside the kidney or tumour and go inside the tissue or have a dead-end are selected to determine the perfusion zones. These branches often ramify further in the kidney. These daughter segments obtain the branch number of their corresponding selected parent branch and hence their control points are also used in the calculations later on. For instance when branch 4 is marked and further ramifies into 5 and 6, then the control points of 5 and 6 are assigned to branch 4. This principle of selecting branches is depicted in figure 3.9 Finally, all branches that fulfil the requirements and their ramifications are kept, while the others are removed from the lists.

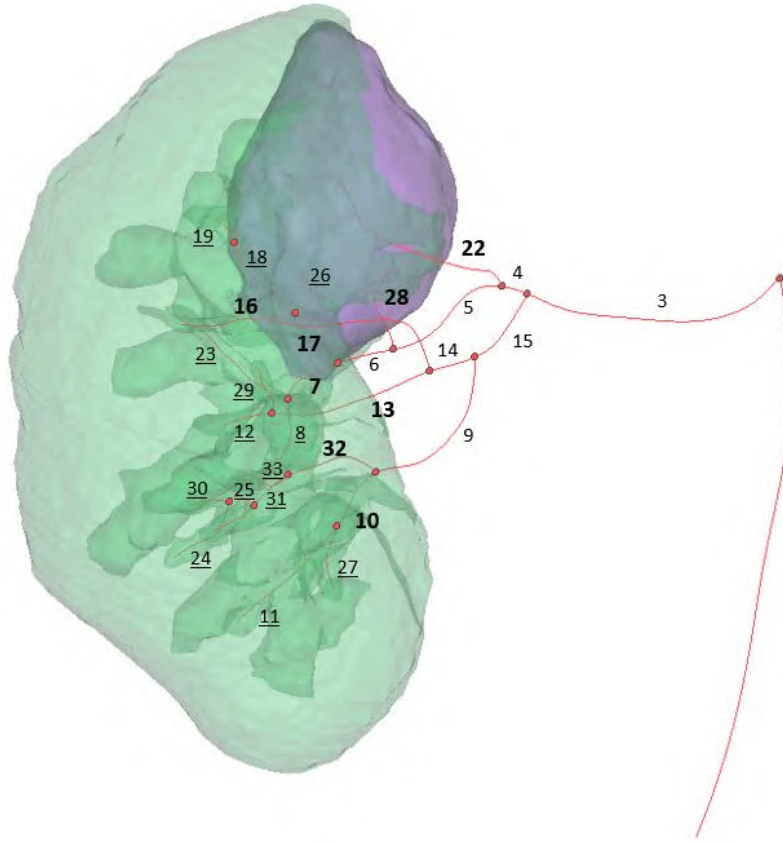


Figure 3.9: The tumour and the tissue are supplied by different branches of the arterial tree. The arterial tree is skeletonized and the branch numbers are added. The bold numbers depict the branches that fulfil the two requirements as set in this section and therefore are selected as the branches determining the perfusion zones. The underscored numbers mark the segments that are situated inside the kidney and are ramifications of the selected (bold) branches.

Kidney and tumour tissue

The perfusion zones need to be calculated inside the kidney and tumour. Therefore, the 2D axial slices of the kidney and tumour are loaded as depicted in figure 3.10 and their coordinates are listed in separate lists for the tumour and the tissue. The x , y and z coordinates are defined according to the dimensions of the image matrix. To give a simple example, a typical slice is 0.7 mm separated the neighbouring slices and has dimensions of 512 mm x 512 mm. So, a voxel situated at the 3rd slice in the second column, has $x = 1mm$ and $z = 1.4mm$. The coordinate system defined in this way is used for further calculations and therefore the skeleton coordinates are also converted to this coordinate system.

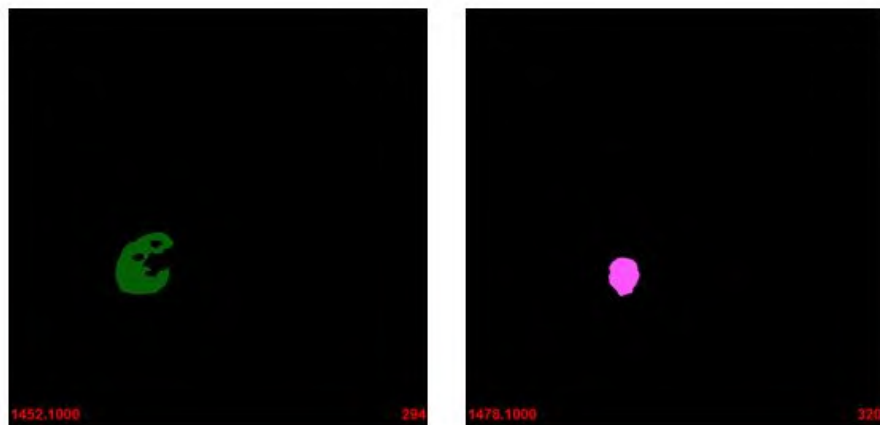


Figure 3.10: Examples of axial 2D slices of the kidney (left) and tumour (right).

Only part of the image volume contains information about the tissue and the tumour. Many top and bottom slices are empty and therefore these slices are not included in the input data. Hence before the data is loaded in the model, the z-coordinate of the new start slice is determined to assign correct z-coordinates. The main reason for removing these slices is the reduction of computational time. This action does not influence the final results and therefore is only advised to decrease the running time of the model.

3.2.2 Apply the model

Once the information about the skeleton and the kidney with the tumour is loaded and listed, the algorithm can be applied. As mentioned before, two different approaches are used to determine the perfusion zones. The first approach simply determines for each voxel of the kidney and tumour the point of the skeleton that is the closest to that voxel and is later on mentioned as the direct distance method. The other method uses the principle of region growing and grows the different branches of the skeleton simultaneously within the volume of the kidney and tumour.

Direct Distance Method

The direct distance method determines the closest branch to each voxel of the kidney and tumour by calculating distances between voxels and control points. The positions of the control points with their corresponding labels and the voxel coordinates are listed as discussed in section 3.2.1. For each of the voxels, the distances to all control points of the arterial tree are calculated. Equation 3.5 shows the calculation of the squared distances between a voxel of the kidney i and a control point of the skeleton j .

$$\mathbf{d}^2(i, j) = [X_{kidney}(i) - X_v(j)]^2 + [Y_{kidney}(i) - Y_v(j)]^2 \quad (3.4)$$

$$+ [Z_{kidney}(i) - Z_v(j)]^2 \quad (3.5)$$

Next, for each voxel i the control point l is determined that corresponds with the minimum distance d from the voxel to the control point as depicted in equation 3.6.

$$\mathbf{d}^2(i, l) = \min\{\mathbf{d}^2(i, 1), \mathbf{d}^2(i, 2), \dots, \mathbf{d}^2(i, n)\} \quad (3.6)$$

$$(3.7)$$

Finally, the number b of the branch where the control point l is located on, is assigned to voxel i . This is practically done by setting function S_{kidney} for this voxel i equal to the number b as depicted in equation 3.8.

$$S_{kidney}(i) = b(l) \quad (3.8)$$

The same method as discussed for the kidney is applied to the list of voxels of the tumour. And that results in a function S_{tumour} that gives for each voxel i the number b of the branch containing the control point that is at a minimum distance from this voxel.

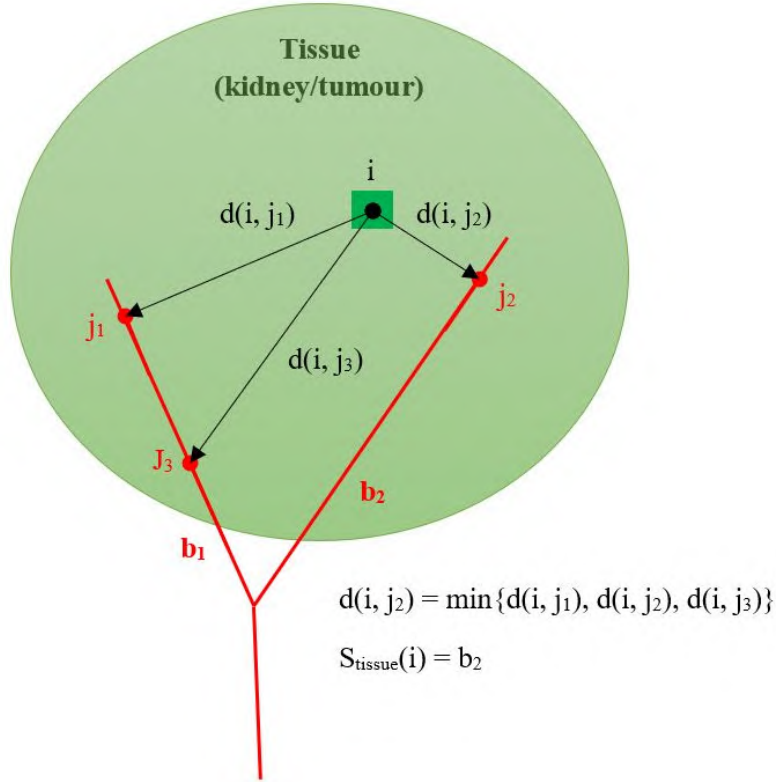


Figure 3.11: Simple example of the principle of the direct distance approach explained above.

Based on the coordinates of the voxels, the obtained labels are positioned within the 3D image volume and this results in a 3D map of the perfusion zones of each branch. Figure 3.12 shows two resulting slices of the direct distance method. As depicted in equation 3.9, the x and y dimensions of the volume remain equal to the original image dimensions in the 'voxel' coordinate system, namely ΔX_v and ΔY_v respectively, and the z range is equal to the number of slices or $\#slices$.

$$image\ shape = (\Delta Y_v, \Delta X_v, \#slices) \quad (3.9)$$

The major drawback of the direct distance method is that the calculations take some time, which is a result of a large number of equations to be solved, namely number of voxels multiplied with the number of control points. Usually, the computational time exceeds 15 minutes.

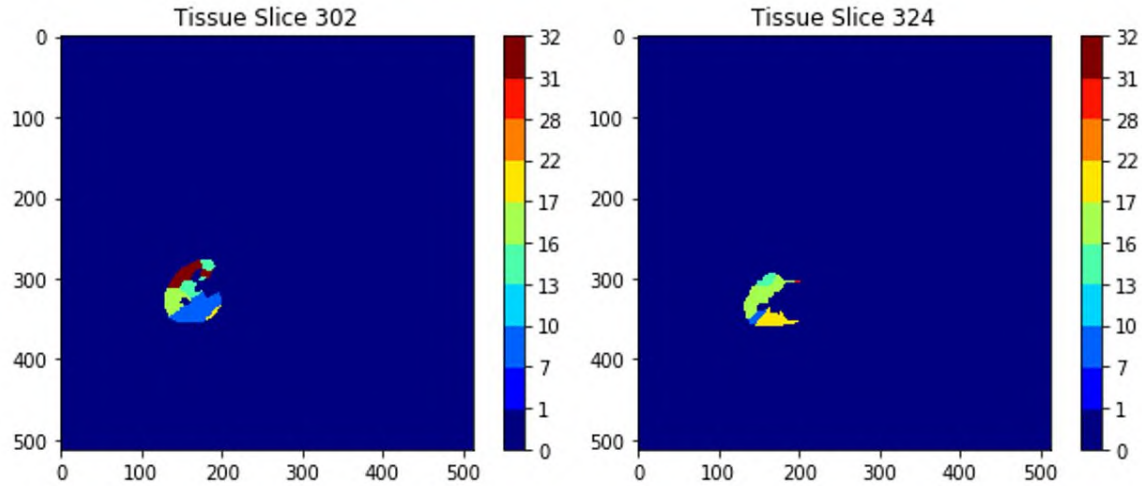


Figure 3.12: Two slices obtained from the direct distance method.

Region Growing Method

The second method aims to define the same perfusion zones as the direct distance method, but by using the approach of 'growing' the arterial branches. In principle, each skeletonized branch grows with the same speed in all 6 directions (back and forth in x,y and z direction). Each branch keeps growing until it reaches the end of the tissue or until it meets another branch. Then the region stops growing. The practical implementation in Python is more complex than the direct distance approach, though the computational time is slightly shorter due to a lower number of calculations.

In order to explain the method in a simple way, the region growing method is applied to a simple example of a 2D slice. Hence, region growing will only occur in 4 directions where the actual model will include all 6 directions, though the general principle is similar as in 3D region growing. The example slice exists of 5 rows and 5 columns and three starting points are marked with three different labels as depicted in figure 3.13(a). Each point $b(x, y)$, that is defined by its position in x and y and labelled with the assigned branch number b , is added to the region growing list (RG list). Hence, the RG list initially only includes these points as depicted in equation 3.10.

$$RG = \left\{ 1(0, 0) \quad 2(3, 2) \quad 3(1, 4) \right\} \quad (3.10)$$

Next, the first element of the list $1(0,0)$ is selected with coordinates $X_1 = 0$ and $Y_1 = 0$. For this element the 4 surrounding elements are determined as depicted in equation 3.11.

$$\begin{cases} (X_1 - 1, Y_1) & \text{Point 1: left} \\ (X_1 + 1, Y_1) & \text{Point 2: right} \\ (X_1, Y_1 - 1) & \text{Point 3: up} \\ (X_1, Y_1 + 1) & \text{Point 4: down} \end{cases} \quad (3.11)$$

Each of these points is only added to the end of the RG list if (1) the point is part of the image volume and (2) no label is assigned to this point. For element 1(0,0), point 3 and point 2 meet these conditions. Hence, label 1 is assigned to these points and they are added to the region growing list as depicted in equation 3.12. The resulting image after this first step is shown in figure 3.13(b).

$$RG = \left\{ 1(0,0) \quad 2(3,2) \quad 3(1,4) \quad 1(1,0) \quad 1(0,1) \right\} \quad (3.12)$$

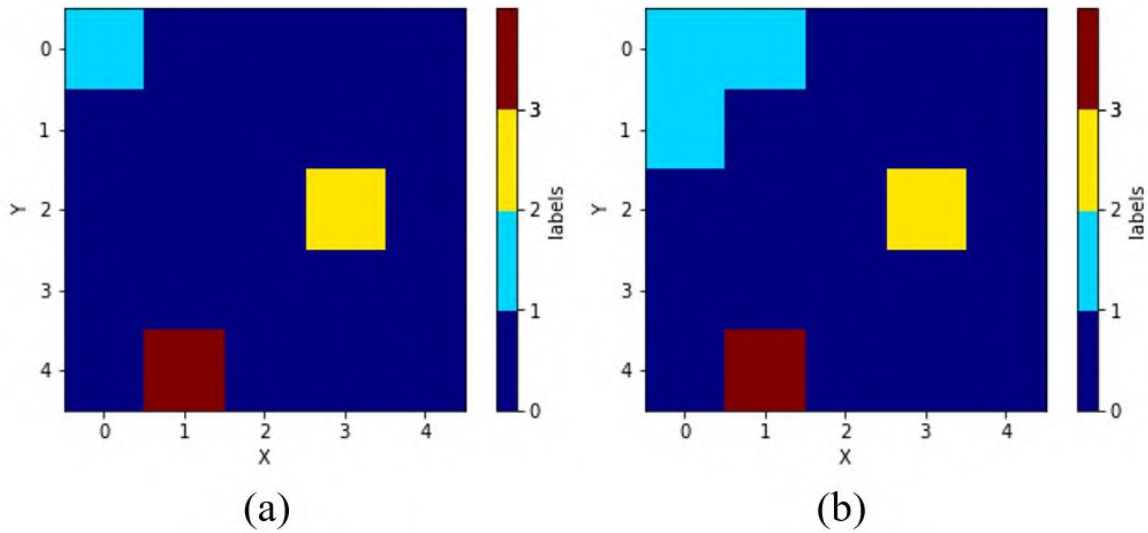


Figure 3.13: The initial situation (a): three points are labelled with 1(blue),2 (yellow) and 3(brown) and (b) the result after one step of region growing.

Next, the second element of the RG list is selected and again the surrounding points are determined and added when they meet the conditions. In that way, for each point in the array, the surrounding voxels are determined. If they meet the conditions, they are added to the region of the original point, resulting in gradually growing of the different regions. Figure 3.14 shows how the region growing algorithm gradually results in three regions with three different labels.

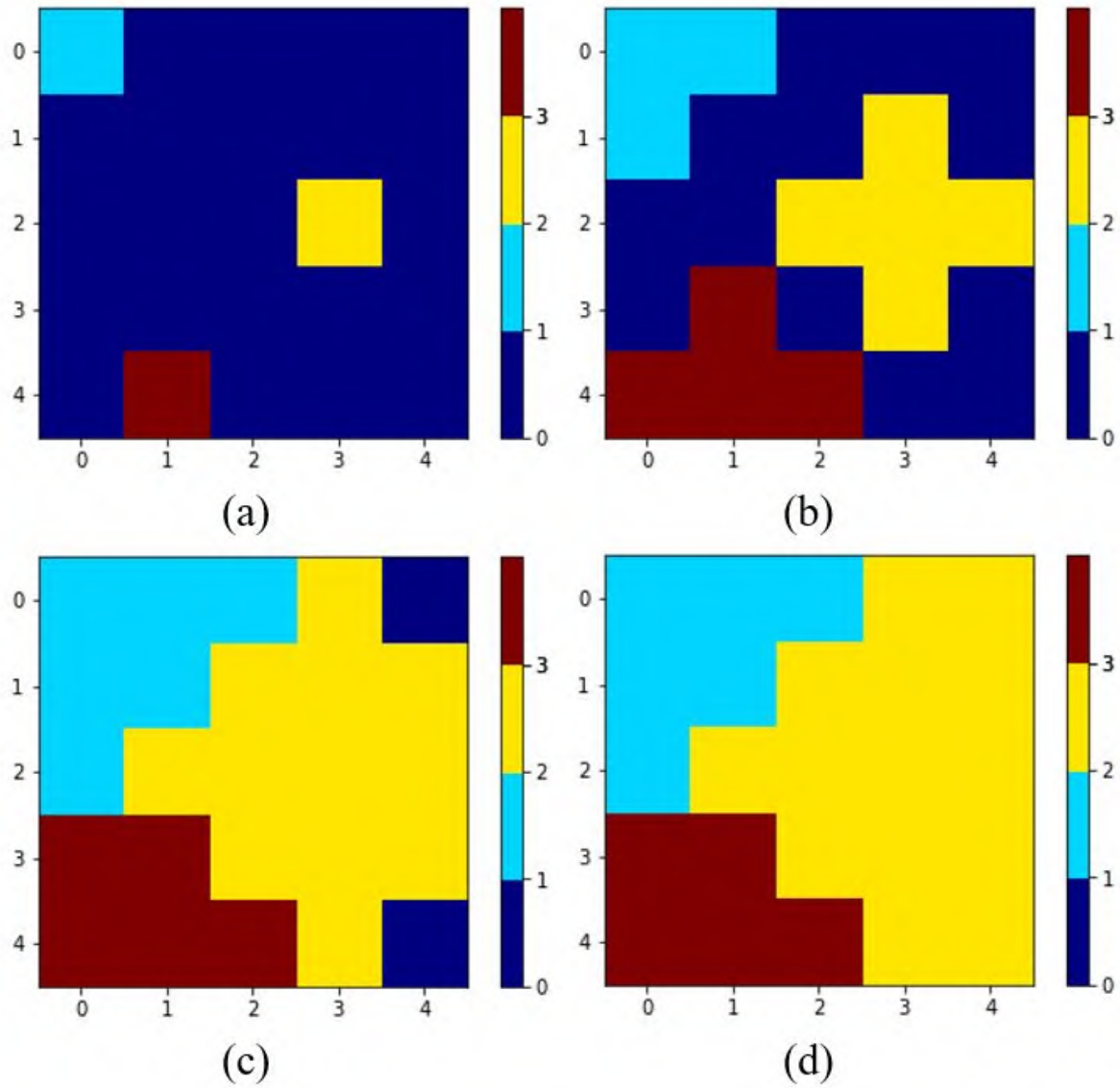


Figure 3.14: (a) The initial situation with three differently labelled points. (b) the situation after one step of region growing of each region. (c) shows further progression in region growing and (d) shows the final result of three different regions labelled with 1, 2 and 3 or blue, yellow and brown.

The region growing method has been applied in a similar way on the arterial tree, with the control points of the arterial tree serving as starting points. The matrix where the arteries grow into the regions, is defined within a 3D image matrix with dimensions as described below.

- The x and y range are equal to the ΔX_v and ΔY_v respectively as defined in section 3.2.1, which are the width and heights of the image slices in the 'voxel' coordinate system.
- The Z range is equal to the number of slices multiplied with the slice gap.

Hence, the 3D image volume exists of squared voxels, allowing growing with equal speed in all directions. Similar as in the example, all control points are added to the RG list as symbolically depicted in equation 3.13. These control points have a label corresponding to the branch they are located on.

$$RG = \left\{ \dots \quad b_j(X_i, Y_i, Z_i) \quad b_j(X_{i+1}, Y_{i+1}, Z_{i+1}) \quad \dots \quad b_{j+1}(X_{i+2}, Y_{i+2}, Z_{i+2}) \quad \dots \right\} \quad (3.13)$$

For each point $b(X, Y, Z)$ of the RG list, the neighbouring points are determined as depicted in equation 3.14. These points are marked in the 3D matrix and added to the list if they have no label yet and are located inside the image volume.

$$\left\{ \begin{array}{ll} (X - 1, Y, Z) & \text{Point 1: left} \\ (X + 1, Y, Z) & \text{Point 2: right} \\ (X, Y - 1, Z) & \text{Point 3: posterior} \\ (X, Y + 1, Z) & \text{Point 4: anterior} \\ (X, Y, Z - 1) & \text{Point 5: bottom} \\ (X, Y, Z + 1) & \text{Point 6: top} \end{array} \right. \quad (3.14)$$

The result of the 3D region growing is depicted in figure 3.15, showing that the regions have grown over the whole image. From these images, the parts of the kidney and tumour cannot yet be distinguished from the rest of the image. Therefore, the image volume of the kidney and tumour are defined. Hence, two 3D image volumes are created with the same dimensions as the region growing matrix. The new image volume exists of cubic voxels with edge 1 mm. However, the original slices with the information of the tissue volumes exist of voxels with cuboid shape due to a slice gap different from 1mm. Hence, empty voxels between slices need to be filled when creating these new image volumes. Therefore, all the voxels that have a filled voxel on top are also filled to compensate for slices that were not present in the original image volume.

In the region growing image volume, only the zones that are part of the kidney tissue volume or the tumour volume are stored, resulting in a map of the perfusion zones for the kidney and the tumour. Figure 3.16 depicts two resulting slices containing the tumour (right) and the kidney (left). The major advantage of this approach is that also slices located outside the kidney or tumour can be taken into account. This is important since these branches may have bifurcations inside the kidney that are not visualized in the segmented model of the arterial tree.

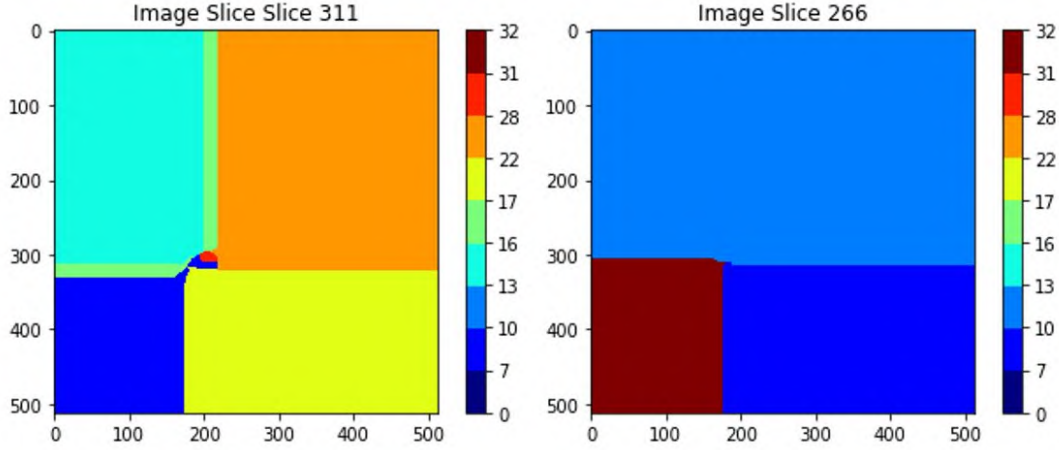


Figure 3.15: Two image slices as results of the region growing.

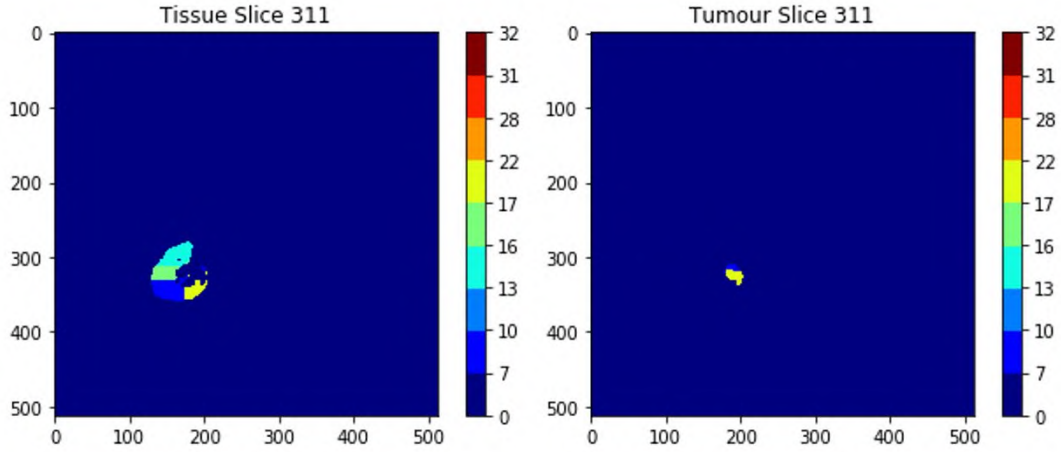


Figure 3.16: Image slice of the kidney (left) and the tumour (right) divided into perfusion zones as a result of the region growing method.

3.2.3 Output 2D slices

The direct distance and region growing method result both in 3D image volumes of the kidney and tumour divided into perfusion zones. In the final 3D model, the arterial tree and the perfusion maps of kidney and tumour are visualised together. Therefore, superposition of the three image volumes is applied. For the superposition of the region growing images, the volume of the arterial tree is first re-sampled from rectangle to cubic voxels to have the same built-up as the tumour and kidney volumes. The re-sampling of the volumes was required to have the same speed of region growing in all directions. To be able to distinguish the tumour volume from the kidney volume, the labels of the kidney volume are changed from their original labels b_{tumour} to their new labels $b_{tumour,new}$ as depicted in equation 3.15. BL presents the list containing the different branch numbers.

$$b_{tumour,new} = b_{tumour} + \max(BL) \quad (3.15)$$

The major advantage of this approach is that the original labels can easily be derived later on, while the tumour and kidney volumes still can be separated.

The final image after superposition is a volume containing information about the arterial tree and the perfusion zones of the kidney and tumour. This image volume is again decomposed into slices with a thickness of one voxel in the z-direction. It is important to note that the direct distance method will deliver slices with the same slice thickness as the original slices, while the slices obtained from the region growing method are re-sampled to slices with a thickness of 1 mm. These slices are exported as grey value images in BMP format.

3.3 Visualization and validation

The 2D slices are converted into a 3D model of the perfusion zones using the Mimics software. In chapter 4, the results of the model applied to four patients are discussed in detail.

These 3D models are first inspected visually to detect major mistakes by looking whether the position of the perfusion zones is realistic compared to the location of the supplying arteries. Next, a first validation of our outcomes is done based on the results of Visible Patient, which is possible because the raw CT data of two patients were sent for analysis to its online service and used for our model as well after segmentation by the medicine students. Visible Patient provided 3D reconstructions of the kidneys and their arterial tree as well as a clipping model showing the perfusion zones per arterial segment. Their results were used for surgical planning to decide on the clipping locations. Though these models are not yet clinically validated, their predictions proved to be realistic during surgery and thus can be used for validation of our model.

Chapter 4

Results and discussion

The perfusion model is applied to four patient cases. Each of them was diagnosed with kidney cancer. As part of the standard care protocol prior to the partial nephrectomy surgery, contrast-enhanced CT scans of the abdomen were taken. Figure 4.1 shows the 3D models of the affected kidney for each of these patients obtained after segmentation of the raw CT images.

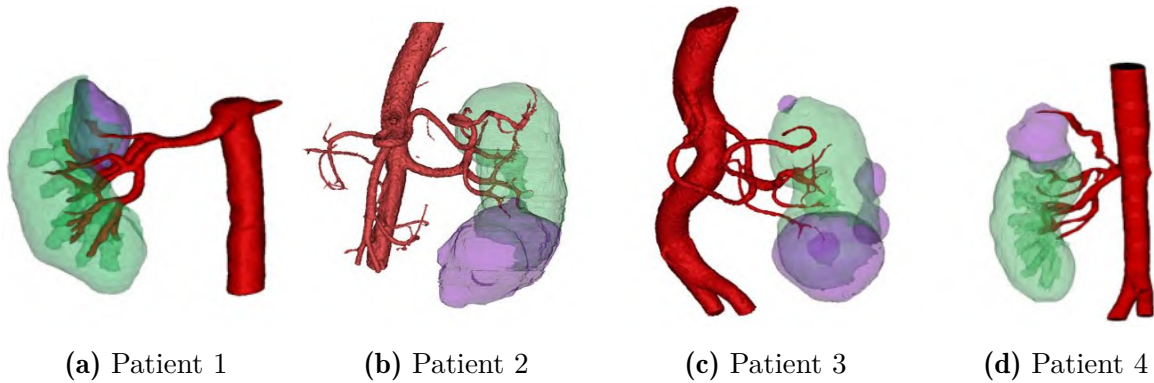


Figure 4.1: Anterior view on 3D models of the renal parenchyma (green), tumour (purple) and arteries (red) as result of segmentation

The underlying algorithm of the model uses either the direct distance or region growing approach as discussed in the materials and methods chapter 3. In the next sections, the results of these methods for each patient are shown and discussed. Further, a first validation of the results is done based on the results of the online service Visible Patient for two patient cases.

4.1 Input of the patient cases

Before addressing the results, the input data and skeletonization is shortly discussed for each patient. The quality of the input data deserves prior attention since it strongly influences the quality of the outcomes of the model. Inspection of the CT images of the different patient cases shows that the image specifications such as slice thickness differ between the patients as a result of different parameters during image acquisition. The acquisition of CT images is executed according to predefined protocols to control the dose and image quality. The slice thickness correlates with these protocols since an increased slice thickness requires a lower radiation dose [43]. Table 4.1 gives the specifications of the original image volume. As discussed in section 3.2.1, only part of the image volume is loaded to limit computational effort. Therefore, the table also defines the number of slices that is actually loaded, and the z-coordinate of the start slice, which is the first slice that is loaded.

Patient	shape image volume [m^3]	number of slices	Slice gap [mm]	start slice	Loaded slices
1	512x512x460	231	2	252	53
2	512x512x467.6	669	0.7	231	281
3	512x512x374.5	536	0.7	210	161
4	512x512x506.4	424	1.2	276	142

Table 4.1: Overview of image specifications for each dataset containing the complete shape of the image volume, the original and loaded number of slices, the slice thickness or slice gap and the z-coordinate of the first slice that is loaded.

The arterial tree of each 3D model is skeletonized as depicted in figure 4.2. The arterial model of the first patient has the most detailed tree with extensive branching up to the 7th generation and well-segmented branches. That allows to generate a relatively detailed skeleton. The arterial models of the other patients are less detailed showing less extensive branching and more incomplete branches in the tree. Often, these incomplete branches or branches with very small cross-sections are not skeletonized automatically, and hence need to be added manually to the skeleton. The detail in the arterial model directly affects the quality of the perfusion model, since a more precise model approximates better the real arterial tree. Hence, models of the arterial tree with low precision miss valuable information to determine the perfusion by missing for instance branches that go to the tumour.

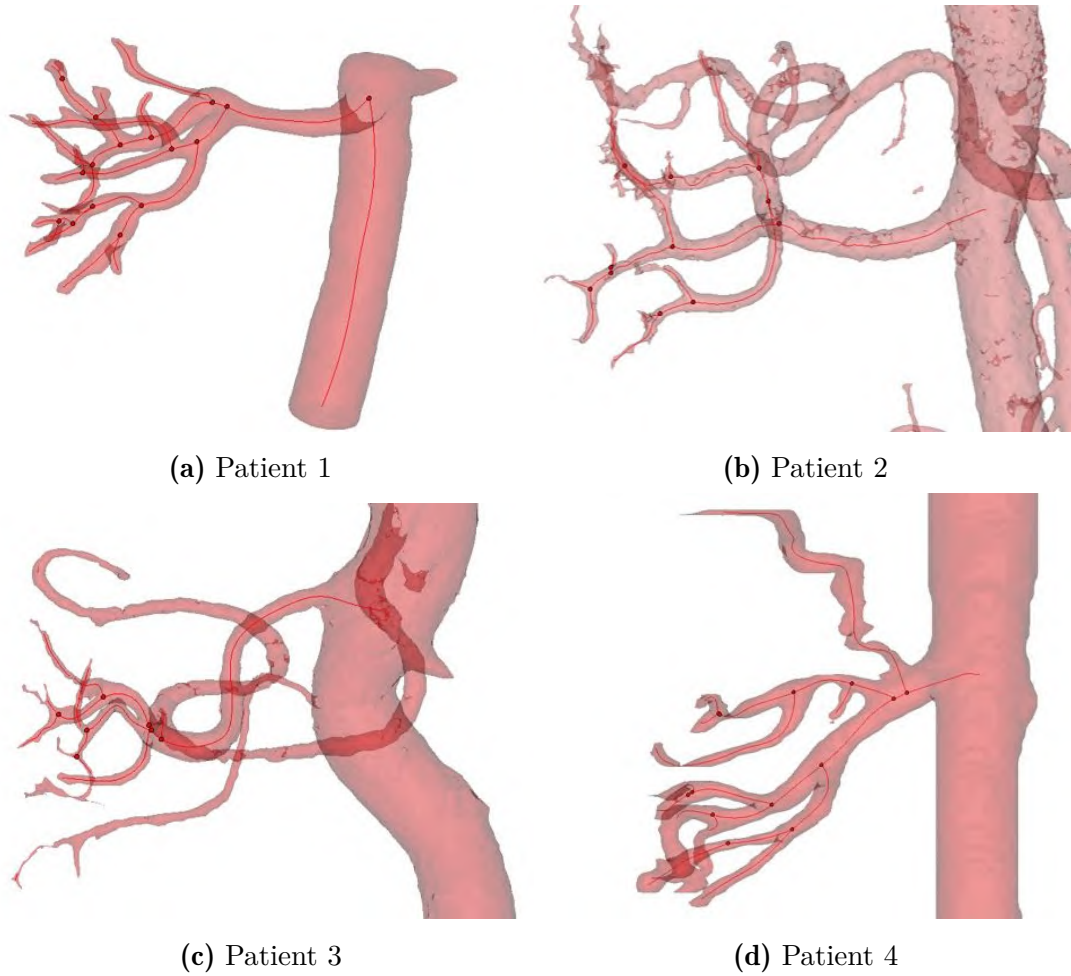


Figure 4.2: The 3D model of the arterial tree and the calculated centrelines for each patient case in anterior view for patient 1 and 4 and posterior view for patient 2 and 3. The complexity of the reconstruction of the tree of patient 3 has more detail than the trees of the other patients.

With the generation of the skeleton, branches are numbered automatically. As discussed in section 3.2.1, branches that start outside the kidney and tumour and subsequently enter it (or have a dead end) are selected to determine the perfusion zones as depicted for all patients in figure 4.3. The bifurcations from these branches are grouped under their corresponding selected branches and are also considered in the calculations.

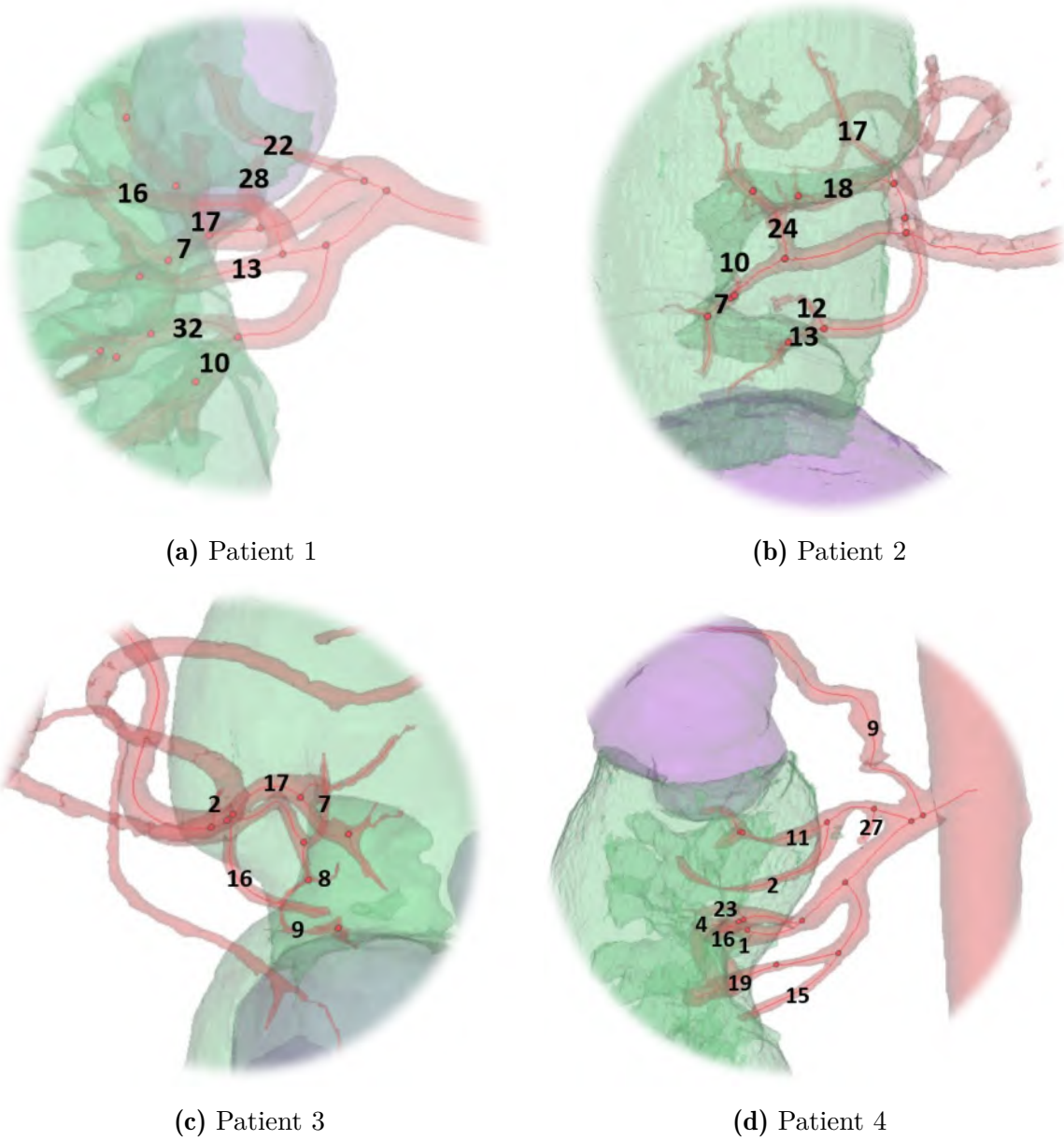


Figure 4.3: The tumour and the tissue are supplied by different branches of the arterial tree. The bold numbers depict the numbers of the branches that fulfil the requirements as set in section 3.2.1 and therefore, are selected as the branches determining the perfusion zones.

4.2 Results of direct distance method

The results in this section are obtained using the direct distance method as described in section 3.2.2. The results are represented as 3D perfusion maps of the healthy parenchyma and the tumour. Figure 4.4 depicts the division into these zones for the first two patients and figure 4.5 shows the maps for patient 3 and 4. Each region represents a zone that is supplied by a specific segment of the arterial tree. These branches are selected from the arterial tree as discussed in the previous section and their positions and corresponding branch numbers are depicted in figure 4.3 for every patient. At the right side of the figures below, the number of these branch segments are given for each region.

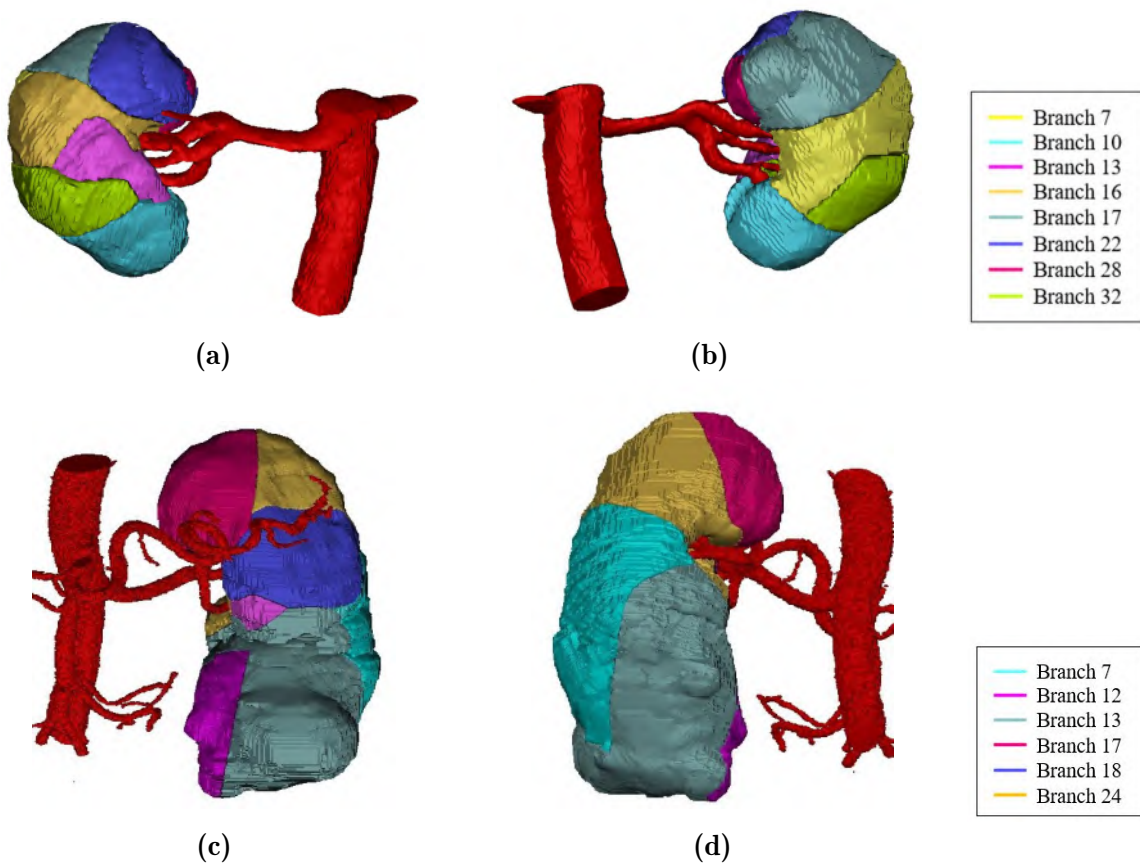


Figure 4.4: Anterior and posterior view on the perfusion maps with the arterial tree of patient 1 (a-b) and 2 (c-d). Each color represents a perfusion zone supplying the corresponding arterial branch.

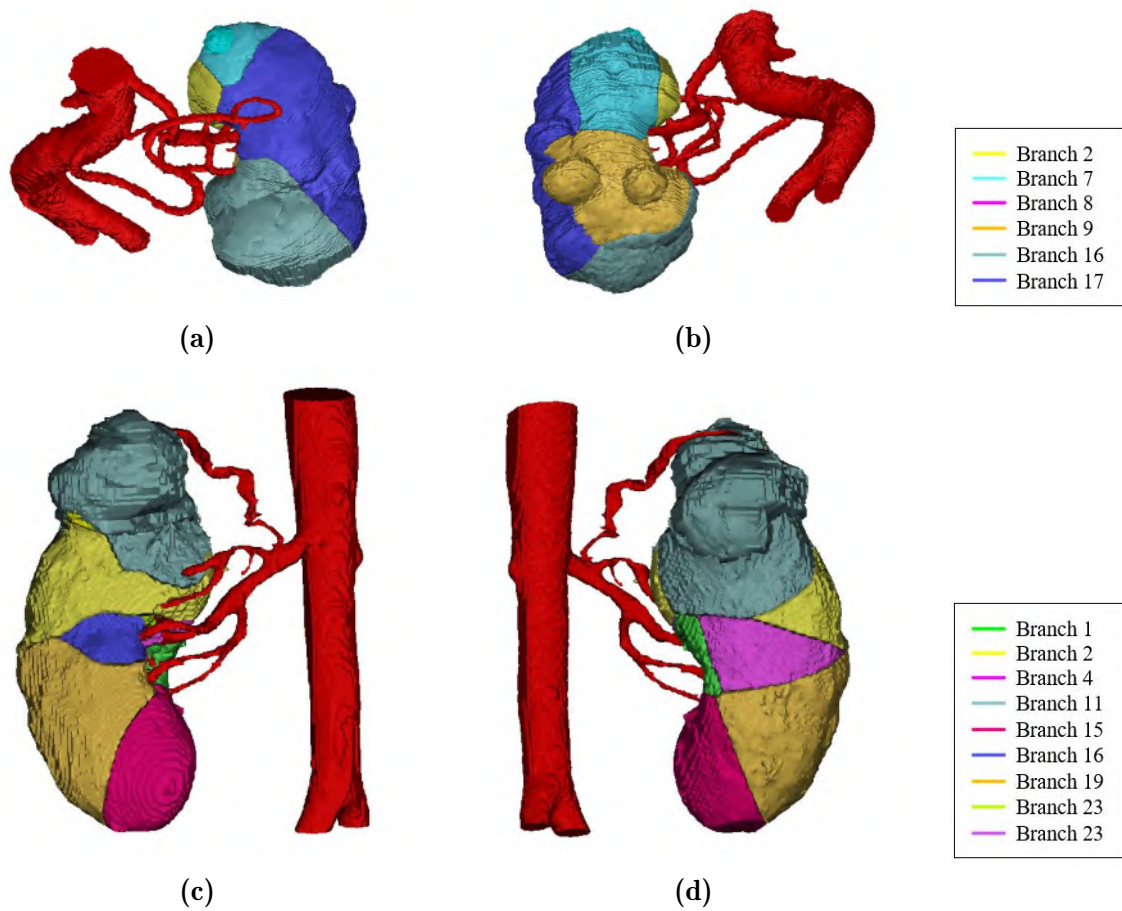


Figure 4.5: Anterior and posterior view on the perfusion maps with the arterial tree of patient 3 (a-b) and 4 (c-d). Each color represents a perfusion zone supplying the corresponding arterial branch.

The planning tool aims to distinguish the arteries that go to the tumour from those that only supply healthy tissue. Therefore, a closer look is taken at the tumour. In figure 4.6(a) the tumour of patient 1 is depicted. The model predicts that the tumour is supplied by five different branches since their perfusion zones include the tumour. This suggests that the surgeon should clamp these vessels to avoid bleeding during surgery. Though, figure 4.6(b) shows that these branches also supply a significant part of the healthy parenchyma. Thus, selective clamping of these vessels will cause local ischemia in half the kidney, though the other parts of the healthy parenchyma will be spared, which seems like a better option than complete kidney ischemia or excessive bleeding without clamping. This, of course, only holds if the predictions by the model are correct.

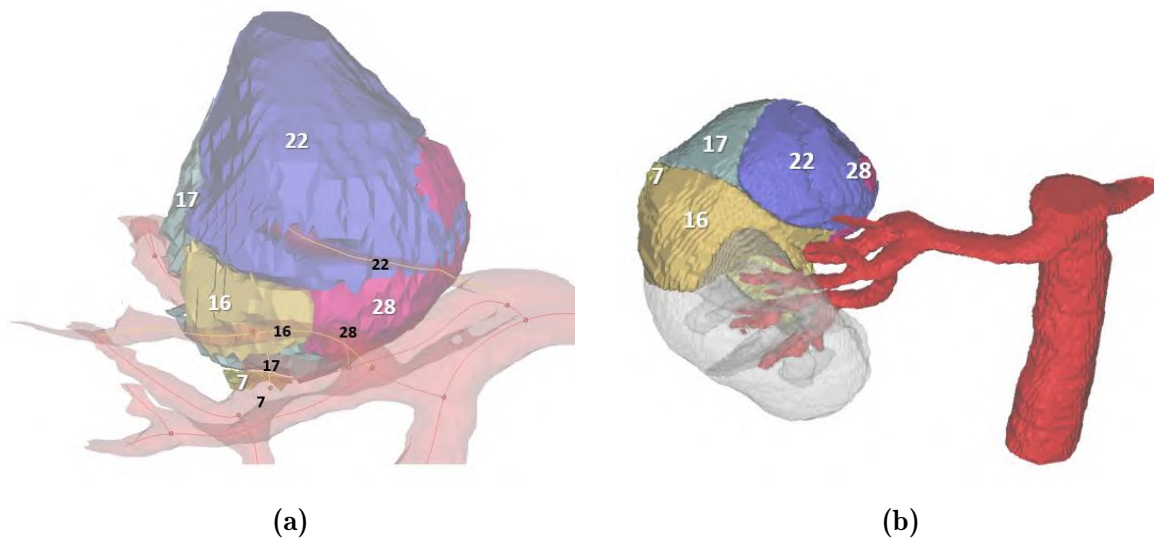


Figure 4.6: (a) The detail of the tumour of patient 1 shows 5 perfusion zones in the tumour, supplied by branches 7, 16, 17, 22 and 28. (b) The perfusion map of these branches in the complete kidney shows that they perfuse about half the kidney including a substantial part of the healthy parenchyma.

Figure 4.7(a) zooms in on the tumour of patient 2. Here, the model predicts that there will be 3 perfusion zones supplied by arterial segments 7, 12 and 13. Figure 4.7(b) shows that the perfusion regions of the branches outside the tumour are limited. Thus, clamping these vessels should allow bloodless resection with limited healthy tissue ischemia. However, the complexity of this arterial tree is low compared to what is expected from the real anatomy and that may influence the quality of the predictions by the model. It is clear that validation of the outcomes is necessary to see how well the results approximate reality.

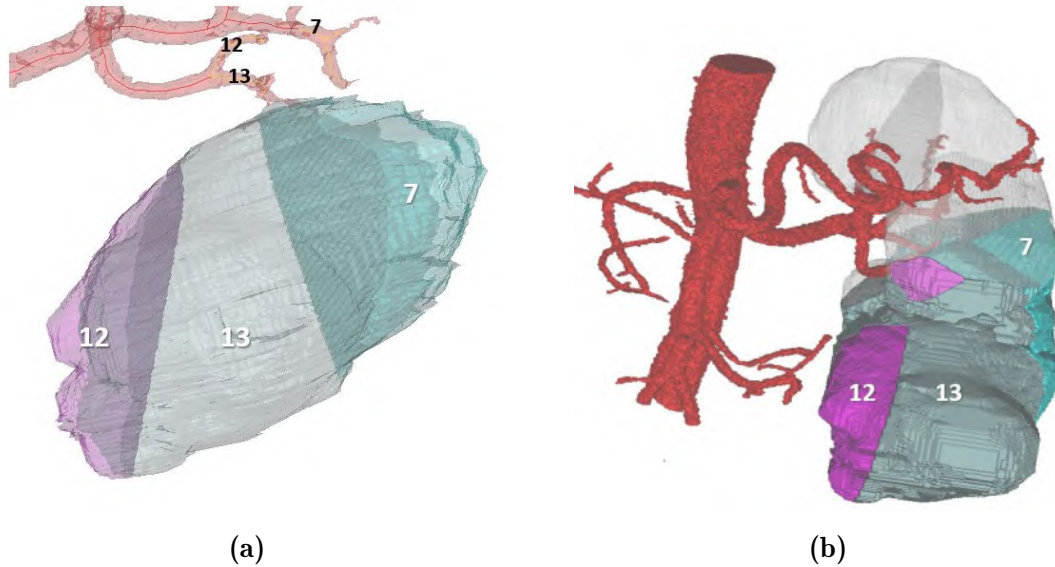


Figure 4.7: (a) The detail of the tumour of patient 2 shows 3 perfusion regions in the tumour, supplied by the branches 7, 12 and 13 according to the results of the model. (b) The perfusion zones supply zones of the tumour and also part of the healthy parenchyma.

Another case to take a closer look at is the 4th patient. The 3D reconstruction of the kidney with tumour and arterial tree as depicted in figure 4.2(d) suggests that there is a branch 9 that obviously seems to supply the tumour. Though, this branch is later on removed from the model because during clinical feedback there was suggested that this branch is actually not an artery, but part of the adrenal gland. In figure 4.8 the difference in results is depicted between adding branch 9 or not. Figure 4.9 depicts a detail of the tumour and shows that adding branch 9 results in an additional perfusion zone in the tumour, and a reduction of the region perfused by branch 11.

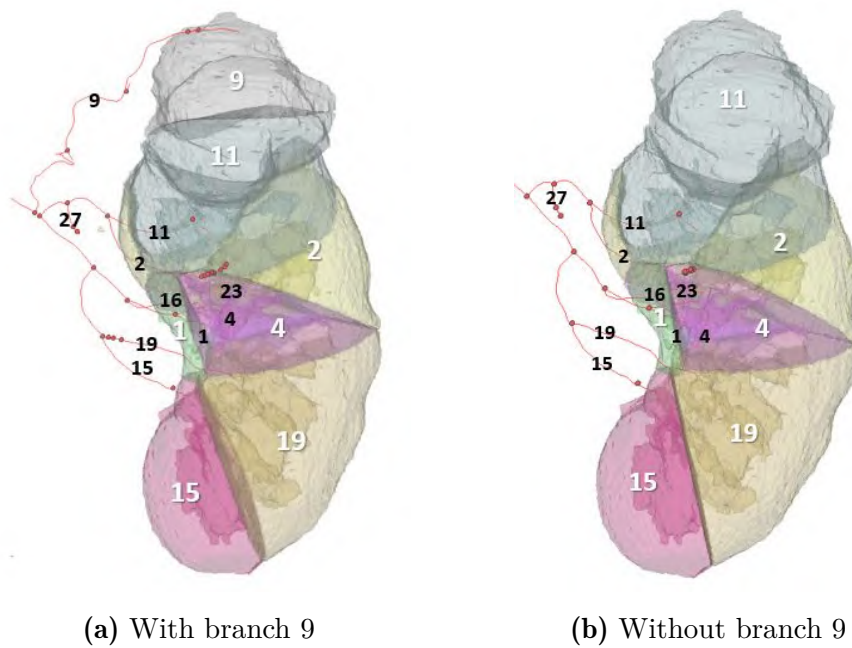


Figure 4.8: 3D perfusion maps of the kidney of patient 4 with branch 9 added and without this branch.

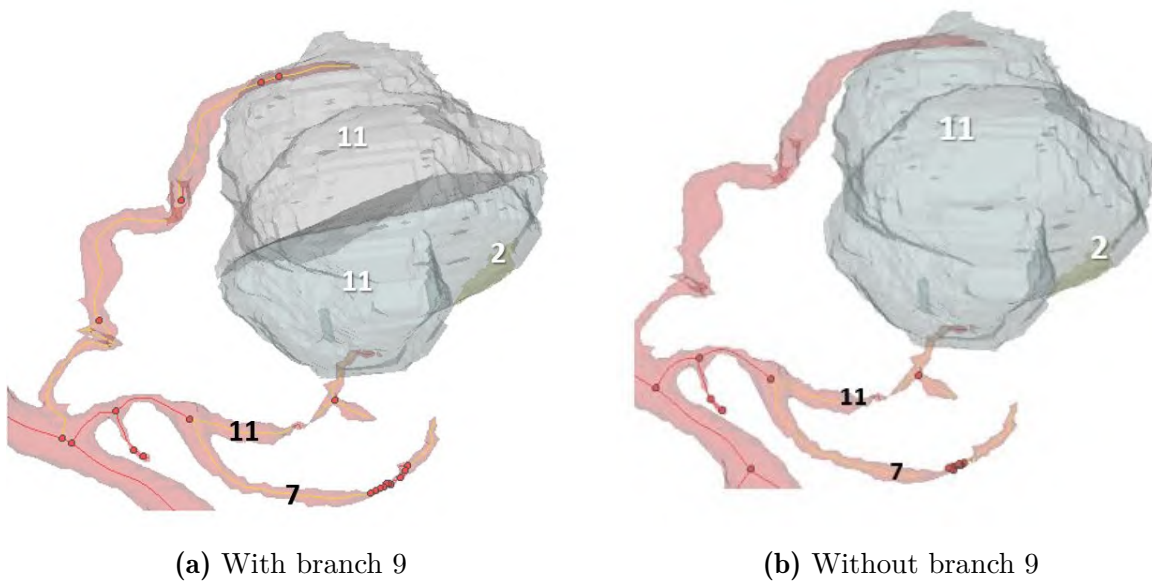


Figure 4.9: (a) The detail of the tumour of the patient 4 when segment 9 is added to the model shows that there are 3 branches perfusing the tumour namely 2,9 and 11. (a) The detail of the patient 4 when there is no segment 9 shows that there are only 2 branches supplying the tumour, namely 2 and 11.

The results until now are obtained by using all information of the arterial tree. Now, it is interesting to see what happens to the results when not all information is imported in the model. That can be achieved by pruning the original arterial model to a certain level. For patient 1, the arterial tree is pruned until only the first three generations remain. In figure 4.10 the perfusion maps supplied by branches of the 3rd generation are shown based on this pruned tree and based on the original tree. It is clinically relevant to take a look at the perfusion zones of this lower generation, as during surgery, usually arteries of the 3rd or 4th generation are clipped, but almost never higher generations.

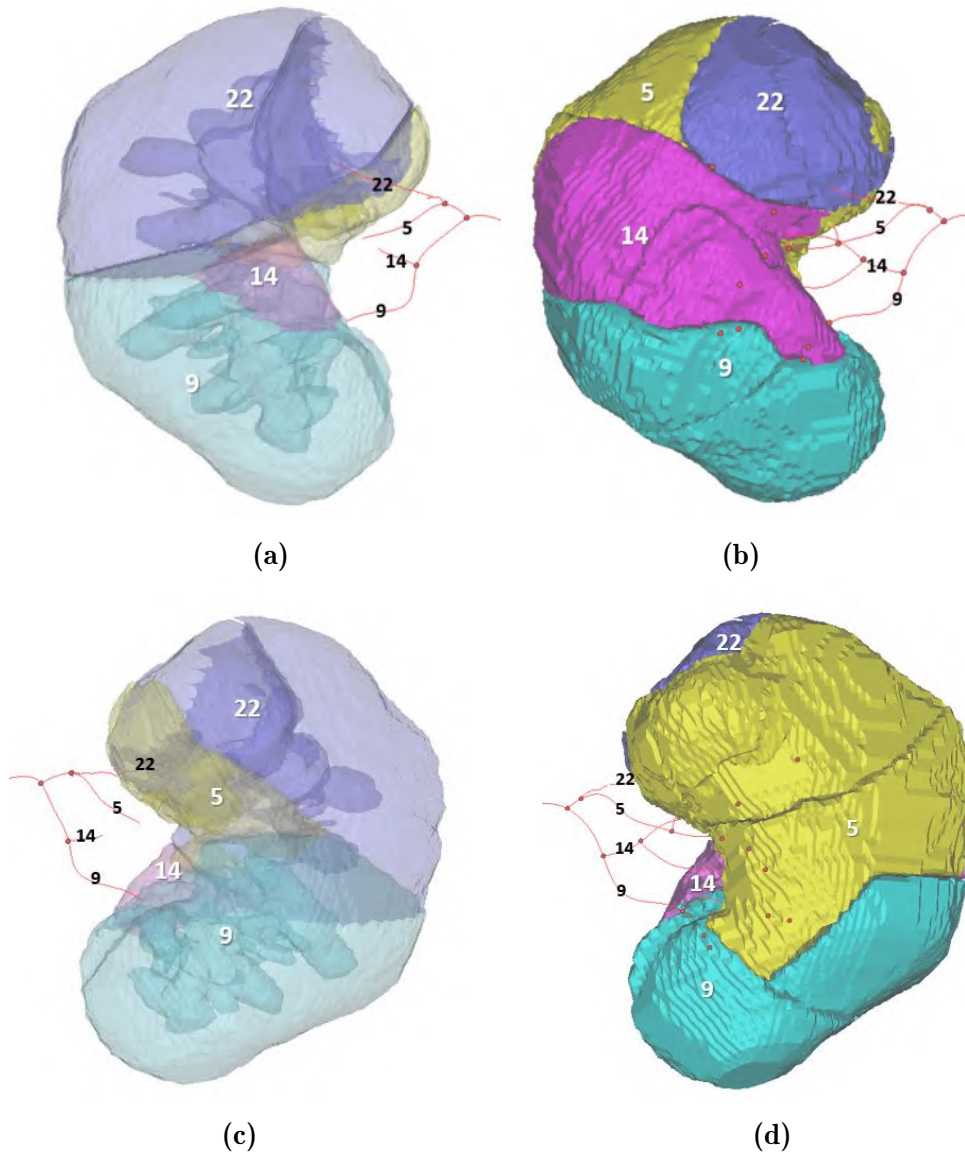


Figure 4.10: Perfusion zones of the branches of the 3rd generation. (a-c) The perfusion zones are determined based on the information of the pruned tree. (b-d) The results are obtained based on the complete tree

The perfusion zones based on the pruned tree are very different from those of the original tree, implying that the quality of the tree has an important influence on the quality of the results. Further, the zones are much larger, which means that clamping of these 3rd generation arteries will cause more healthy tissue ischemia and thus these branches are less suitable candidates. Figure 4.11 shows a close-up of the tumour divided into perfusion zones based on the complete and pruned tree. As discussed before, the complete tree predicts 5 branches supplying the tumour, namely 7, 16, 17, 22 and 28. The pruned tree, however, predicts two branches: segment 5, that supplies segments 7, 17 and 28, and segment 22. Hence, the perfusion model based on the pruned tree neglects the perfusion of the tumour via branch 16 and consequently, complete tumour ischemia cannot be realised when clamping based on these results. This shows that the complexity of the arterial tree reconstruction should be as high as possible to allow accurate predictions and correctly suggests locations for clamping to allow resection in a bloodless field.

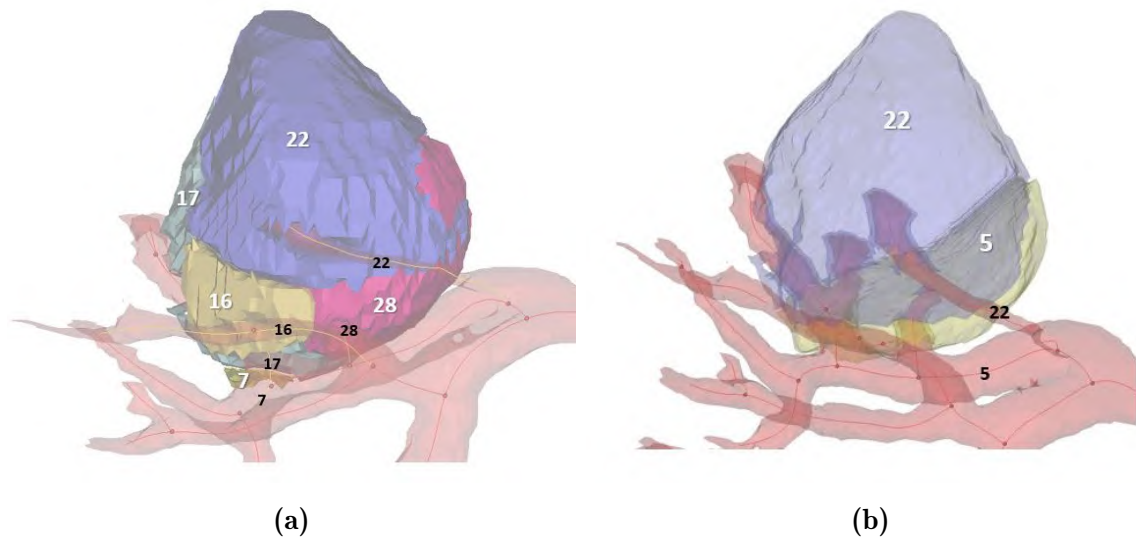


Figure 4.11: The detail of the tumour with (a) 5 perfusion zones when the complete arterial tree is used and (b) 2 perfusion zones when the tree pruned until only the 3 first generation remain.

4.3 Results of region growing method

In figure 4.12 the results of the region growing approach are shown next to those of the direct distance approach for patient 1. Though both methods have the same underlying principle, namely constructing a perfusion map giving for each voxel its closest branch, the volumes of the regions are not completely the same. For instance, when applying region growing, the region of branch 22 has expanded causing a reduction of the region of branch 28. The reason for these differences can be found in the way the region growing algorithm is implemented. The algorithm grows regions starting from control points and hence segments existing of more control points may be favored over those existing of only few control points.

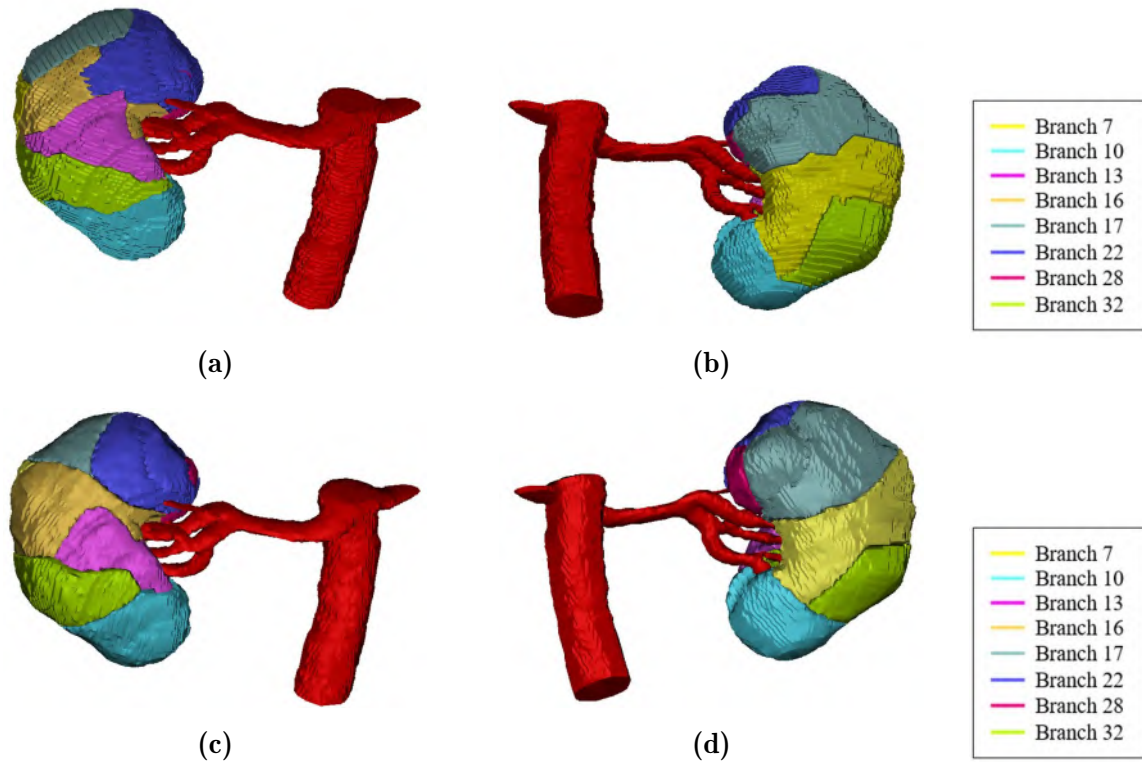


Figure 4.12: Anterior and posterior view on the perfusion maps of patient 1 obtained with region growing (a-b) and with the direct distance method (c-d). Each color represents a perfusion zone supplied by the corresponding arterial branch.

A closer look is taken to the tumour in figure 4.13. This is to see what branches supply the tumour according to the region growing method and how well these results match the results from the direct distances approach. Both approaches suggest the same branches that supply the tumour, though their regions are slightly different.

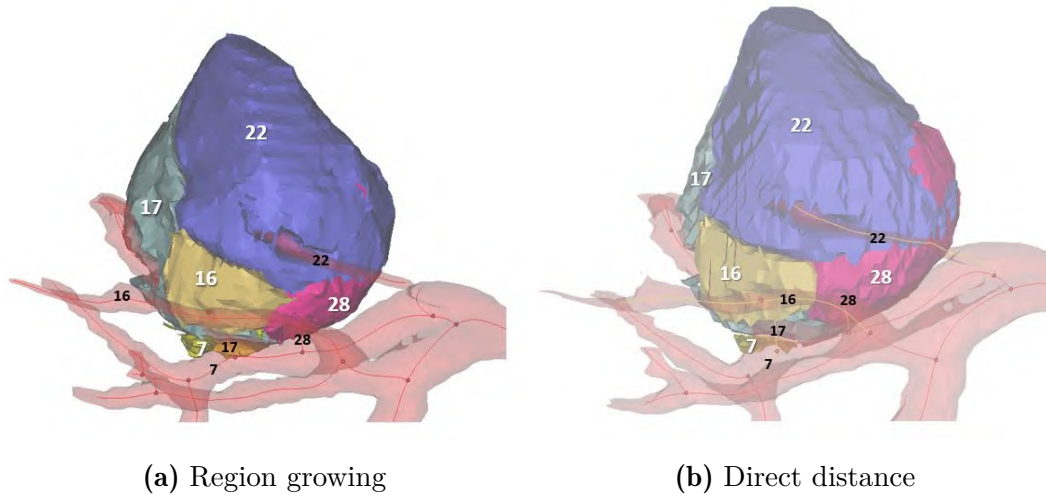


Figure 4.13: The detail of the tumour of patient 1 with perfusion zones determined according to (a) the region growing approach and (b) the direct distance approach.

The region growing method is also applied to the kidney of patient 2. Figure 4.15 compares again the resulting 3D perfusion maps for both methods. Here, again some differences in volumes are observed between the models, though these differences seem smaller than those for patient 1. When taking a closer look at the tumour in figure 4.14, both methods predict branch 7, 12 and 13 as the arterial segments supplying the tumour.

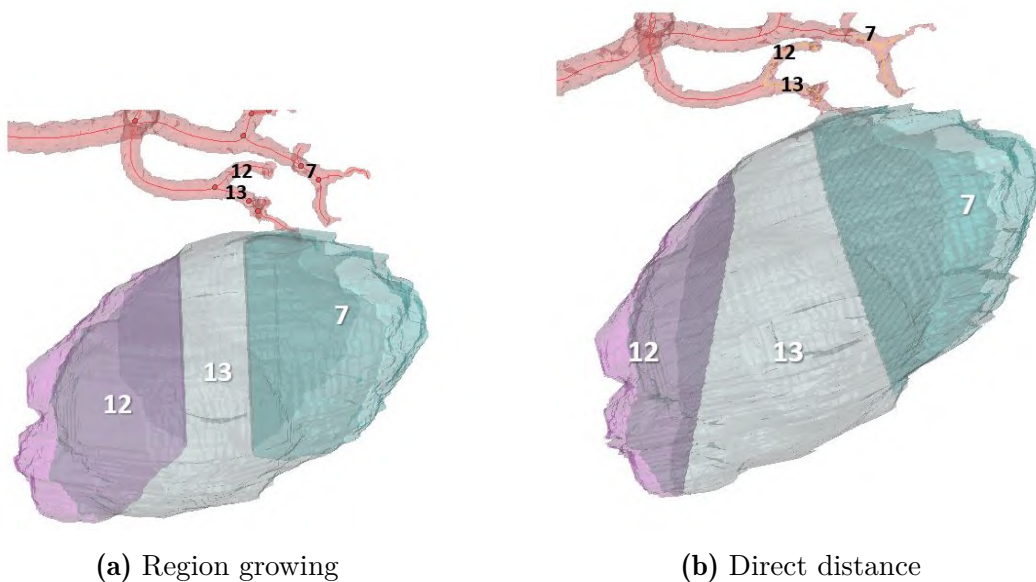


Figure 4.14: The detail of the tumour of patient 2 with perfusion zones determined according to (a) the region growing approach and (b) the direct distance approach.

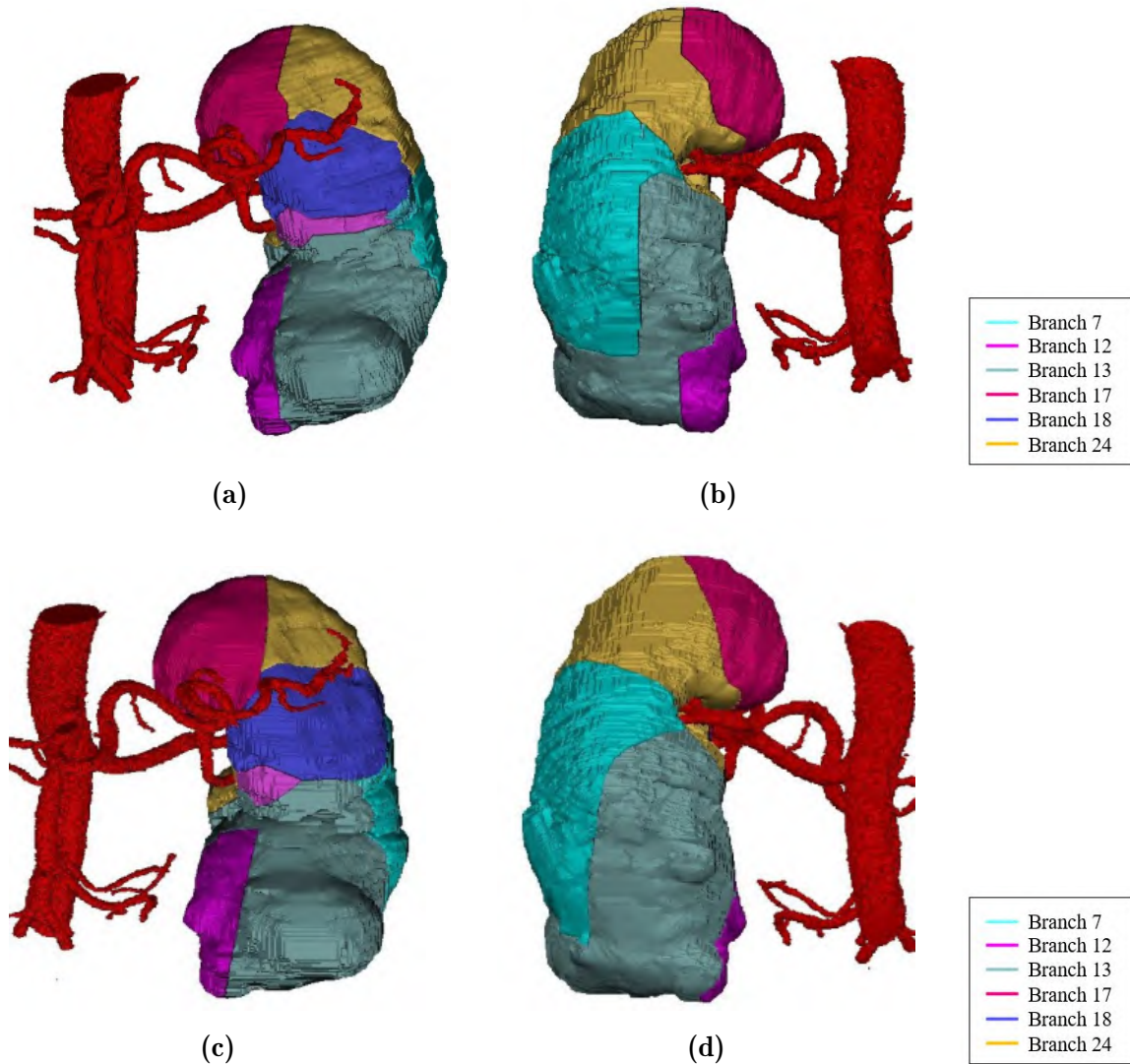


Figure 4.15: Anterior and posterior view on the perfusion maps of patient 2 obtained with region growing (a-b) and with the direct distance method (c-d). Each color represents a perfusion zone supplied by the corresponding arterial branch.

The perfusion volumes of the region growing and direct distance method are not completely the same. Though both methods have the same goal, the way they determine the nearest branch explains their differences in results. It is clear that the direct distance approach is the most accurate way to determine the nearest branch as it directly determines the minimum distance. The region growing method is more an approximating method. Though, this does not say anything about how well the direct distance approach approximates reality, because therefore validation is required. Despite the differences in perfusion volumes, the predictions about the tumour perfusing arteries were the same for both methods. Thus, the region growing method certainly seems like a suitable alternative for the direct distance method, especially because the computational time for running the model is shorter. However, this approach requires optimization for toward the future.

4.4 Validation of results

The results of the previous sections are first inspected visually to see whether these results could be valid. This visual inspection allowed to optimize the algorithm of the two methods to ensure that each voxel is assigned correctly to the branch that is closest to it. However, this inspection doesn't say anything about the quality of the results with respect to reality. One way to validate these models is validation with vascular corrosion casts as the study by Selle et al. [46] did. However, in the context of this thesis, a first validation of the results is done based on the outcomes of Visible Patient for 2 of our patients, as discussed in section 2.7.

For patient 1, figure 4.16 shows the resulting clipping model of Visible Patient next to the outcomes of the model based on the direct distance approach. The results of the model approximate the results of Visible Patient relatively well, though there are some differences in the volumes. As discussed in the previous sections, our model predicts that the tumour is supplied by five different branches, namely 7, 16, 17, 22 and 28. Though, Visible Patient predicts that only four of these branches perfuse the tumour and excludes branch 7 as depicted in figure 4.17. It is important to note that this segment 7 perfuses a large part of the healthy tissue, and hence the decision not to clamp can significantly reduce the region of local tissue ischemia during surgery. Visible Patient builds its clipping model starting from a more complex arterial tree as depicted in figure 4.18. This allows them to predict more precisely and may explain the differences in results.

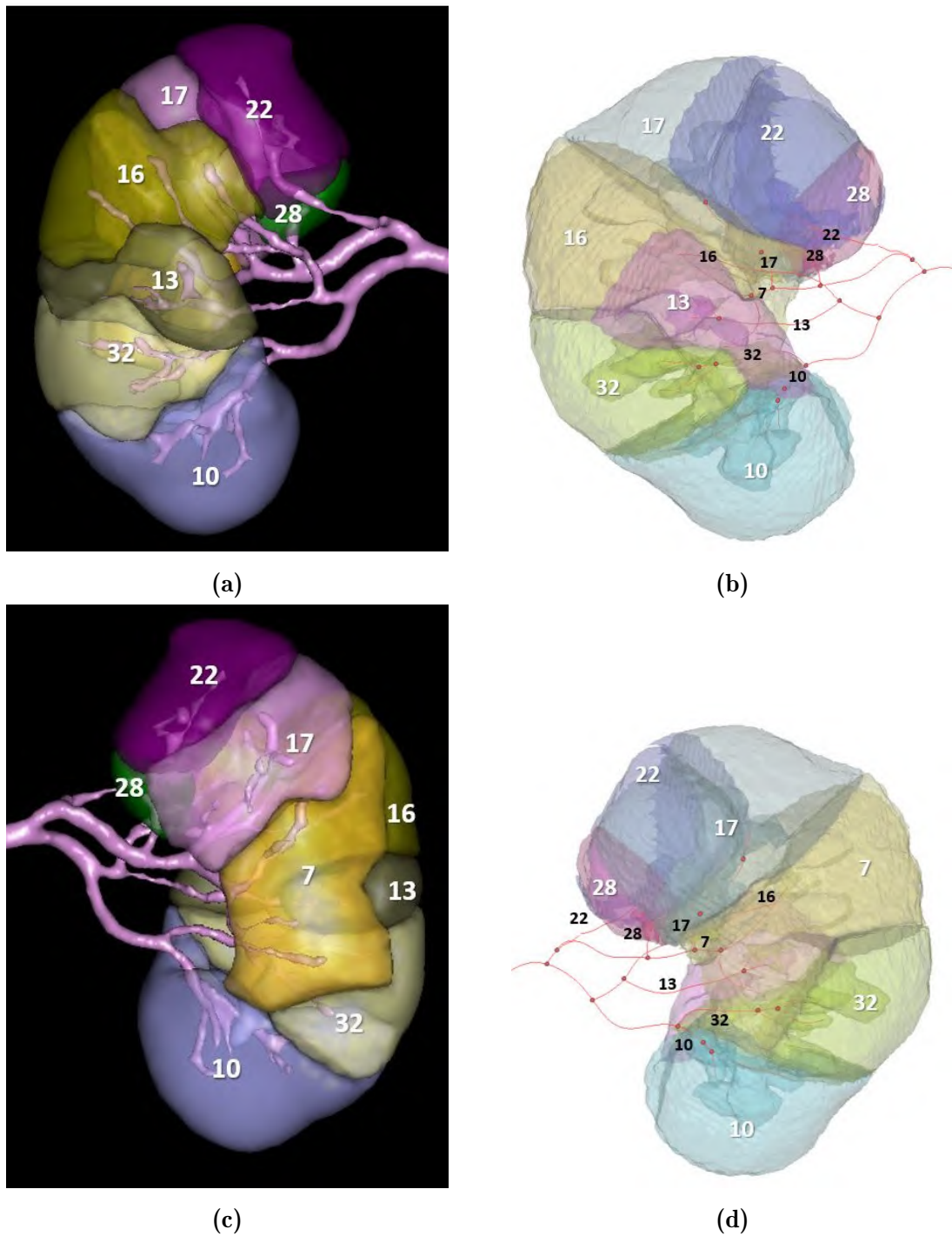


Figure 4.16: The results of Visible Patient (a-c) on the left side are compared to the results of our model (b, d) on the right side. The black numbers show the labels of the branches and the white and coloured numbers correspond to the perfusion zones.

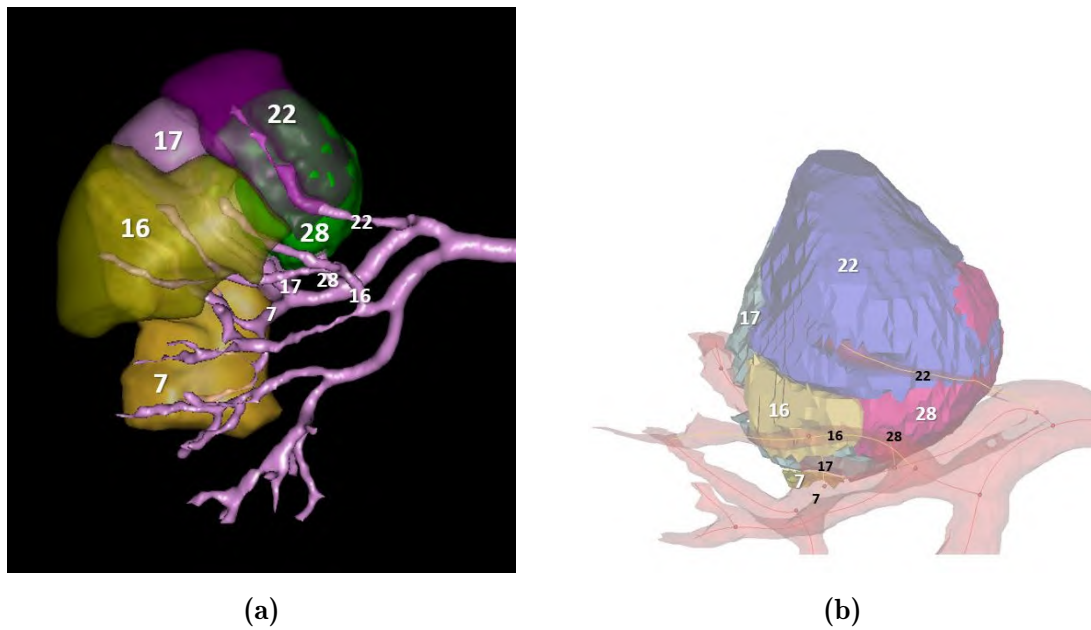


Figure 4.17: Detail of the perfusion zones supplying the tumour. (a) Visible Patient predicts that 4 branches supply the tumour, namely 16, 17, 22 and 28. (b) Our model suggests that there are 5 perfusion zones supplied by branches 7, 16, 17, 22 and 28.

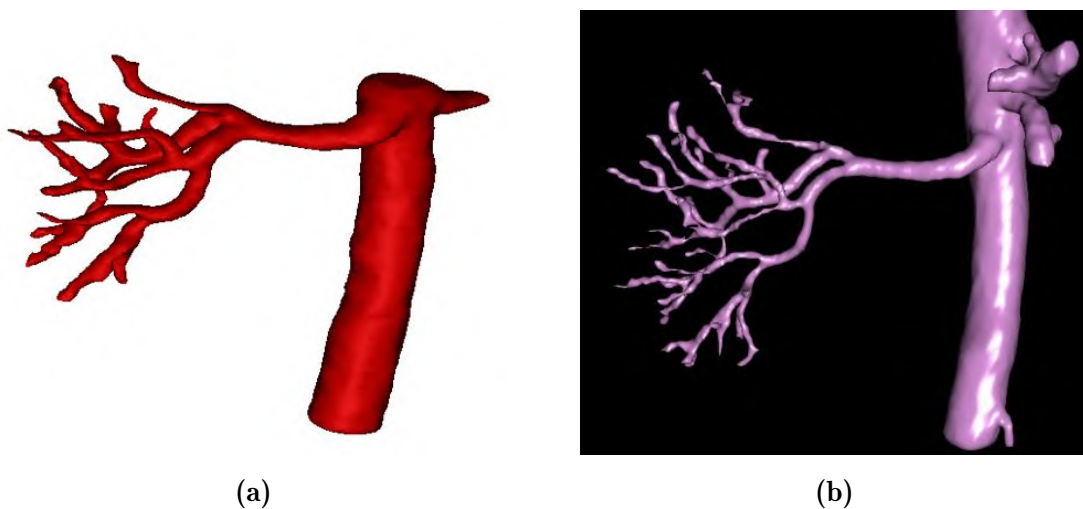


Figure 4.18: Arterial tree obtained by Visible Patient (b) has a higher complexity than the one used in our model (a)

The results of patient 2 can also be compared to outcomes of Visible Patient as depicted in figure 4.20. Again the locations of the regions are quite similar, but the volumes differ here more than in patient 1. In figure 4.19, the tumour is studied in detail, and there can be observed that Visible Patient predicts that only two branches supply the tumour while our model predicts three of them. When taking a closer look to the tumour vascularization in figure 4.21, the branches are much more complex in the clipping model of Visible Patient and therefore more information about the perfusion can be delivered.

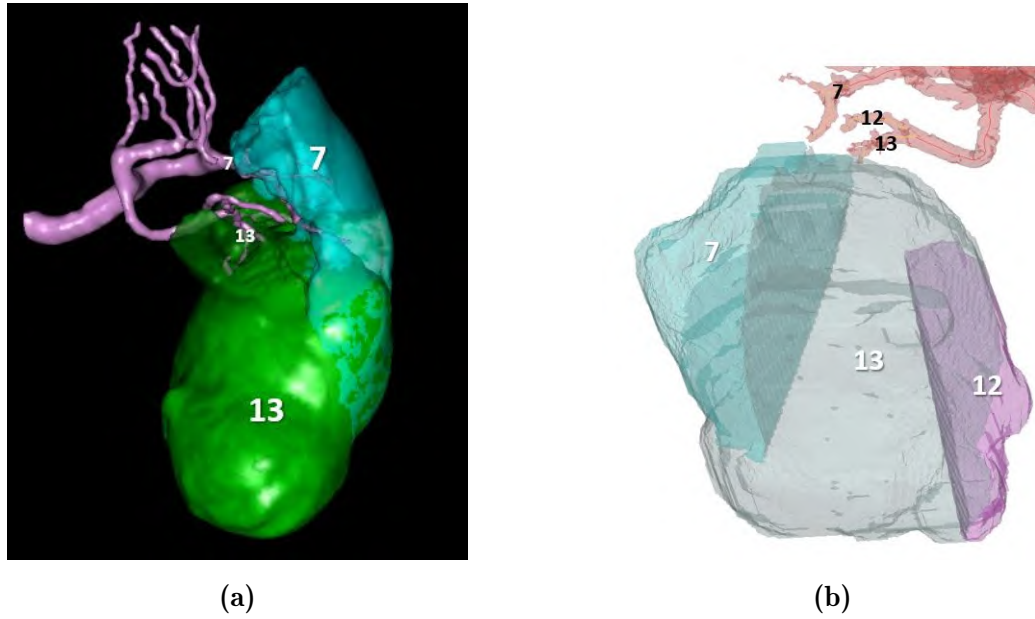


Figure 4.19: Detail of the perfusion zones supplying the tumour for patient 2. (a) Visible Patient predicts that 2 branches supply the tumour, namely 13 and 7. (b) Our model suggests that the 2 perfusion zones are supplied by branches 7, 12 and 13.

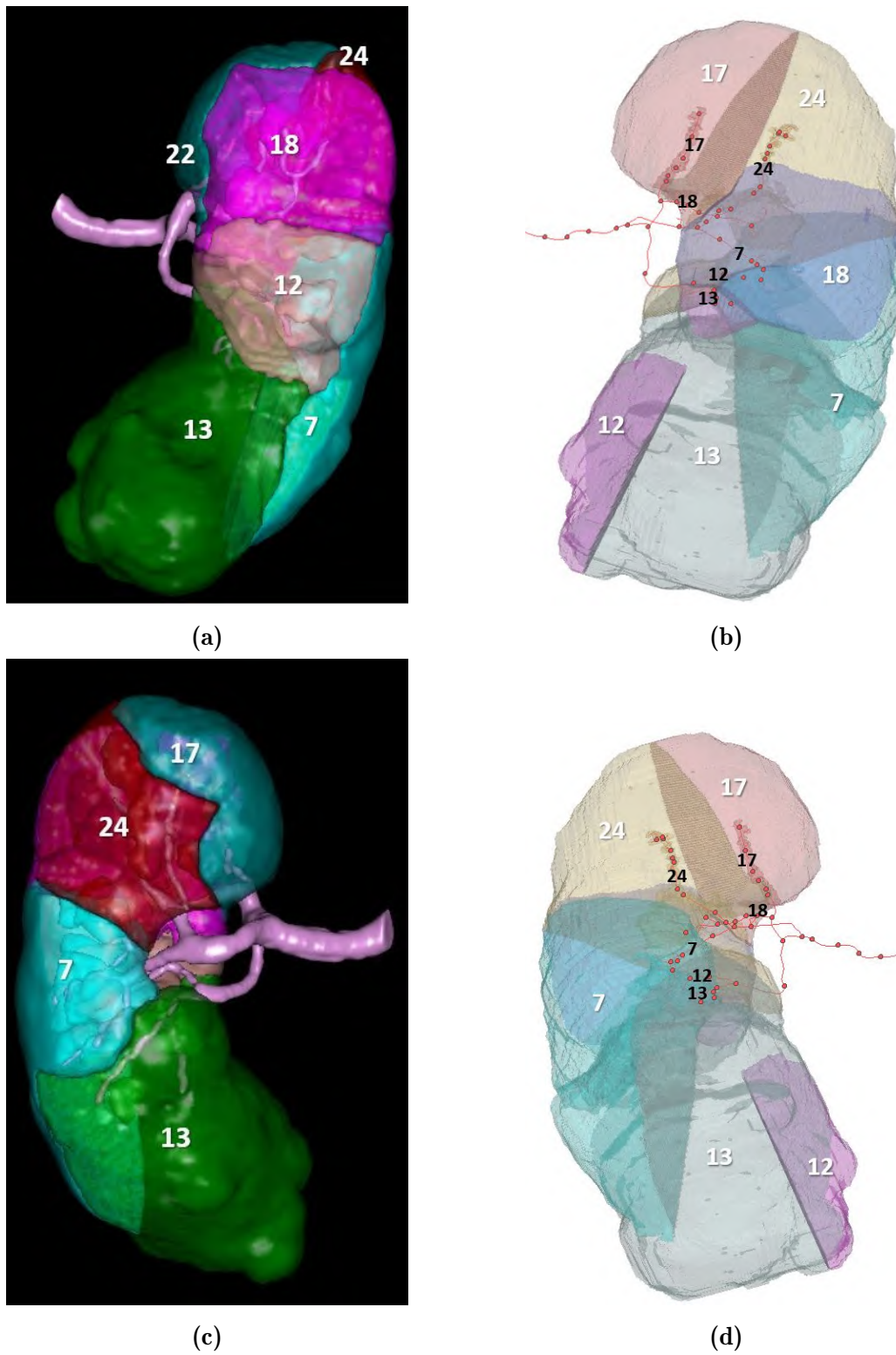


Figure 4.20: The results for patient 2 of Visible Patient (a-c) on the left side are compared to the results of our model (b, d) on the right side. The black numbers show the labels of the branches and the white and coloured numbers correspond to the perfusion zones.

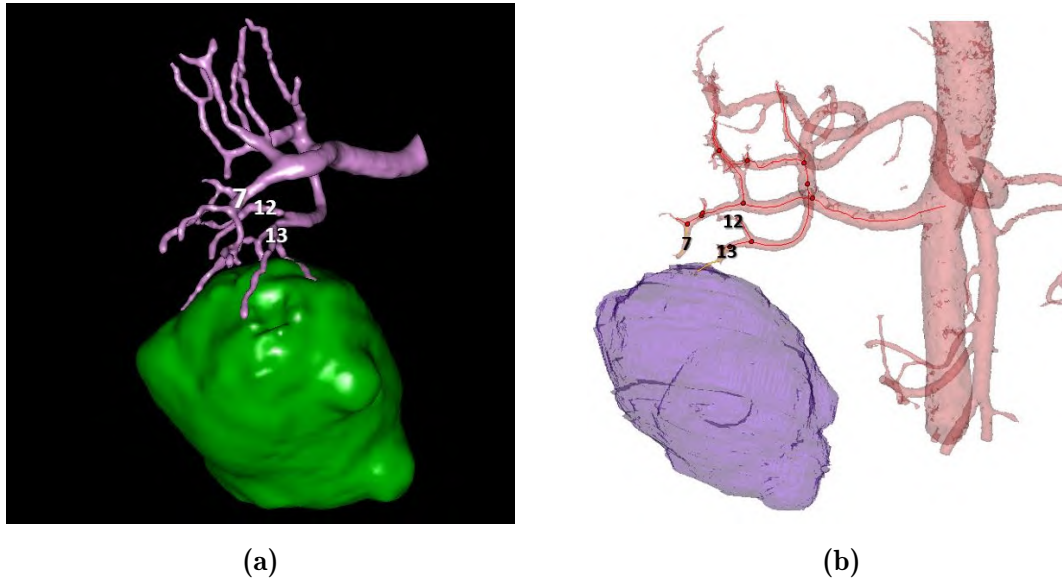


Figure 4.21: Arterial tree of patient 2 with tumour and tumour supplying arteries assigned. The arterial segments by (a) Visible Patient have a higher complexity than (b) those used in our model.

In conclusion, the results of Visible Patient and our model show similar results, implying that the algorithm based on the closest distance gives realistic results. However, thanks to their more detailed model of the arterial network, Visible Patient can predict the perfusion zones more precisely. For both patient cases, our model suggests that more branches should be clamped than what is actually needed to cause ischemia according to the outcomes of Visible Patient.

Chapter 5

Implementation

The planning tool is able to predict the arterial segments supplying the tumour based on a closest distance approximation. Currently, the outcomes are retrieved thanks to a combination of the perfusion model in Python and the image processing functionalities in Mimics. The workflow requires some manual work in Mimics for image processing and visualization and also for the perfusion model to adjust the patient-specific settings. Therefore, the user requires some anatomical and technical knowledge on the model to correctly execute these actions. Ideally, the manual part is automated and all steps are integrated into one interface that is easy to use and requires minimal manual work so that it can be used by the surgeon in clinical practice. As discussed in section 2.8, MeVisLab makes a good candidate, since it has several functionalities to import data, write code and visualizes images in 2D and 3D. Further, a tool developed in MeVisLab can also be integrated into *syngo.via* Frontier, the platform for medical applications of image processing developed by Siemens Healthineers and that may facilitate implementation in clinical practice.

This chapter explores the possibilities of MeVisLab to evaluate if the implementation of the complete planning tool is feasible in this environment. Therefore, a closer look is taken at the three main functionalities required for the implementation of this tool, namely import of imaging data, execution of the perfusion algorithm and 3D visualization.

5.1 Import imaging data

Let's assume that there is again started from the 3D reconstructions of the kidneys based on segmentations of CT data in Mimics. The image volumes can be exported from Mimics as 2D images of different formats. One frequently used format for medical images is Digital Imaging and Communications in Medicine (DICOM), which refers here to a specific digital format for medical images [3]. This file format is also supported in MeVisLab and thus, a network can be constructed to load several 2D slices in DICOM format and visualise the resulting image volume. MeVisLab has a specialised module, **DicomImport** that allows

to construct a 3D image volume in TIFF and DICOM format. By adding a module **ImageLoad**, one is able to load an image volume in TIFF or DICOM format in the network. That last module, in turn, can be connected to **View2D** or **View3D** for 2D and 3D visualization respectively. This simple flow is shown in figure 5.1.



Figure 5.1: The network required to load multiple DICOM slices and visualize the resulting image volume in 2D

The aim is reconstruction of the 3D structures of the kidney, tumour and arteries. Therefore, an additional step is required, since the segmentations are always exported together with the original CT image as background in DICOM format. This background can be removed by subtracting the original image from the segmented image, which is realised using the **Arithmetic** module. Figure 5.2 shows the schematic and MeVisLab network to the image volume of the kidney and visualise it.

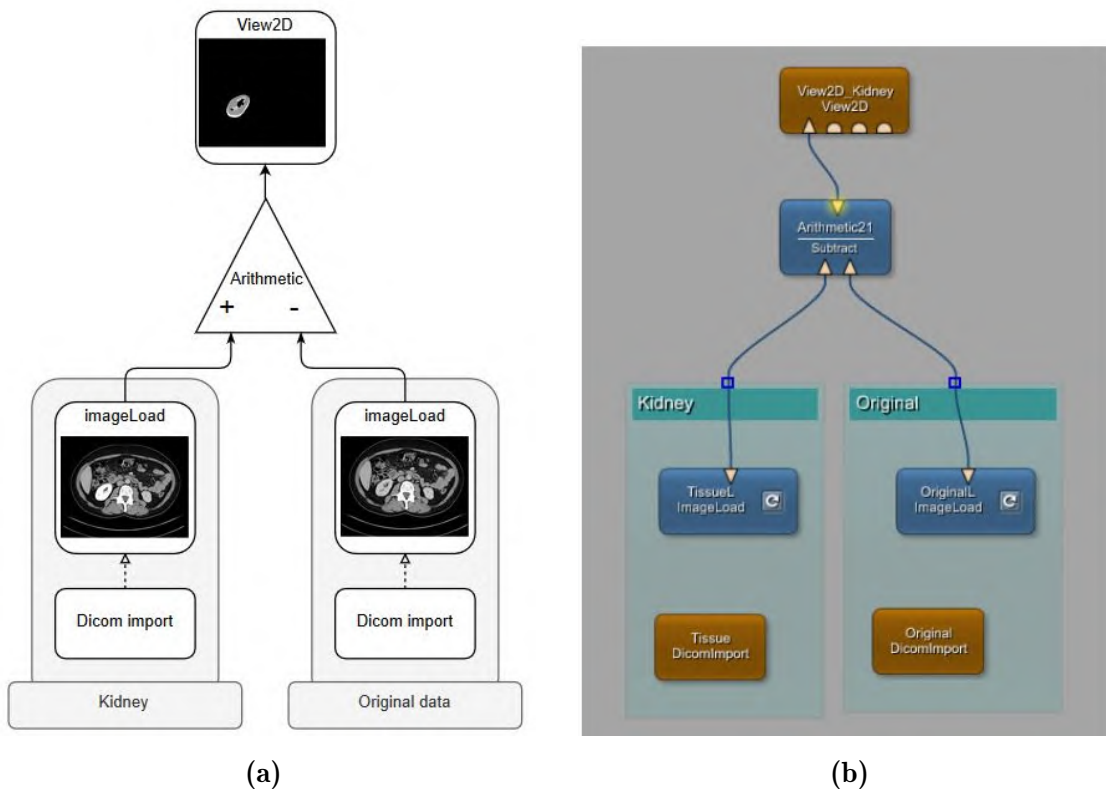


Figure 5.2: The network required to load and visualise the kidney volume starting from 2D DICOM slices exported from Mimics.

Alternatively, images in BMP format can be loaded in MeVisLab. The advantage of BMP compared to DICOM is that it is possible to export images containing only the segmented structures. Moreover, 3D visualisation of the resulting 2D image files is possible, since these outcomes are also in BMP format. There is no specific module present to load multiple BMP, and thus, an alternative approach is used as depicted in figure 5.3. Here, the image volume is loaded by connecting two modules, namely **imageLoadMulti** and **imageComposer**. The first module is able to run through a list of image files located in a given directory and the other is able to compose an image volume by stacking 2D image slices reaching this module. Thus, each time **imageLoadMulti** loads an image, it is sent to the **imageComposer** that adds it to the previous images until the complete image volume is reconstructed.

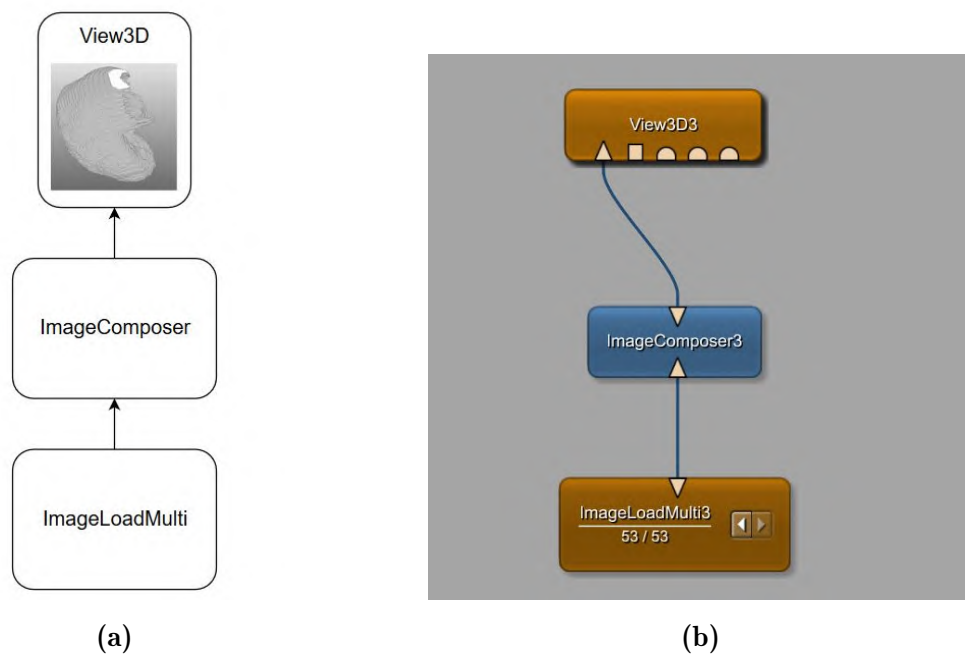


Figure 5.3: The network required to load and visualise the kidney volume starting from 2D BMP slices exported from Mimics.

The above methods make use of network approaches to load data. The data can also directly be loaded into the model by a specialised module constructed to run the model as discussed in the next section(5.2). For this application, it would be useful to be able to change variables outside the code by the use of text boxes. This is about variables that change with every patient. An overview of these variables is given in table 5.1.

Parameters	file type
Skeleton	file name for skeleton textfile
Kidney tissue	location of .bmp 2D image slices of the kidney tissue
Tumour tissue	location of .bmp 2D image slices of the tumour
Arteries	location of .bmp 2D image slices of the arteries
Slice gap	number in mm
Start	z coordinate of first slice
Coordinate Transformation	$X_{min}, Y_{min}, Z_{min}$ $\Delta X, \Delta Y, \Delta Z$ $\Delta X_{sk}, \Delta Y_{sk}, \Delta Z_{sk}$
Points in kidney	list of points in kidney
Grouping points in kidney	list of groups

Table 5.1: Overview of what should be manually inserted in the model.

5.2 Implementation of the algorithm

Here, a closer look is taken at the implementation of the perfusion algorithm in MeVisLab by construction of a macro module. With the project wizard, the module can be created via the window shown in figure 5.4. First, a user package needs to be created to be able to select this package when creating this module. Thereby, a Python file is added to the macro module to be able to implement the code. Further, it is possible to create fields to allow the user to insert specific file directories or variables. The create button allows to create a module with the related Python and script file.

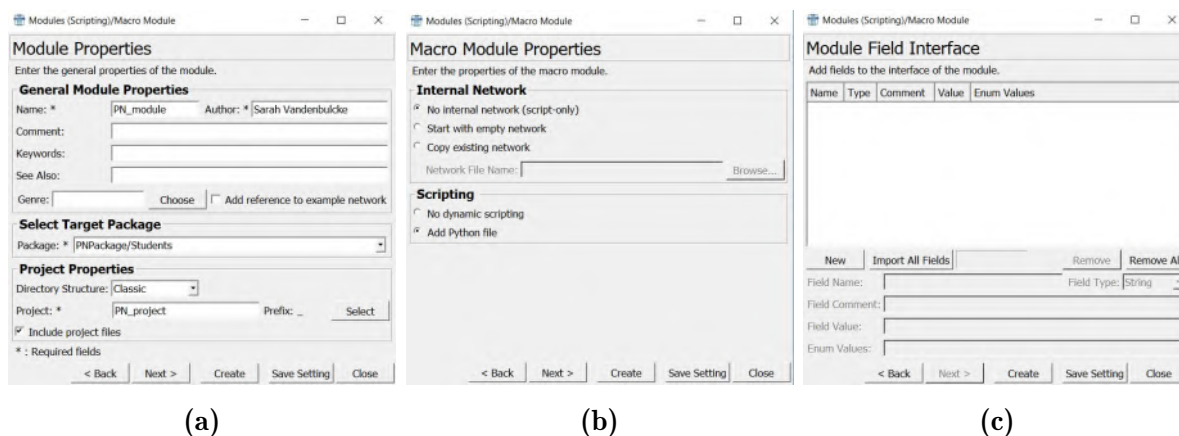


Figure 5.4: Window to create a macro module. (a) The name of the module, the project and the package is selected. (b) A Python file can be added to the module to allow scripting. (c) Fields can be created to import for instance specific variables or directories.

The functionalities of the module are implemented in the script. One possibility is the creation of a button that allows to run the program. This can be done by changing the code in the script and the Python file that can be found as depicted in figure 5.5. The script file can easily be used to create a button or a checkbox, for instance, to choose different options in the model. However, running the Python script itself seems not to work resulting in an error that Python files of more than 2kB cannot be added/modified without a MeVisLab SDK licence, which is also mentioned on the website of MeVisLab [2]. Based on these outcomes, there should be searched for other solutions within the free version of MeVisLab. Otherwise, the purchase of a licensed version may be required.

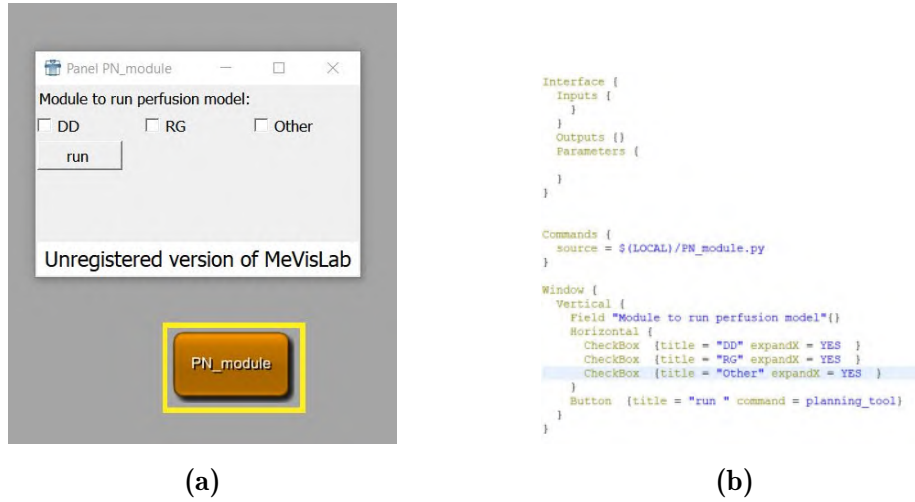


Figure 5.5: (a)Module to run the perfusion model with corresponding code (b) to define functionalities

5.2.1 Visualization

At last the 3D visualization in MeVisLab is discussed. Several formats can be loaded by specialised modules and thereafter visualized by the 2D or 3D visualization modules as discussed in section 5.1. There are two possible approaches to obtain a visualization of the tumour, kidney and arteries together. The first approach uses the same BMP image slices containing in the tumour, parenchyma and arterial tree as those imported in Mimics. The corresponding network is shown in figure 5.6.

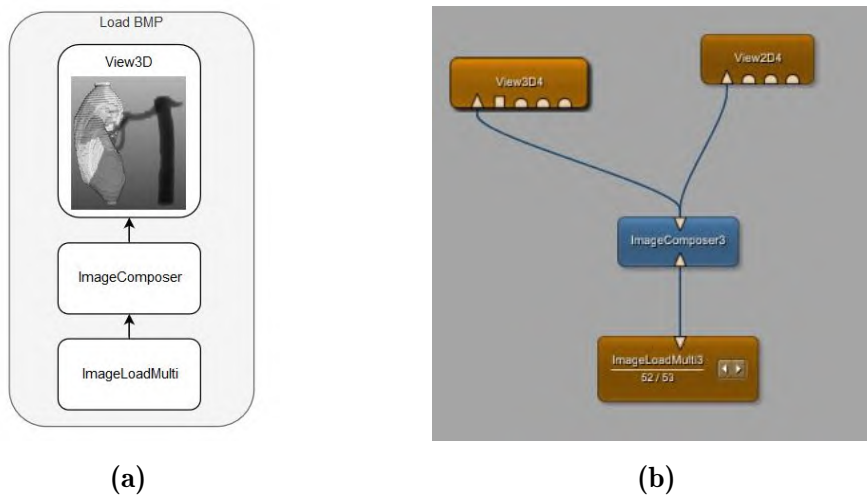


Figure 5.6: Network (a) schematic and (b) in MeVisLab to obtain 3D visualization of arterial tree and the perfusion zones of the kidney and tumour. There is started from the 2D BMP slices of the image volume that combines the tumour, kidney and arteries.

The other option uses the separate image slices of the tumour, kidney and arteries and combines these with an **Arithmetic** module. Figure 5.7 shows the corresponding network schematically and figure 5.8 depicts the constructed network in MeVisLab.

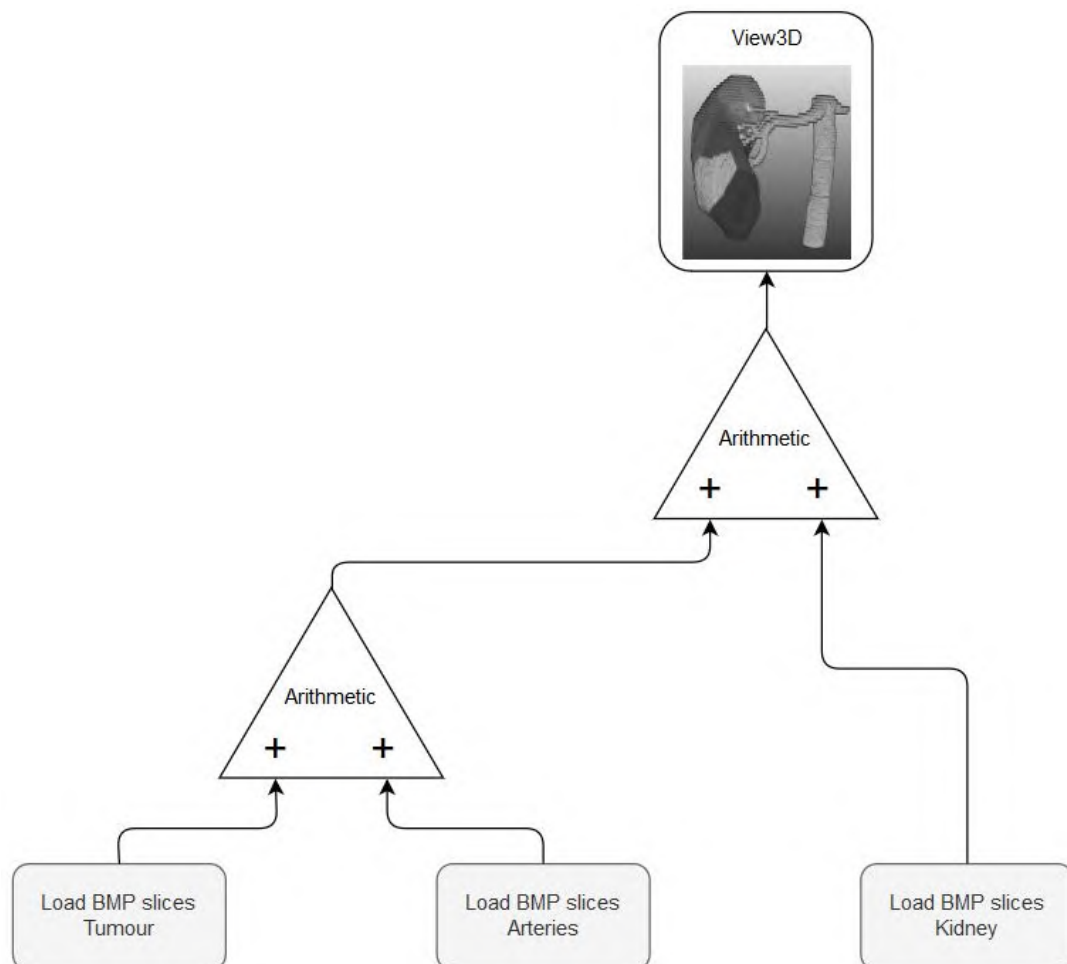


Figure 5.7: Schematic representation of the network to obtain 3D visualization of the arterial tree and the perfusion zones of the kidney and tumour when starting from the BMP files of the separate structures. Each load BMP slices module represents the combination of the **ImageComposer** and **ImageMultiLoad** module.

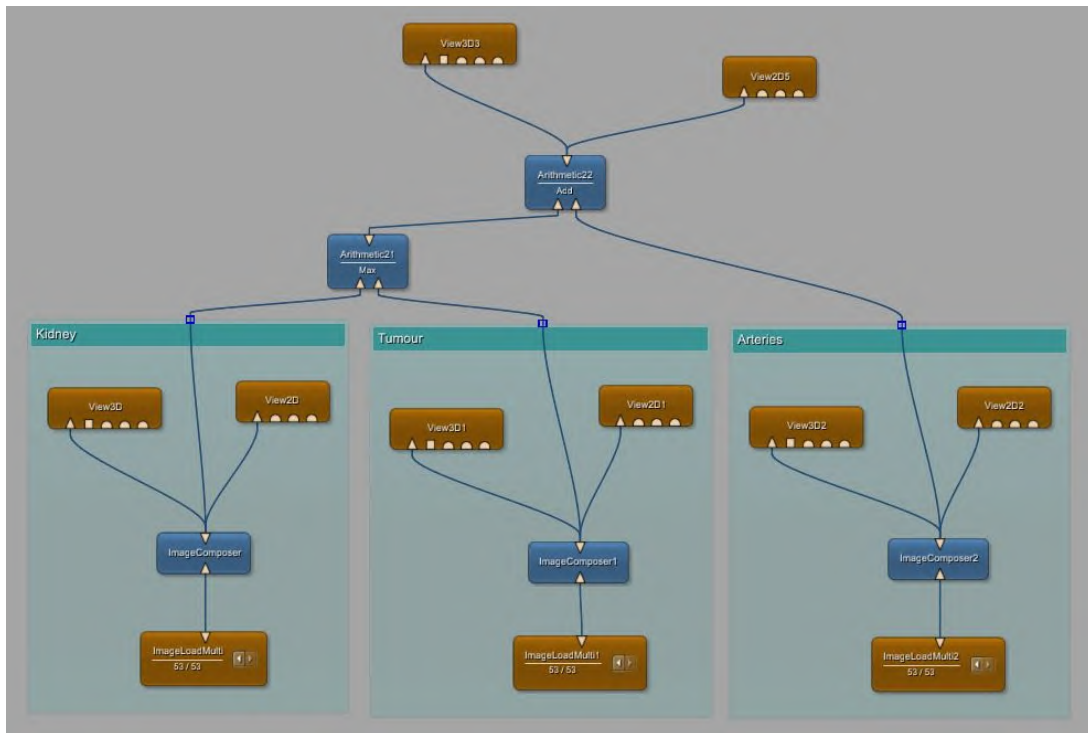


Figure 5.8: Network in MeVisLab to obtain 3D visualization of the arterial tree and the perfusion zones of the kidney and tumour. There is started from the 2D BMP slices of the tumour, kidney and arteries separately.

Figure 5.9(a) shows the 3D map of the perfusion zones for patient 3 when loading the arterial tree, tumour and kidney together and Figure 5.9(b) shows the same map when loading the three structures separately. Unfortunately, the images are unclear and it is difficult to distinguish the different perfusion zones. The quality of these outcomes is much lower than the Mimics quality, though there are ways to improve like conversion into a color image or increasing the contrast.

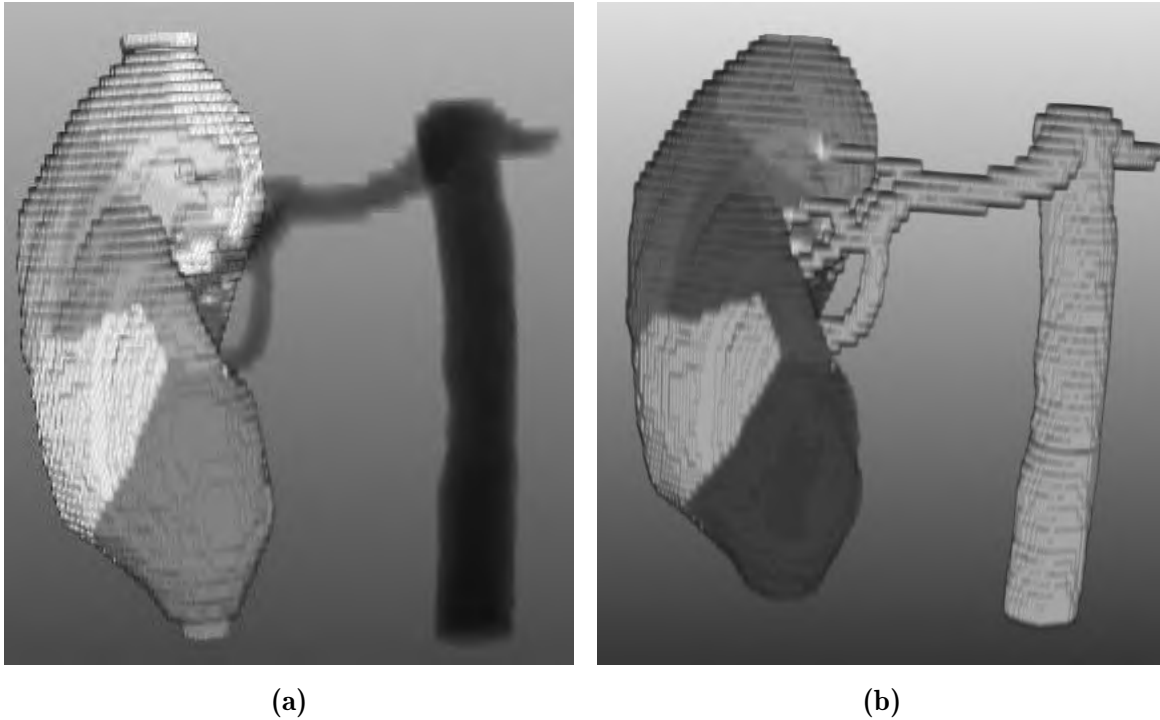


Figure 5.9: (a) Visualization of perfusion zones starting from combined images. (b) Visualization of the perfusion zones starting from separate images of the structures.

5.3 Conclusion

In conclusion, MeVisLab has a wide range of functionalities showing that this platform is very promising for implementation of the planning tool. Though during practical testing of the platform, some complications concerning the licence and visualization are encountered that should be solved to move towards proper functioning of the model and actual visualization.

Chapter 6

Conclusion and future prospectives

The aim of this thesis was the development of a planning tool for partial nephrectomy that helps the surgeon to decide on the ideal clipping locations by informing him about the renal perfusion. Therefore, a model is developed that creates a 3D map of the arterial perfusion zones by assigning each point of the parenchyma and tumour to the closest arterial branch. This map allows to distinguish the branches supplying the tumour from those that only supply healthy tissue and thus select these tumour supplying arteries for clipping.

The results of two patients are compared with the clipping models realised by Visible patient to validate the performance of the model. For both patients, the perfusion model correctly predicted all the branches perfusing the tumour according to Visible Patient, but also suggested an additional branch. That suggests that clamping based on the outcomes of the perfusion model allows complete tumour ischemia, but also causes the region of healthy tissue ischemia to become larger than strictly needed.

The comparison with the clipping model of Visible Patient shows that the model gives anatomically relevant results, though there is still room for optimization. Firstly, the optimization of the model should include the improvement of the quality of the outcomes. Here, the critical factor is the quality of the input data, and in particular the quality of the 3D reconstruction of the arterial tree. It is obvious that the reconstructed arterial tree should be as precise as possible to better approximate the real arterial tree. Unfortunately, the examined patients have a highly pruned tree, which implies a rather difficult reconstruction of the real perfusion zones. Hence, towards the future, it is important to search for ways to improve the segmentation. Moreover, because the segmentation by Visible Patient is more detailed, it will be interesting to investigate the performance of our algorithm against the commercial package of Visible Patient when applying it to identical segmentations.

Further, the comparison between the region growing and direct distance method showed that perfusion volumes between these approaches are slightly different. Though the aim of both methods is the same, it is clear that the direct distance approach is directly derived from the definition and thus is the most accurate way to determine the closest branch. However, its major drawback is the computational time. Therefore, ways to optimize the region growing approach should be explored, so that the results approximate better the direct distance outcomes. Moreover, the region growing approach has interesting possibilities for more advanced perfusion modelling as the growing speed can be adjusted. Up to present, the model assumes that perfusion of the parenchyma occurs isotropically, which means that blood diffuses with the same speed in all directions independent of the tissue it goes through. However, in reality, as discussed in section 2.1, the parenchyma is not homogeneous and exists of the different structures with different orientations. It seems obvious that the diffusion of blood will adjust its direction and speed based on the orientation and density of structures. Besides that, the cross-section of the arteries may also influence the size of the perfusion regions. Towards the future, it will be interesting to study diffusion speed and direction in the tumour or near the urinary tract system or when starting from a larger artery and implement these anatomical differences in the region growing algorithm.

On the other side, the planning tool is destined for use in clinical practice and therefore, requires realistic results and a user-friendly interface for the surgeon. The current model has promising results but contains a lot of manual work that requires specific technical knowledge. Therefore, reducing the manual work is definitely key. Up to present, the skeleton is automatically generated using Mimics. Apart from the adjustments that are done to improve the skeleton, the settings for the coordinate transformation need to be defined too, as the Mimics coordinates system is different from the dimensions of the slices. Possible solutions include the creation of a thinning algorithm as proposed by [46] and [38]. Aside from automation of the different steps, implementation of the complete tool in one interface to have a completely automated process is the final aim of the model and can be realised by the use of MeVisLab. This platform allows to integrate different steps of the workflow as modules in one interface. Moreover, a module for automatic segmentation can also be added to the model, so that the complete workflow, starting from contrast-enhanced CT data until the visualization runs fully automatically. Unfortunately, the implementation of the perfusion model is not yet realised due to limitations of the non-licensed version of MeVisLab on the integration of python files.

Beside all these optimization steps, the results of the model need to be validated. Therefore, information about the surgical outcomes and the indocyanine green measurements can serve as validation. Further, vascular corrosion casts and animal studies can validate the final model.

In conclusion, the model has promising outcomes and is able to predict the tumour supplying branches. Based on the comparison with the results of Visible Patient, the suggests correctly which branches to clamp to have complete tumour ischemia. Though currently, falls positives occur resulting in unnecessary healthy tissue ischemia. This model is applied on the kidney, but also offers possibilities to apply on other organs such as the liver, lungs and brain.

Bibliography

- [1] Materialise mimics. <https://www.materialise.com/en/medical/software/mimics> [accessed March 3, 2019].
- [2] Mevislab: Features. <https://www.mevislab.de/mevislab/features/> [accessed April 10, 2019].
- [3] Understanding and using DICOM, the data interchange standard for biomedical imaging. 4(3):199–212, 1997.
- [4] How do the kidneys work? <https://www.ncbi.nlm.nih.gov/books/NBK279385/> [accessed February 13, 2019], Mar 2018.
- [5] Kidney cancer. Retrieved from <https://www.mayoclinic.org/diseases-conditions/kidney-cancer/symptoms-causes/syc-20352664>, Apr 2018. [accessed April 10, 2019].
- [6] F. Becker, H. Van Poppel, O. W. Hakenberg, C. Stief, I. Gill, G. Guazzoni, F. Montorsi, P. Russo, and M. Stöckle. Assessing the Impact of Ischaemia Time During Partial Nephrectomy. *European Urology*, 56(4):625–635, 2009.
- [7] J. G. Betts, P. DeSaix, E. Johnson, J. E. Johnson, O. Korol, D. H. Kruse, B. Poe, J. A. Wise, and K. A. Young. Anatomy and physiology: Openstax. <https://opentextbc.ca/anatomyandphysiology/chapter/introduction-ch-25/> [accessed February 13, 2019], 2016.
- [8] L. M. Biga, S. Dawson, A. Harwell, R. Hopkins, J. Kaufmann, M. LeMaster, P. Matern, K. Morrison-Graham, J. Runyeon, L. Whittier, and et al. Anatomy & physiology. <http://library.open.oregonstate.edu/aandp/chapter/25-2-microscopic-anatomy-of-the-kidney-anatomy-of-the-nephron/> [accessed May 9, 2019], 2019.
- [9] M. Bjurlin, T. McClintock, and M. Stifelman. *Near-Infrared Fluorescence Imaging with Intraoperative Administration of Indocyanine Green for Robotic Partial Nephrectomy*, volume 16. Springer US, apr 2015.

- [10] S. Borojeni, A. Borojeni, P. Panayotopoulos, A. Bouvier, C. Aubé, A.-R. Azzouzi, and P. Bigot. Study of Renal and Kidney Tumor Vascularization Using Data from Preoperative Three-dimensional Arteriography Prior to Partial Nephrectomy. *European Urology Focus*, 2018.
- [11] P. Cairns. Renal cell carcinoma. *Cancer biomarkers : section A of Disease markers*, 9(1-6):461–473, 2011.
- [12] U. Capitanio, K. Bensalah, A. Bex, S. A. Boorjian, F. Bray, J. Coleman, J. L. Gore, M. Sun, C. Wood, and P. Russo. Epidemiology of Renal Cell Carcinoma. *European Urology*, 75(1):74–84, jan 2019.
- [13] R. G. Carroll and A. A. Abdel-Rahman. Renal Blood Flow. pages 1–2. Elsevier, New York, 2007.
- [14] D. M. Coll, B. R. Herts, W. J. Davros, R. G. Uzzo, and A. C. Novick. Preoperative use of 3d volume rendering to demonstrate renal tumors and renal anatomy. *RadioGraphics*, 20(2):431–438, 2000.
- [15] C. F. de Mello Júnior, S. A. Araujo Neto, A. M. de Carvalho Junior, R. B. Rebouças, G. R. P. Negromonte, and C. D. de Oliveira. Multidetector computed tomography angiography of the renal arteries: normal anatomy and its variations. *Radiologia brasileira*, 49(3):190–195, 2016.
- [16] A. M. Duffy, D. J. Bouchier-Hayes, and J. H. Harmey. Vascular endothelial growth factor (vegf) and its receptors. <https://www.ncbi.nlm.nih.gov/books/NBK6482/> [accessed March 24, 2019], 2019.
- [17] N. R. Dunnick. Renal cell carcinoma: staging and surveillance. *Abdominal Radiology*, 41(6):1079–1085, 2016.
- [18] K. Garfield and C. A. LaGrange. Cancer, renal cell. <https://www.ncbi.nlm.nih.gov/books/NBK470336/> [accessed February 29, 2019], Nov 2018.
- [19] N. K. Gautam, P. Verma, and M. G. Tapadia. Drosophila malpighian tubules: A model for understanding kidney development, function, and disease. In *Kidney Development and Disease*, pages 3–25. Springer, 2017.
- [20] J. T. Hartmann and C. Bokemeyer. Chemotherapy for renal cell carcinoma. *Anti-cancer research*, 19(2C):1541–1543, 1999.
- [21] S. Healthineers. syngo.via frontier. <https://www.siemens-healthineers.com/medical-imaging-it/advanced-visualization-solutions/syngo-via-frontier/features#04134224> [accessed April 10, 2019].

- [22] D. Herzlinger and R. Hurtado. Patterning the renal vascular bed. *Seminars in Cell & Developmental Biology*, 36:50–56, 2014.
- [23] ISO. Iso 13485 medical devices. <https://www.iso.org/iso-13485-medical-devices.html> [accessed May 11, 2019], Mar 2016.
- [24] R. Kabaria, Z. Klaassen, and M. K. Terris. Renal cell carcinoma: links and risks. *International journal of nephrology and renovascular disease*, 9:45–52, mar 2016.
- [25] F. Kunath, S. Schmidt, L.-M. Krabbe, A. Miernik, P. Dahm, A. Cleves, M. Walther, and N. Kroeger. Partial nephrectomy versus radical nephrectomy for clinical localised renal masses. *Cochrane Database of Systematic Reviews*, (5), 2017.
- [26] S. W. Leslie. Anatomy, abdomen and pelvis, renal artery. <https://www.ncbi.nlm.nih.gov/books/NBK459158/> [accessed February 15, 2019], Dec 2018.
- [27] A. S. Levey, S. P. Andreoli, T. DuBose, R. Provenzano, and A. J. Collins. Chronic kidney disease: Common, harmful, and treatable—world kidney day 2007. *JASN*, 18(2):374–378, 2007.
- [28] C. Y. Z. Liao. Comparison of radical nephrectomy and partial nephrectomy for t1 renal cell carcinoma: A meta-analysis. *Urol Int*, 101:175–183, 2018.
- [29] W. M. Linehan, R. Srinivasan, and L. S. Schmidt. The genetic basis of kidney cancer: a metabolic disease. *Nature Reviews Urology*, 7:277–285, 2010.
- [30] Y. Liu and Y. Jiang. Nephrectomy-procedures. <https://www.clinicalpainadvisor.com/anesthesiology/nephrectomy--procedures/article/581708/> [accessed February 13, 2019], 2018.
- [31] B. Ljungberg, L. Albiges, K. Bensalah, A. Bex, R. H. Giles, M. Hora, M. A. Kuczyk, T. Lam, L. Marconi, A. S. Merseburger, and et al. Eau guidelines on renal cell carcinoma. *European Association of Urology*, Mar 2018.
- [32] M. Medina-Rico, H. L. Ramos, M. Lobo, J. Romo, and J. G. Prada. Epidemiology of renal cancer in developing countries: Review of the literature. *Canadian Urological Association journal = Journal de l'Association des urologues du Canada*, 12(3):E154–E162, mar 2018.
- [33] A. Motiwala and O. Karim. Overview of partial nephrectomy techniques: influence of technology. <https://www.urologynews.uk.com/features/features/post/overview-of-partial-nephrectomy-techniques-influence-of-technology> [accessed March 30, 2019], Jul 2017.
- [34] S. Nabi, E. R. Kessler, B. Bernard, T. W. Flaig, and E. T. Lam. Renal cell carcinoma: a review of biology and pathophysiology. *F1000Research*, 7:307, mar 2018.

- [35] T. Nimeh. Robotic surgery partial nephrectomy. <https://www.fairbanksurology.com/robotic-partial-nephrectomy> [accessed February 20, 2019], 2 2019.
- [36] D. A. Nordsletten, S. Blackett, M. D. Bentley, E. L. Ritman, and N. P. Smith. Structural morphology of renal vasculature. *American Journal of Physiology-Heart and Circulatory Physiology*, 291(1):H296–H309, jul 2006.
- [37] C. A. OCallaghan. *The renal system at a glance*. Wiley Blackwell, 2 edition, 2017.
- [38] G. Peeters. *Modelling the degenerative adaptation of the liver vasculature and perfusion in Cirrhosis*. PhD thesis, Ghent University, 2017.
- [39] M. A. Perazella, R. Dreicer, and M. H. Rosner. Renal cell carcinoma for the nephrologist. *Kidney International*, 94(3):471–483, 2018.
- [40] F. Porpiglia, D. Amparore, E. Checcucci, R. Autorino, M. Manfredi, G. Iannizzi, and C. Fiori. Current Use of Three-dimensional Model Technology in Urology: A Road Map for Personalised Surgical Planning. *European Urology Focus*, 4(5):652–656, 2018.
- [41] F. Porpiglia, C. Fiori, E. Checcucci, D. Amparore, and R. Bertolo. Hyperaccuracy Three-dimensional Reconstruction Is Able to Maximize the Efficacy of Selective Clamping During Robot-assisted Partial Nephrectomy for Complex Renal Masses. *European Urology*, 74(5):651–660, 2018.
- [42] A. M. Potretzke, J. Weaver, and B. M. Benway. Review of robot-assisted partial nephrectomy in modern practice. *Journal of kidney cancer and VHL*, 2(2):30–44, apr 2015.
- [43] S. P. Raman, M. Mahesh, R. V. Blasko, and E. K. Fishman. CT Scan Parameters and Radiation Dose: Practical Advice for Radiologists. *Journal of the American College of Radiology*, 10(11):840–846, nov 2013.
- [44] M. Regier and F. Chun. Thermal Ablation of Renal Tumors: Indications, Techniques and Results. *Deutsches Arzteblatt international*, 112(24):412–418, jun 2015.
- [45] C. G. Rogers, A. Singh, A. M. Blatt, W. M. Linehan, and P. A. Pinto. Robotic Partial Nephrectomy for Complex Renal Tumors: Surgical Technique. *European Urology*, 53(3):514–523, 2008.
- [46] D. Selle, B. Preim, A. Schenk, and H. . Peitgen. Analysis of vasculature for liver surgical planning. *IEEE Transactions on Medical Imaging*, 21(11):1344–1357, 2002.
- [47] Trustpilot. Stages and prognosis for kidney cancer. <https://bookimed.com/article/stages-and-survival-rates-for-kidney-cancer/> [accessed April 3, 2019], 2019.

-
- [48] VisiblePatient. Visible patient: Now you see. now you know. <https://www.visiblepatient.com/en/> [accessed May 3, 2019], 2019.
- [49] B. Zeller-Plumhoff, T. Roose, G. F. Clough, and P. Schneider. Image-based modelling of skeletal muscle oxygenation. *Journal of the Royal Society, Interface*, 14(127):20160992, feb 2017.

Appendix

A Overview Python Files

Here the overview of the Python files is given. For the actual code, or more information, please contact supervisors or IBiTech-bioMMeda research group.

A.1 Patient-specific settings

These python files contain the patient specific settings and should be executed prior to running one of the models. It is important to note that the files are named according to their corresponding 3D reconstructions, which are different from those in this document.

- Patient 1: **Patient3.py**
- Patient 2: **Patient5.py**
- Patient 3: **Patient6.py**
- Patient 4: **Patient8.py**

The table below gives an overview of the settings in Python with their corresponding description.

Setting in Python	Description
Define_patient	Map for storing data
skeleton	Skeleton file location
Tissues	Parenchyma file location
Tumours	Tumour file location
Arteries_D	Arterial tree file location
start	z-coordinate start slice
increment	Slice thickness
Xminc	X_{mc}
Yminc	Y_{mc}
Zminc	Z_{mc}
Xrangev	ΔX_{mc}
Yrangev	ΔY_{mc}
Zrangev	ΔZ_{mc}
Xrangev	ΔX_v
Yrangev	ΔX_v
Zrangev	ΔX_v
Points_in_kidney	Numbers branches in kidney
List_of_groups	List to assign branches in kidney in groups according to their parent branch

Table 6.1: Overview of the settings in Python with their corresponding description.

A.2 Algorithm of Perfusion model

These python files contain the Python code for the two perfusion models based on the direct distance and region growing method respectively. They don't require manual adjustments for use unless the user wants to change visualization in Python or output different BMP slices.

- Direct distance method: **Direct_distance_algorithm.py**
- Region growing method: **Region_growing_algorithm.py**

The table below gives an overview of the settings in Python with their corresponding description.

